UNIVERSITY OF OKLAHOMA

GRADUATE COLLEGE

ERROR ESTIMATION AND STRUCTURAL SHAPE OPTIMIZATION

A Dissertation

SUBMITTED TO THE GRADUATE FACULTY

in partial fulfillment of the requirements for the

degree of

Doctor of Philosophy

By

Xiaoguang Song

Norman, Oklahoma

1998

UMI Number: 9914416

ERROR ESTIMATION AND STRUCTURAL SHAPE OPTIMIZATION

A Dissertation APPROVED FOR THE

SCHOOL OF AEROSPACE AND MECHANICAL ENGINEERING

BY

James D. Baldwin

M. Cengiz Altan

Robert P. Anex

Charles W. Bert

Kelvin K. Droegemeier

ACKNOWLEDGMENTS

I would like to express my deepest gratitude to colleagues, classmates, professors and friends who have offered their advice, guidance and encouragement during the course of my research in the School of Aerospace and Mechanical Engineering. I would especially like to thank:

Professor James D. Baldwin, my advisor and dissertation committee chairman, for sharing his experience, for providing invaluable guidance throughout the course of this work, and for generously leaving me the space to pursue broad interests in my personal education, to explore my own thinking and to take credit for my own work;

Professor M. Cengiz Altan for his continued interest in my research, for many stimulating discussions, for his support and encouragement, and for serving on my dissertation committee;

Professor Robert P. Anex for serving on my committee on extremely short notice;

Professor Charles W. Bert for inspiring my interest in the lateral buckling analysis of a plate structure, for many stimulating discussions, and for serving on my dissertation committee;

Professor Kelvin K. Droegemeier for his continued interest in my research, for his patience, support and encouragement during my working at CAPS, and for serving as a member of dissertation committee;

Dr. Ronald A. Cox, my former advisor, from who I am indebted for the vast amount of engineering knowledge imparted to me, for his introducing me into the area of computational fluid dynamics and numerical optimization technique, for his support and encouragement throughout the course of my entire graduate study, and for his steadfast friendship I continue to cherish;

Dr. Vassilios E. Theodoracatos for introducing me to the exciting dual kriging fitting technique from which a part of this dissertation is based, and for serving on my general examination committee;

Dr. Dudley E. Smith for his continued interest in my research, and for serving as a member of my general examination committee; and

Dr. Vince Wong for his support and encouragement during my working at CAPS.

I would also like to personally thank Dr. John R. Christiansen, M.D. and his wife, Kim, for their generous support and encouragement through the major part of my graduate study, and for letting me use their tickets to enjoy so many Sooner football and basketball games. Their friendship was a primary factor in my enjoyment of life at the University of Oklahoma.

My deepest thanks also go to my supervisor at York International Corporation, Mr. Ian Campbell, for his invaluable support and encouragement in wrapping up this long overdue assignment.

This research was supported under various grants from the National Science Foundation, Seagate Technology, Inc. and Baker Oil Tools Company during my full-time graduate study, and York International Corporation during the final stage of this work. Those sources of support are gratefully acknowledged.

DEDICATIONS

I have always thought I may be one of the most fortunate men in this world because of members of my family, especially the following persons who have made impacts throughout my life:

My sister, Xiaomei Song, and brother, Xiaolin Song, have shown their care and support to me in every period from my childhood to my graduate study.

My uncle, Foshen Son, too deserves my thanks. The financial and spiritual support from his family through my graduate study was invaluable.

My wife, Ying Nie, to whom I wish to express sincerest appreciation. Her love and understanding have been major sources with which I have worked so hard. Without her continuous encouragement and support, this research may have never been possible. She and our son, Brian, have been great sources of enjoyment and amusement.

My parents, Furong Song and Zongyi Yang, deserve more than just the gratitude I can possibly give them. They have been working so hard so I could have a better life. They have loved, supported and encouraged me for many years to achieve my goals.

TABLE OF CONTENTS

LIST OF TABLES

LIST OF FIGURES

Page

ABSTRACT

This work is concerned with three topics: error estimation, data smoothing process and the structural shape optimization design and analysis. In particular, the superconvergent stress recovery technique, the dual kriging B-spline curve and surface fittings, the development and the implementation of a novel node-based numerical shape optimization package are addressed.

Concept and new technique of accurate stress recovery are developed and applied in finding the lateral buckling parameters of plate structures. Some useful conclusions are made for the finite element Reissner-Mindlin plate solutions.

The powerful dual kriging B-spline fitting technique is reviewed and a set of new compact formulations are developed. This data smoothing method is then applied in accurately recovering curves and surfaces.

The new node-based shape optimization method is based on the consideration that the critical stress and displacement constraints are generally located along or near the structural boundary. The method puts the maximum weights on the selected boundary nodes, referred to as the design points, so that the time-consuming sensitivity analysis is related to the perturbation of only these nodes. The method also allows large shape changes to achieve the optimal shape. The design variables are specified as the moving magnitudes for the prescribed design points that are always located at the structural boundary.

Theories, implementations and applications are presented for various modules by which the package is constructed. Especially, techniques involving finite element error estimation, adaptive mesh generation, design sensitivity analysis, and data smoothing are emphasized.

1 INTRODUCTION

1.1 Background

The efficient use of materials is a primary concern in engineering design. The aerospace and automotive industries have applied structural optimization to their designs of various structures and mechanical elements [5, 13, 55, 36]. It is generally believed that engineering design is an iterative process in that the design is continuously modified and refined until it meets all criteria set by designing engineers. Traditional design practice is primarily based on trial and error procedures, and therefore, requires extensive experience and intuition to achieve an optimal design for a complex mechanical system. The subject of effectively combining the structural finite element analysis technique and nonlinear constrained optimization algorithms has been widely investigated in the last two decades and optimization modules have been incorporated into a number of commercial finite element packages.

Applications of structural optimization are usually grouped in the literature into the following three categories: sizing, shape, topology and material of a structure. Early efforts in numerical structural optimization emphasized optimal sizing design. In other words, the goal was to predict the optimal element stiffness properties such as cross-sectional areas and moments of inertia for truss or frame system elements, or transverse thicknesses in a plate structure. One of main characteristics of using such a sizing method is that a changing value of a design variable will not influence the already-specified finite element mesh system. As a result, the varying responses in a structure due to changes in a design variable generally were a linear function of either the variable or its reciprocal. A substantial amount of work in optimal sizing applications can be found in the literature [e.g., 36].

Numerical shape optimization design (or optimal shape design), on which part of this study focuses, attempts to use numerical optimization techniques to achieve an optimal shape for an existing structure, usually through the perturbation of the structural boundary. An example illustrating the difference between the sizing optimization design and shape optimization one is that of minimizing the stress concentration at a hole in a plate. Sizing design would change the thickness of the plate near the hole, while shape design would focus on the effects of changing the shape of the hole boundary. Generally, a shape optimization is a more effective method than a sizing optimization to achieve an optimal design, but is more involved than a sizing optimization mainly due to the fact that it is necessary to consider the structural boundary shape changes, to maintain an adequate finite element mesh, and to ensure the accuracy of the sensitivity analysis.

It should be pointed out that the vast majority of success stories about numerical shape optimization applications were told within the framework of planar structures (either plane stress or plane strain). A limited number of the reports could be found on the shape optimization involving plate elements in the finite element calculation.

Compared with sizing and shape optimization techniques, less research has been conducted on topological optimization for structures. In topological optimization, the optimal design is sought by changing the layout of truss or frame structural elements, or, removing or creating internal boundaries or holes in continuum structures. The work by Michell in 1904 is commonly believed to be the earliest one engaging in topology optimization investigation. Research in this direction was essentially stagnant until 1988 when Bendsoe and Kikuchi [10] introduced a homogenization method based on the relaxation concept introduced by Kohn and Strang [45]. This innovative concept suggested that an original optimization design should be relaxed to introduce microscale perforation in certain interesting design areas. A recently published monograph [11] may be consulted for more details regarding this topic.

Algorithms used in structural optimization generally fall into one of three broad categories: optimality criteria methods, random search methods, or mathematical programming methods. In optimality criteria methods, all of the necessary (and sometimes sufficient) conditions of optimality (Kuhn-Tucker conditions, for example) are used to generate a system of equations. The resulting equations are then solved, partly explicitly (if possible) and partly iteratively, to provide optimal designs. Further details about this method and its applications can be found in a number of excellent review papers by Venkayya and coworkers [77, 14].

Random search techniques, such as genetic and simulated annealing algorithms [33], are based on a randomized procedure that systematically generates a large number of sample designs, out of which the best one is selected as the optimal design. The use of these techniques in structural optimization has been quite recent and has primarily concentrated on the sizing and topological optimizations of truss and frame structures [e.g., 60].

In mathematical programming methods, the gradients of objective and constraint functions are calculated for a given design and, subsequently, used to generate optimal and feasible directions for specifying the next design iteration. The procedure is repeated until the optimal design is achieved.

As numerical optimization theory and applications were developed, intensive studies have also been conducted in universities and companies all over the world to improve the pre-processing, finite element robustness, solving and post-processing. As a result, finite element (FE) analysis methods have become more and more popular in practical designs. Among many notable improvements, accurate and economical prediction of the stress (strain) field from the computed displacement solutions (stress recovery technique) has been investigated by researchers. The successes in this path can be stated to be due to mainly the contributions from the progress in error estimation and adaptive mesh generation of a FE solution procedure.

1.2 Scope and Objectives

There exist a number of serious deficiencies in existing shape optimization algorithms in the literature. Notably, these methods are all restricted to small shape changes because large shape changes will generally result in extreme distortion of the elements on which a structural solution is based in using FE techniques, as demonstrated later. Another deficiency shared by existing shape optimization codes is the tediousness in preparing the pre-process database and the lack of a fully automatic nature due to the requirement of constant user interaction. The principal objective of this work is to present the development of a novel node-based structural shape optimization package, which has a number of characteristics:

1) a computationally efficient and robust approach leading to accurate stress recovery for a planar structural problem;
2) a compact formulation for design sensitivity analysis;
3) a robust adaptive mesh generation system; and
4) a simple user interface.

This code was developed by combining the FE solvers, the error estimation, the stress recovery, the sensitivity analysis formulae and the proposed node-based boundary design point method and has been applied to a number of design problems of beam and planar structures. By a planar structure, we mean in this study that only membrane stress and in-plane deflection components are involved in the FE analysis; in a plate analysis, the additional bending and transverse effects are included in the analysis. Special emphasis is placed on technical aspects of the efficient implementation.

This work is organized as follows. A literature survey and overview of structural shape optimization is presented in Chapter 2. This chapter covers many topics, such as basic concepts of the mathematical programming method, finite element error estimation, stress recovery techniques, design sensitivity analysis, and data smoothing methods.

We must emphasize that one of the objectives is to shed some light on the development, implementation and applications of adaptive mesh refinement (AMR). The error estimation, the stress recovery and AMR procedures are presented in Chapter 3. There, a compact form of a linear system of equations is developed for easy programming and the implementation details of stress superconvergent patch recovery (SPR) for both triangular and quadrilateral elements are provided. Examples are included to illustrate the applications in adaptive mesh generation. It is noted that the developed stress recovery technique is also used in Chapter 7 to predict the accurate in-plane stress field and further to calculate the critical lateral buckling factor for a number of different plate configurations. In these applications, the finite element plate models are constructed from the Reissner-Mindlin thick plate theory, which is outlined in the second part of Appendix A.

A reliable tool for design sensitivity analysis is a prerequisite for performing structural optimization design. Efficient and reliable methods for design sensitivity analysis of all implemented analysis types and finite element types must therefore be developed and implemented. In Chapter 4, we present a compact form of the design sensitivity analysis formulation. The well-known maximum shear stress and the von Mises stress are widely used failure criteria, and the formulation is orientated toward these two criteria for computational efficiency.

Direct use of a single design point movement predicted from the optimization solver generally leads to an unrealistic boundary shape that contains many kinks. To remedy this, a smoothing process is described in Chapter 5 and has been used through this work. There, the dual kriging B-spline fitting procedure is used from the given set of data, a covariance function and a prescribed number of control polygon points. The polygon points are next determined and a set of smoothed nodal points are then computed. It is emphasized that the results of a fitted curve caused by modifying the locations of the control polygon points are not always obvious, as opposed to modifying directly points on the curve itself. This was a main reason why this work did not employ the control polygon points as the primary tool to optimizing a structural boundary as many shape optimization works did. Furthermore, the dual kriging fitting technique guarantees that the fitted curve or surface has not only high quality as a traditional B-spline fitting technique produces, but also passes through the data points. A number of applications in 3-D curve and surface fittings are also presented in this chapter.

Chapter 6 is devoted to introducing the proposed node-based shape optimization methodology along with some implementation considerations. As will be seen, the method requires very little effort from users to set up the initial model. As a matter of fact, the only user input required is to provide an initial coarse boundary model and a set of boundary segments allowed to be modified to achieve an optimal shape. Then, the rest of designing processes is automatically executed.

Chapter 7 contains a number of example applications of structural problems to demonstrate the validity of the methods derived in the preceding chapters. While some examples are included to emphasize the importance of using the developed error estimation technique, a number of examples are also devoted to structural shape optimization designs.

The conclusions of this research and recommendations for future work are given in Chapter 8.

The finite element library used for this dissertation has facilities for solution of linear types of static, stability and dynamic analysis problems for 2-D structures, i.e., static stress analysis, linear buckling analysis and natural frequency analysis. The code was developed by the author during his graduate study. Many different isoparametric finite elements are described and implemented in the system. A brief description of the planar and the Reissner-Mindlin plate finite element theories and programming implementation are summarized in Appendix A for easy reference and notation purpose.

A brief account of surface-area based parametrization theory and a numerical finite difference formulation of Gaussian and mean curvatures is presented in Appendix B. These techniques have important applications in 3-D the dual kriging curve and surface fittings.

2 LITERATURE SURVEY AND REVIEW

2.1 General

Over the last two decades, various numerical shape optimization techniques have been developed and applied to mechanical and structural design. This is most fundamentally due to the requirements and expectations from designer and customer standpoints that structures should be efficiently and economically designed and manufactured. A literature survey on structural optimization primarily oriented toward shape optimization of both planar and plate structures is presented first. Next, we introduce several concepts and techniques that are fundamental to the successful development of a structural shape optimization design and their important roles are emphasized.

It should be pointed out that the field of structural shape optimization is still a relatively new field undergoing rapid changes in methods and applications. Though a substantial number of research articles have appeared in this field, a relatively small number of real structures have been analyzed. This imbalance may result from the fact that a meaningful shape optimization requires a substantial amount of experience in structural design to formulate the problem in an adequate form.

2.2 Literature Survey of Shape Optimization

The survey is conducted in three parts: the techniques for planar structures and for plate structures that are developed by combining the traditional FE solution procedure and numerical optimization analysis. The third part briefly discusses other concepts and techniques in the literature used to reach an optimal shape design.

2.2.1 Planar Structures

The subject of numerical shape optimization has been a topic of in-depth research for over two decades. In the early stage of its development, a straightforward procedure was adopted in which a set of nodal coordinates within the structure were considered as design variables. Zienkiewicz and Campbell [86] presented one of the first examples of using such an approach. They calculated design sensitivities by using the semi-analytical method and used sequential linear programming for numerical optimization. The optimum shapes of dams and rotating turbine machinery were demonstrated. Though simple and instinctive, this technique has two serious drawbacks: it often results in a large number of design variables so that only relatively simple structures can be handled; and, because it is difficult to maintain an adequate FE mesh during the optimization iterations, the elements may suffer severe distortions that can introduce inaccuracy into structural analysis.

Various shape representations were then proposed to reduce the number of design variables. The early success in using a specific shape representation for particular structural boundaries was demonstrated by Kristensen and Madsen [48] for a class of shape optimal designs. Polar coordinates and orthogonal polynomials were used to locate boundaries and the coefficients in these polynomials were treated as design variables. With this approach, the number of design variables was reduced dramatically because a few design variables could be used to control the boundary shape and element distortions were also prevented. An example given by Bhavikatti and Ramakrishnan [15] employed six coefficients of a fifth-order polynomial as design variables to conduct optimum shape investigation on the outer boundaries of rotating disks.

It is known that the representation of a curved boundary by a high order polynomial may result in an oscillatory boundary shape. Use of the spline functions can eliminate oscillation since spline functions are composed piecewise of low order polynomials. The two most popular members in the spline function family are Bezier and B-spline functions. The work by Braibant and Fleury [18] was the first one in which a systematic approach was outlined to demonstrate the use of Bezier and B-spline functions in structural shape optimization. Note that in such an optimization design method, the polygon points were generally used as the design points. In our proposed node-based method, however, the design points consist of the structural boundary nodes. Furthermore, a general B-spline curve or surface fit does not necessarily pass through the data points. The dual kriging fitting technique, on the other hand, guarantees that the fitted curve or surface not only has high quality of a B-spline fit, but also passes through the data points. This powerful method will be reviewed and detailed later.

A popular alternative of reducing the number of design variables, proposed by Imam [40], is to use the design element concept. With this approach, a structure is first divided into a number of small element blocks and some of these blocks are allowed to be altered to yield the optimal shape. The interior nodes in the design elements are generated by using isoparametric shape functions or geometric blending functions. Another benefit brought up by this methodology is that the initially coarse mesh can be refined in each design element. Its disadvantages are obvious too, however, it may be difficult to establish a fully automatic process given that the number and the locations of the predetermined design elements may be required to be modified to cope with the varying boundary shapes. Furthermore, incorporation of a local refinement within a single design element into the global FE model generally imposes a major bookkeeping load. Consequently, application of the shape optimization procedure based on the design element concept must in general be restricted to designs with small shape changes.

Numerous researchers have made significant contribution to shape optimization algorithms and applications in the last twenty years. Two survey papers and a conference proceedings, all published in 1986, reflect various research activities in optimal shape design up to the mid 1980's. Ding [27] collected eight types of 2-D and 3-D structural examples successfully solved by the shape optimization techniques. These included the minimum weight design of a bridge, the maximum von Mises effective stress design of a spherical pressure vessel, the maximum reference stress design of a shoulder fillet, the minimum weight design of a torque arm and bracket, the minimum weight design of a plate with a hole, the minimum weight design of a plate bridge, the minimum volume design of concrete in a round head buttress and arch dam, and the optimal ratio of the maximum and minimum stress design in a four-spoked disk. It should be emphasized that none of these applications employed an adaptive FE modeling technique.

Haftka and Grandhi [35] emphasized the difficulties which are encountered in shape optimization and which are not present or are easier to solve in sizing design. They collected 139 references and included a table which summarized sixteen areas of shape optimization application: beams, brackets, columns, connecting rods, cross-sectional shape in torsion, dams, disks, engine main bearing caps, fillets, plate with a hole, pressure vessel components, rotating turbine machinery, shells, stress concentration minimization, torque arm, and turbine and compressor blades.

The symposium sponsored by GM Research Labs [13] emphasized the then state-of-the-art and future developments of shape optimization and its applications. The interesting thing to note in this proceedings is that it began with an article on adaptive analysis refinement and error estimation. Topics covered in the symposium included adaptive analysis refinement, shape design sensitivity analysis, modeling, and applications for shape optimization. It was also concluded that although many other methods may be used for structural shape optimization, most researchers shared confidence in the use of FEM as a tool for structural analysis and in the use of mathematical programming procedures as the ultimate algebraic minimization tool.

Belegundu and Rajan [9, 59] developed a method based on fictitious loads acting on an auxiliary structure. One of purposes of employing this auxiliary system is to provide the smooth mesh translations for the varying structural shapes during optimization iterations by altering the preceding meshes, in an attempt at avoiding an overall structural remesh. It should be pointed out that this author applied this method in the early stage of his studies with only limited success. It was found that a periodic remesh is still often necessary to avoid excessive distortion in the mesh system.

Great strides have been taken toward shape optimization since these surveys.

Among many journal and conference articles, the following several applications are emphasized due to their uniqueness. Cheu [22] considered shape optimization of axisymmetric structures subject to thermo-mechanical loads. The applied problem is the optimal shape design of a rotating disk. Andrews [3] considered the minimization of fillet stresses due to bending for an epicyclic gear system consisting of basic rack, pinion cutter, and gear teeth. The design variables included the pressure angles and a median height factor. Schramm and Pilkey [66] applied shape optimization methodology in designs of beam cross sections subject to an applied torsion load. They used non-uniform rational B-splines to describe the beam boundary shapes.

2.2.2 Plate Structures

The literature cited above addresses shape optimization applications in planar structures under the constraints associated with in-plane displacements and membrane stresses. When out-of-plane bending effects become important, such a structure is referred to as a plate structure in this work. Most of the early developments in numerical plate optimal shape designs were summarized in the survey paper by Haftka and Prasad [34]. Besides stress and displacement constraints as in a planar optimization, they also emphasized the necessity of buckling and vibration constraints in practical plate and shell structural designs. Also, they mentioned some difficulties in achieving an optimal solution.

It should be pointed out that only a limited number of successful stability and vibration optimization applications in plate structures have been reported in the open literature. Among them, the design procedures developed by Vanderplaats and his associates have been the most applicable and practical. By refining the force approximation method originated by Schmit [65], they have made a number of important contributions to numerical optimal designs of shape and sizing for truss, frame and shell structures subjected to static, vibration and buckling constraints [76] and 3-D general continuum structures subjected to constraints on von Mises stresses [42, 43, 44]. They showed that the force method for a static stress constrained structure offers a high quality approximation that is able to capture some of the constraint nonlinearities without the need for high order sensitivity analysis. Recently Gates and Accorsi [31] also applied this type of modeling to a rib-stiffened cylinder design.

2.2.3 Other Optimization Methods and Applications

Shape optimization problems may also be solved in direct conjunction with variational statements, that is, with classical analytical formulations. Prager [58] is generally credited with motivating this line of research. The representative work in this classical approach can be found in the books by Haslinger and Neittaanmaki [37] and Banichuk [6].

The boundary element method (BEM), combined with an optimizer, also has been applied to shape optimization [84]. As is known, BEM is less versatile for structural analysis than FEM, but, more accurate prediction of the design sensitivities, stresses, and displacements can be made at the boundary.

Shape optimization has also been applied to three-dimensional structures. In this case, the modeling plays a key role in the successful optimization. Botkin and Bennett [17] treated a three-dimensional part as an assembly of the two-dimensional segments, referred to as the stamped model. Their approach could be viewed as a novel application of plate and shell optimization. Three optimal shape design examples were shown in the aforementioned reference: an engine bearing cap; a transmission bracket; and an engine connecting rod. It should be noted, however, that in general a three-dimensional structure has to be modeled by a solid modeling technique. The idea of using entities that define the geometric primitives of a solid object as design variables has been applied by Kodiyalam and coworkers [43]. Their results include design examples such as a fixed-fixed beam structure under a constant pressure load; an engine connecting rod; an aircraft turbine disk; and an automotive control arm.

2.3 Review of Shape Optimization Techniques

We begin with a general formulation for structural optimization within the framework of the mathematical programming technique. The feasible direction method is then outlined in such a way that it is consistent with the major steps of the CONMIN routine, developed by Vanderplaates [74]. This will be followed by a brief introduction of fundamental concepts and techniques that represent modules in this research and in most structural shape optimization packages. The introduction emphasizes the role that each module plays in the development of numerical shape optimization.

2.3.1 Mathematical Programming Technique

A structural shape optimization problem can be described as the minimization of an objective function subject to a number of prescribed constraints. It may be stated mathematically as

$$\text{Minimize } F(\{p\})$$

$$\text{Subject to } g_i(\{p\}) \leq 0, (1 \leq i \leq N_c) \tag{2.1}$$

$$p_i^l \leq p_i \leq p_i^u, (1 \leq i \leq N_d)$$

where F and g_i are the objective function and the constraint function, respectively. The N_c constraints described by Equation (2.1) impose the limits involving, for example, the nodal displacements, the stress components, and the natural frequencies. The N_d components of the vector $\{p\}$ represent the design variables that are chosen to describe the shape of the structure that is to be optimized. The values of p_j^l and p_j^u are the lower and upper bounds of the design variable, usually referred to as side constraints in the literature. Here, it is also assumed that any geometrical constraints such as boundary slope continuity are included in these constrained equations.

The CONMIN routine [74, 75] uses the method of feasible directions to search for a local optimum. A search direction is determined first, and then the distance to move in that direction is determined that reduces the design objective the most, while not violating any constraints. In this study, the computed gradients of the design objective and constraints with respect to the design variables are fed directly into the CONMIN routine. A general representation in the mathematical programming method for a structural optimization and the essential ingredients of the method of feasible directions consistent with the routine are given in the above-mentioned references.

A constraint g_i is referred to as an active, or violated, one if $g_i = 0$ or $g_i > 0$. This theoretical definition is of little use during numerical evaluation since a precise zero is seldom achievable on a digital computer. In actual calculation, a tolerance band about zero is selected for defining when a constraint is active. In this study, the constraint is considered active or violated if

$$C_{il} \leq g_i \leq C_{iu} \tag{2.2}$$

or

$$g_i > C_{iu} \tag{2.3}$$

where the numerical values of bounds C_{tl} and C_{tu} are set to be -0.01 and 0.004, as suggested by Vanderplaats [74].

The objective function may be selected in many ways. In this study, the area of the underlying two-dimensional planar structure is selected as this function. On the other hand, a desirable range of a specific natural frequency can be formulated into a suitable form of the objective function. We emphasize that under the mathematical programming framework, the objective function and the constraint functions may be linear or nonlinear, explicit or implicit functions of the design variables, but must be continuous and should have continuous first derivatives.

Various sources [75, 36] may be consulted for in-depth discussions about mathematical programming techniques, their numerical implementation, and broad applications to engineering problems; the works by Tseng and Arora [71, 72] are particularly recommended.

The method of feasible directions was developed originally by Zoutendijk [92] and has been modified and used by Vanderplaats [74] in his popular CONMIN optimization program. It should be mentioned that this type of method may not be applied directly to a problem with any equality constraint. An equality constraint, $g(\{p\})=0$, may be approximated by two inequality constraints as

$$g_1(\{p\}) \equiv g(\{p\}) - \varepsilon_1 \le 0$$
$$g_2(\{p\}) \equiv -g(\{p\}) + \varepsilon_2 \le 0 \tag{2.4}$$

where ε_1 and ε_2 are small prescribed positive numbers. A more sophisticated method of including this equality constraint was developed by Kreisselmeier and Steinhauser (cf. [36]). One of the major advantages in using this method is that it does not increase the number of constraints.

2.3.2 Error Estimation and Adaptive Mesh Generation

It is known that a robust estimation of the accuracy of the finite element solutions plays an important role in successful structural optimization because the predicted values of displacements and stresses are required to guide optimization directions. It has been established that FE approximation error converges to zero as the number of nodal points increases and the areas of elements in FE mesh decreases. How can the amount of error be quantified properly and how is the mesh refined?

As is known, the direct product of a displacement-based FE method is the displacement and the by-products include reaction force, stress, and strain. Any one or several of these products may be used for error estimation purpose. Overall refinement of a coarse mesh system is, however, uneconomic since such an overall-refined model may require an unrealistically expensive computational effort and, in most cases, is unnecessary since it is most likely that only a few regions in a model require such highly-refined local meshes to obtain adequately accurate solutions. These are the questions an adaptive mesh refinement method (AMR) tries to answer. It is generally understood by now that AMR should include at least two parts. The first part is for estimating the errors in each individual element which can be summed up to yield a global error estimation; the other part is designed to guide the mesh refinement based on the above estimating results. It has commonly been accepted that the error estimation should be conducted on those quantities associated with the gradients of the obtained displacements. As a result, a proper AMR is generally required for efficient computation and accurate prediction of both displacements and their gradients (stresses and/or strains).

The importance of the gradients can also be reflected in evaluating constraints. Most of the critical constraints are typically associated with stress components in a structural shape optimization analysis. These stress components may be recovered from the displacements at nodal points solved by the FE equations. It was found by Barlow [7] and Hinton [39] that this nodal recovery led in most cases to stresses with gross errors and it was concluded that the stress recovery process should be conducted at the Gauss integration points used in the numerical integration for forming the stiffness matrix. The stresses at other points (including nodal points) of the element should then be formed by interpolation and/or extrapolation.

The calculation of more accurate stress solution has been one of the most active research fields in the finite element analysis community for many years. The more promising method, superconvergent patch recovery (SPR), was proposed by Zienkiewicz and Zhu [85, 91] and over the years has become a primary stress recovery method in commercial finite element analysis packages. This author and his supervisor have modified the original SPR method and extended it into an automatic 2-D adaptive mesh generation program. Briefly, the SPR method leads to a superconvergent estimate for the smoothed stress at an edge node by patching together the elements surrounding that node and employing a local least-squared fitting technique.

Description of the error estimation and SPR used in this research is presented in Chapter 3 along with implementation considerations.

2.3.3 Design Sensitivity Analysis

Design sensitivity analysis is another main topic in shape optimization. The purpose of this analysis is to quantify the variations of responses of a structure with respect to changes in the design variables. It provides the derivatives of the objective function and constraints with respect to the design variables, which is the essential information required in using a mathematical programming solver. It is also noted that the calculation of the design sensitivities of the structural response is often the most computationally intensive part of an entire optimization process, consequently, it is important to design an efficient algorithm for these calculations.

Implicit (or discretized) and variational (or continuum) methods are two popular approaches in calculating design sensitivities. The implicit method was first proposed in [86] and was based on manipulating the discretized FE equations. Its implementation requires the derivatives of the stiffness matrix and force vector. There are two approaches in computing these derivatives. One is based on the finite difference argument, referred to as the semi-analytical method in the literature, in which numerical differentiation of stiffness matrix is formed by a forward or central finite difference scheme. The other is applicable only to the isoparametric model and is referred to as the analytical method, in which the analytical expressions of the derivatives are derived for each entity of the stiffness matrix and the force vector.

It has been reported [36] that the semi-analytical method may suffer inaccuracy in a shape optimization process in modeling beam, plate, shell, and higher-order accurate finite elements, especially as the mesh is refined. Note that these models possess both translational and rotational degrees of freedom. It was concluded recently by Olhoff and coworkers [57] that the cause of this phenomenon is related to the negative powerness of the design variables contained in the components of the stiffness matrix. Consequently, they proposed a new method for "exact" semi-analytical design sensitivity analysis, which was claimed to completely eliminate inaccuracy associated with the traditional semi-analytical approach. It is noted that the design variables in the sizing optimization, such as the cross-sectional areas of a truss element and the thickness of a plate element, are usually included in the stiffness matrix as simple linear functions. As a result, the semi-analytical method used in the sizing optimization results in an adequate sensitivity analysis.

The variational approach, which was introduced in the late 1970's by Haug and coworkers [38], starts from the fundamental principle of virtual work on which the FEM was based to estimate the effect due to the change of design variables. This approach was originally developed with the help of a material derivative. It was claimed that the variational approach may yield relatively accurate sensitivity analysis. It was found, however, that a difficulty arises in applying this approach to a structure under concentrated loads since the solution of the adjoint problem, which is a necessary step in applying the approach, leads to singular adjoint loads. As a result of this singularity, some local averaging technique must be used and the accuracy in the smoothed results may be questionable, especially for stress sensitivity analysis. Recently the control volume from fluid dynamics was also proposed and the results were compared with these using material derivative by Arora *et al.* [4]. Comparisons between implicit and variational approaches can be found in a number of articles [e.g., 83, 24]. Two review articles [1, 82] can be consulted for more details.

In his research, this author has developed straightforward sensitivity formulae for stress constraints arising from von Mises stress and maximum shear stress criteria. They were successfully used in several shape optimization applications, as demonstrated in the following chapters.

2.3.4 Dual Kriging B-spline Fitting

In recent years, the B-spline method has rapidly become one of the most important curve and surface fitting techniques. Major advantages associated with a B-spline curve, compared to other spline formulations, are its flexibility and its variation diminishing property [63]. Kriging is a statistical estimation method, first proposed by Krige [47] for applications in mining engineering. This technique consists of describing the interpolating function by two parts: a draft function and a covariance (or variogram) function. The goal is to establish a minimum variance, unbiased estimate of the value of a random variable at one location from values available at surrounding locations. A major advantage of the kriging approach is that it is an exact interpolator. Typical applications of kriging method include map analysis [26] and contouring [28] in geology.

Matheron [52] and Watson [80] demonstrated the formal equivalence of cubic spline interpolation and the kriging technique and concluded that the spline solution could be derived via kriging under certain conditions. Since then, the dual formulation of the primal kriging equations, called the dual kriging technique, has been applied as an interpolation technique. Gilbert, *et al.* [32] applied dual kriging to the calculation of the optimum angle for displays and to the surface representation of the arm by using simple linear and trigonometric functions as the draft function. Montes [54] used Bezier spline functions as the draft function to investigate dual kriging curve interpolation and to establish the connection between Bezier curves and the dual kriging interpolation scheme. He also demonstrated the application of constraints associated with slope requirements at certain points.

Recently, Limaiem and El Marghy [50] applied the dual kriging technique to curve, surface and solid fitting. The theory presented by Gilbert, *et al.* [32] was refined to such an extent that the formulation could be applied directly. Limaiem and El Marghy also demonstrated that this method has a broad spectrum of practical applications. Unfortunately, their presentations are limited to such applications with uniform parametrization. A detailed account of this powerful technique will be presented in Chapter 5. There can be found many applications of this method in 3-D curve and surface fittings. One of our purposes there is to point out that the dual kriging technique can be applied in conjunction with a broader class of parametrization methods.

3 ERROR ESTIMATION AND ADAPTIVE MESH GENERATION

3.1 General

Theoretical description of error estimation and stress recovery is first presented in this chapter. This will be followed by a subsection dealing with mesh refinement procedure, which is orientated toward a triangular mesh system. An automatic triangular mesh generator is used as the main part of an adaptive automatic mesh generator. The applications of this technique are given in Chapter 6 and the node-based shape optimization method is presented in Chapter 7 where the lateral buckling loads of plate structures are considered.

In general, the calculated element stresses and strains based on the FE solution are discontinuous at the interface of two elements. For a homogeneous domain, however, it is expected that the exact stress and strain should be continuous functions across elements. The error due to a FE solution in each element is generally measured by the difference between the stresses resulting from the smoothed solution, denoted by σ^*, and the FE solution σ. It is noted that the strains can also be used for the error estimation for a homogeneous domain.

3.2 Theoretical Development

In this work, the elemental error is defined in terms of the energy norm by

$$E_e = \left[\frac{1}{2} \int_{\Omega_e} (\{\sigma^*\} - \{\sigma\})^T [C]^{-1} (\{\sigma^*\} - \{\sigma\}) \mathrm{d}\Omega \right]^{\frac{1}{2}} \tag{3.1}$$

where the vector $\{\sigma^*\}$ denotes the smoothed FE stress vector $\{\sigma\}$, whose representative function form will be given shortly. $[C]$ represents the constitutive matrices of the plane stress problem, The global error is the root-mean-square summation of the elemental errors

$$E = \left(\sum_{e=1}^{NE} E_e^2 \right)^{\frac{1}{2}} \tag{3.2}$$

To identify the element(s) in which the FE solution suffers from large error(s), a relative percentage error is defined as

$$\eta_e = \frac{E_e}{\left[\left(E^2 + S^2 \right) / NE \right]^{\frac{1}{2}}} \tag{3.3}$$

where

$$S = \left[\frac{1}{2} \int_{\Omega} \sigma^T [C]^{-1} \sigma \, \mathrm{d}\Omega \right]^{\frac{1}{2}}$$

$$\Omega = \sum_{e=1}^{NE} \Omega_e \tag{3.4}$$

represents the strain energy resulting from the FE solution. A value of 0.05 is usually chosen as the allowable upper bound $\bar{\eta}$ for η_e from Equation (3.3) in most of applications. If any elemental error indicator η_e is greater than the bound $\bar{\eta}$, then that element needs refining. Let us denote the area of the trouble element as A_e, the area required after the refinement can be expressed by

$$A_e^r = \left(\frac{\bar{\eta}}{\eta_e} \right) A_e \tag{3.5}$$

To better illustrate the determination procedure of the smoothed stress function σ*, plane stress is taken as an example. Assume a functional approximation to the smoothed stresses with

$$\sigma^{*T} = \{\sigma^*_{xx}, \sigma^*_{yy}, \sigma^*_{xy}\} = \{p\}^T \left[\{f_{xx}\}, \{f_{yy}\}, \{f_{xy}\} \right] \tag{3.6}$$

where the vector $\{p\}$ consists of polynomial base functions in the global x and y coordinate system. The vectors $\{f_{xx}\}$, $\{f_{yy}\}$ and $\{f_{xy}\}$ represent coefficient vectors to be determined. It is noted that the above equation can also be represented in a compact form by

$$\sigma^* = [P(x, y)]\{f\} \tag{3.7}$$

where

$$[P(x,y)] = \begin{bmatrix} \{p\}^T & & \\ & \{p\}^T & \\ & & \{p\}^T \end{bmatrix}$$

$$\{f\} = \{\{f_{xx}\}^T, \{f_{yy}\}^T, \{f_{xy}\}^T\}^T \tag{3.8}$$

To compute the estimate $\{\sigma^*\}$ inside the patch, the following function is minimized

$$F(\{f\}) \equiv \sum_{e=1}^{N_1} \sum_{i=1}^{n_e} w_i \left(\{\sigma_i^*\} - \{\sigma_i^e\}\right)^T [C]^{-1} \left(\{\sigma_i^*\} - \{\sigma_i^e\}\right) \tag{3.9}$$

where N_1 denotes the number of elements defining the current patch, and n_e is the number of Barlow points used in the element to calculate the FE stress $\{\sigma^e\}$ in the e-th element. w_i denotes the weight value in the Gaussian quadrature of the integration. By making use of the expressions for the smoothed stress vector

$$\{\sigma_i^*\} = [P(x_i, y_i)]\{f\} \tag{3.10}$$

and

$$\{\sigma_i^e\} = [C][B^e(x_i, y_i)]\{q^e\} \tag{3.11}$$

one can reduce Equation (3.9) to

$$F(\{f\}) \equiv \sum_{e=1}^{N_1}\sum_{i=1}^{n_e} w_i \left([P(x_i, y_i)]\{f\} - [C][B^e(x_i, y_i)]\{q^e\}\right)^T [C]^{-1}\left([P(x_i, y_i)]\{f\} - [C][B^e(x_i, y_i)]\{q^e\}\right) \quad (3.12)$$

where $[B]$ represents the strain-displacement matrices of the plane stress problem; the superscript e highlights an association with the e-th element. The minimization of Equation (3.12) yields a linear system of equations

$$[A]\{f\} = [D] \quad (3.13)$$

where the coefficient matrices can be expressed by

$$[A] = \sum_{e=1}^{N_1}\sum_{i=1}^{n_e} w_i [P(x_i, y_i)]^T [C]^{-1} [P(x_i, y_i)]$$

$$[D] = \sum_{e=1}^{N_1}\sum_{i=1}^{n_e} w_i [P(x_i, y_i)][B^e(x_i, y_i)]\{q^e\} \quad (3.14)$$

The proper choice of the vector $\{p\}$ depends on the type and the order of the finite elements used in forming the stiffness matrix. Also, these variables have a great effect on the implementing details when the current SPR approach is used. Therefore, two subsections are devoted to covering them.

3.2.1 2^{nd} -Order Triangular Element

From our limited experience, it was found that in most applications, a patch can be adequately represented by a 2^{nd} complete polynomial, that is

$$\{p(x, y)\} = [1, x, y, x^2, xy, y^2]^T \quad (3.15)$$

It is noted that it requires that the number of integration points associated with the patch is not less than six, as depicted by Figure 3.1(a), or the interior integration scheme is used, as shown Figure 3.1(b). Otherwise, the following reduced complete polynomial

$$\{p(x,y)\} = [1, x, y]^T \tag{3.16}$$

is recommended, for instance, at the corner of the structure, as shown in Figure 3.1(b), and Figure 3.1(c) if the edge integration scheme is used. It is worth mentioning that no apparent advantage was observed by making use of the third or higher-order complete polynomials. To avoid the potential ill conditioning in the least square fitting calculations, the integration points associated with a patch is linearly translated into a two by two square centered at point (0,0). Also, stresses are normalized to maintain the same magnitude on both sides of the least square equation.

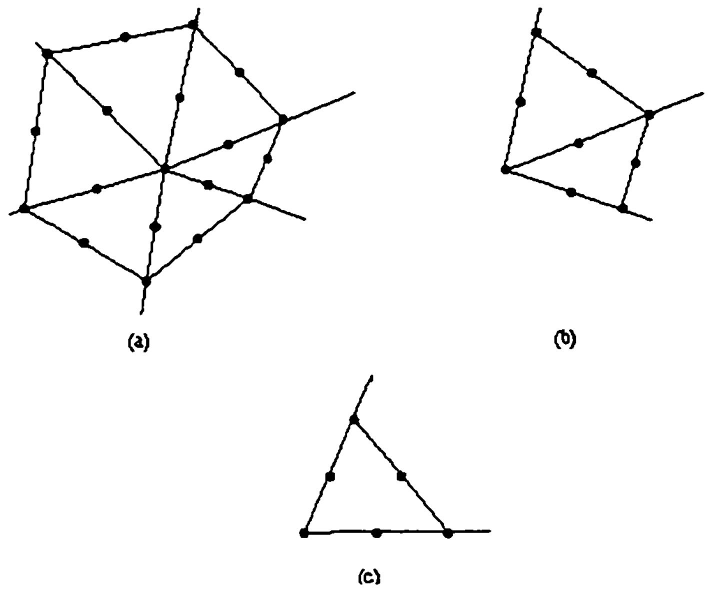

Figure 3.1: Triangular element patches

It is noted that the recovery stress vector $\{\sigma^*\}$ contains information at the integration points. An element may be associated with the same number of patches as the number of apex nodes. Consequently each of these patches contributes a different $\{\sigma^*\}$ at the same integration point. A quick remedy is achieved by taking the averaged values from these patches. However, it is felt that the following procedure is more robust since it takes into account the relative effects resulting from the distance between the integration points and the finite element nodes. For each element, $\{\sigma^*\}$ may be computed at the integration points for each apex node. A single $\{\bar{\sigma}^*\}$ at each integration point inside the element can then be calculated by

$$\{\bar{\sigma}^*\} = \sum_k \begin{bmatrix} N_k & & \\ & N_k & \\ & & N_k \end{bmatrix} \{\sigma_k^*\} \tag{3.17}$$

where N_k are the shape functions associated with the apex nodes of the element. The stress components at a node can next be recovered using stress information at the integration points.

3.2.2 2^{nd} –Order Quadrilateral Element

A complete polynomial of up to 4^{th} order (containing 15 coefficients) was used for the vector $\{p\}$ if there are enough Barlow points available in the patch. The recovered stresses at eight points were then used to calculate the stresses at the required nine integration points from the eight-node isoparametric shape functions. It should be pointed out that the number of integration points in a full integration of Equation (3.13) depends on the order of the polynomial used for recovering the stresses. If the stress recovery vector for $\{\sigma^e\}$ is a 4^{th} order complete polynomial, a 4 by 4 integration point stencil may be used to evaluate Equation (3.13) numerically for the purpose of accuracy.

We have so far applied the automatic adaptive mesh generator to the structural model consisting of only straight-sided triangular elements (subparametric elements). For element refinement, the *h*-refinement was exclusively used in the present work. In other words, an element in the previous mesh system is divided into smaller elements by adding a certain number of nodes within the element. Such a procedure inevitably requires a more involved bookkeeping algorithm to store the information on new generated nodes, elements, and their connections.

A 2-D Delaunay triangulation was included to accomplish the mesh generation and its subsequent refinement. The mesh quality is controlled by a given value of the minimum elemental angles.

Before turning to the topic of validation, it is worthwhile to mention two other refinement approaches. Belegundu and Rajan [9] proposed a simple refinement method based on a fictitious loading concept in which the mesh was updated during the optimization process by solving an additional finite element model with a fictitious load system. With their approach, no error estimation is required. This author has implemented this method in the early stage of this work and found that it is necessary to apply mesh regeneration periodically to prevent element distortions from becoming excessive. Another approach, developed by Kikuchi, Taylor, and their coworkers [41], was intended to achieve an optimal AMR process by combining AMR and a mathematical programming solver.

3.3 Validation

The developed error estimation and AMR techniques are validated by considering two models. The first example concerns a square plate with a center square hole and the plate is under the biaxial tensile loading condition. The initial triangular mesh is shown in Figure 3.2 and the refined ones in Figure 3.3(a) and (b). As evident, the coarse mesh is properly refined near the high stress regions. Figure 3.4 and Figure 3.5 show the detailed views of the first and the second refinements near the singularity point. It should be pointed out that these two figures suggest that the refinement should be an iterative process.

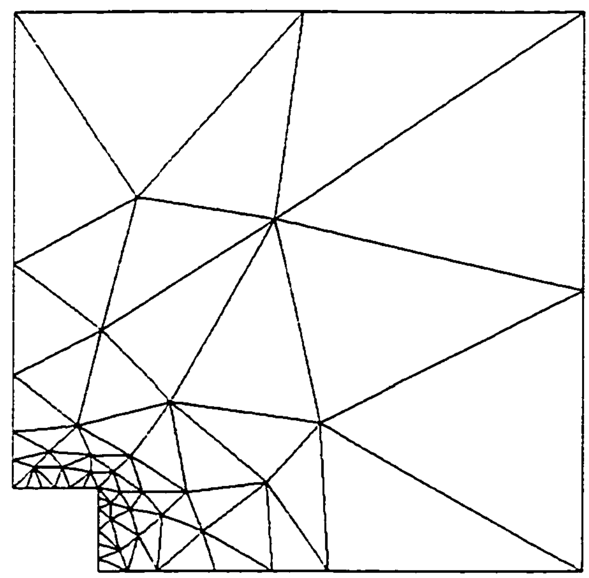

Figure 3.2: Initial mesh of plate model

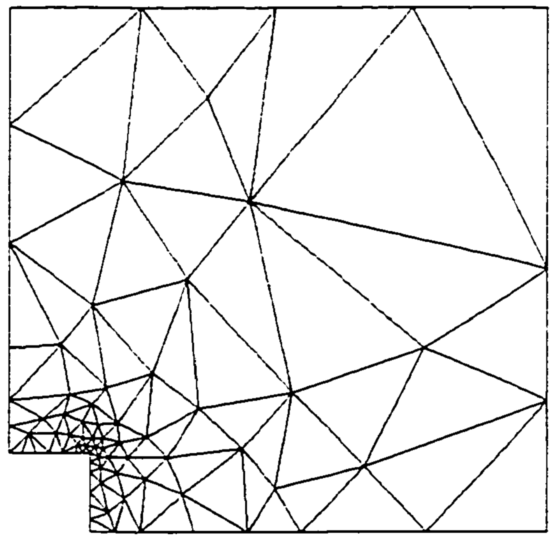

(a)

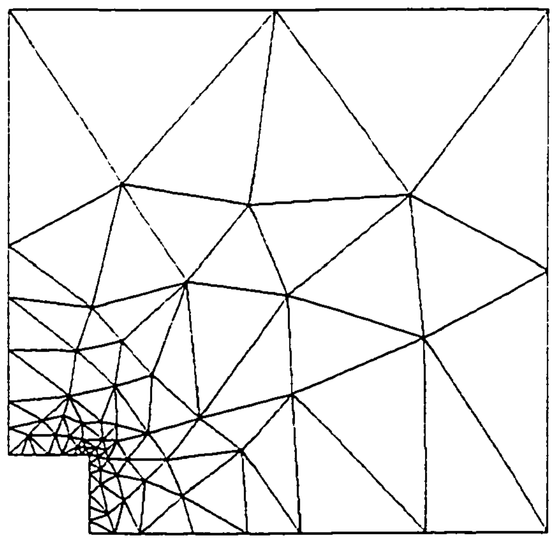

(b)

Figure 3.3: Mesh from the first refinement with
(a) edge integration scheme; (b) interior integration scheme

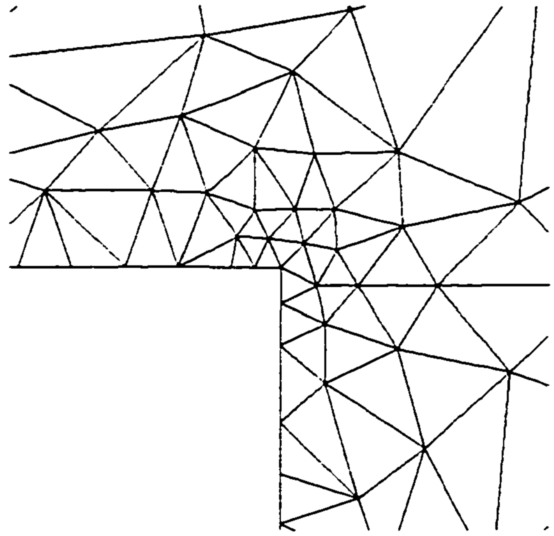

(a)

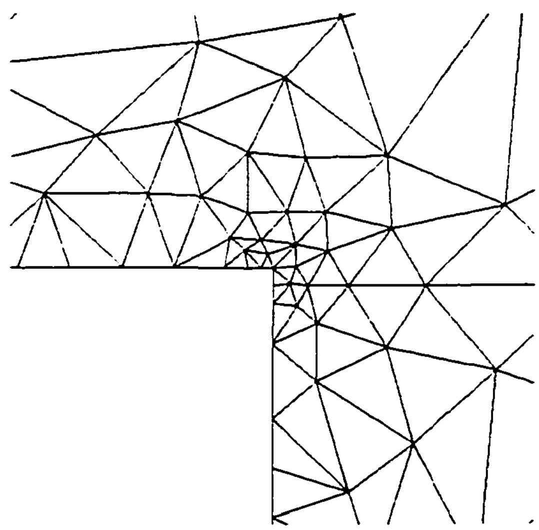

(b)

Figure 3.4: Mesh with edge integration scheme from the
(a) first refinement; (b) second refinement

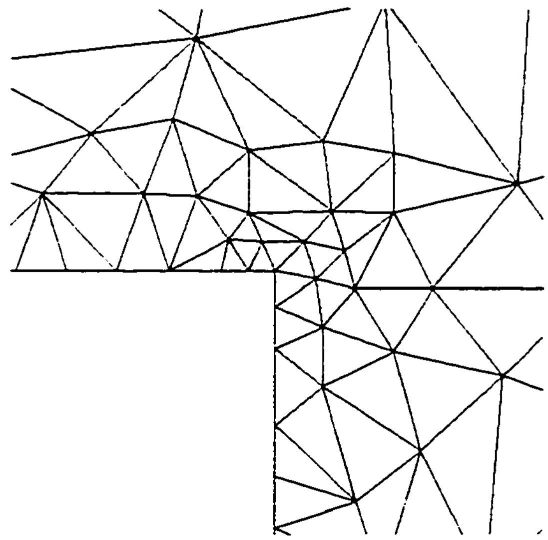

(a)

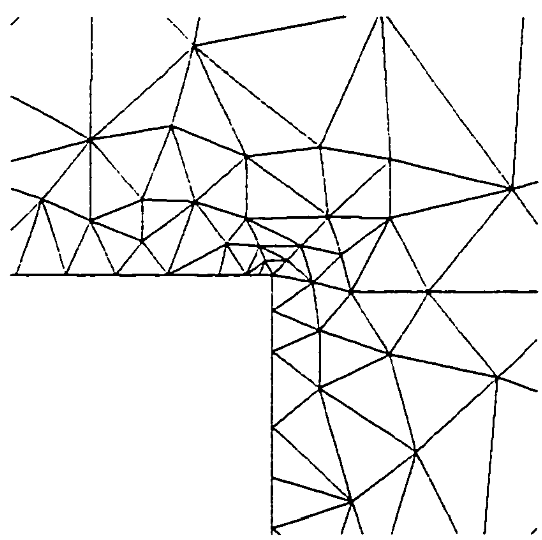

(b)

Figure 3.5: Mesh with interior integration scheme from the
(a) first refinement; (b) second refinement

The next application is on a bracket model, as shown in Figure 3.6. The initial mesh, which consists of 338 nodes and 141 six-node triangular elements, and its refinement (1167 nodes and 532 elements) are depicted in Figure 3.7(a)-(c).

The results of the verification and validation tests were favorable, thereby indicating the FE module and adaptive mesh generator module can be used to model structures adequately.

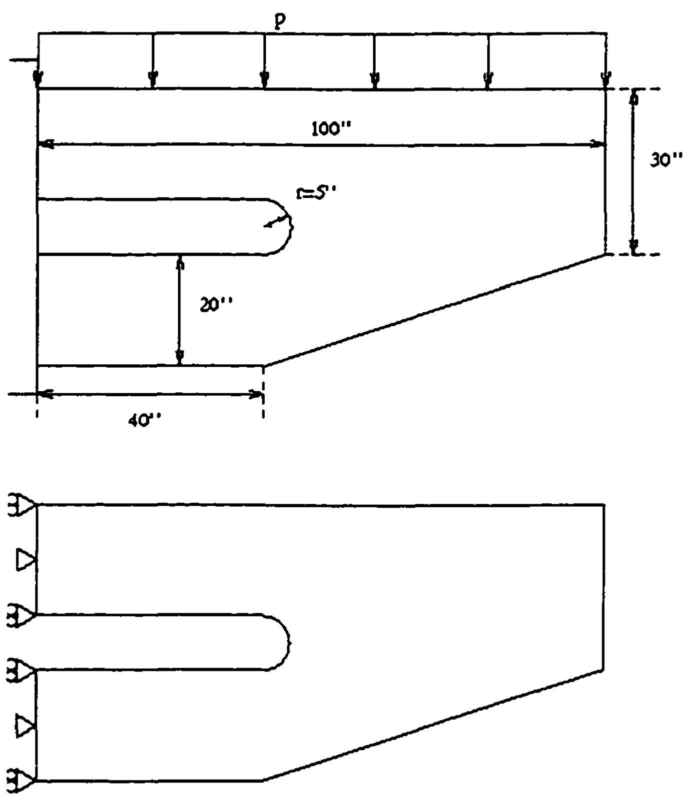

Figure 3.6: Plane stress bracket model

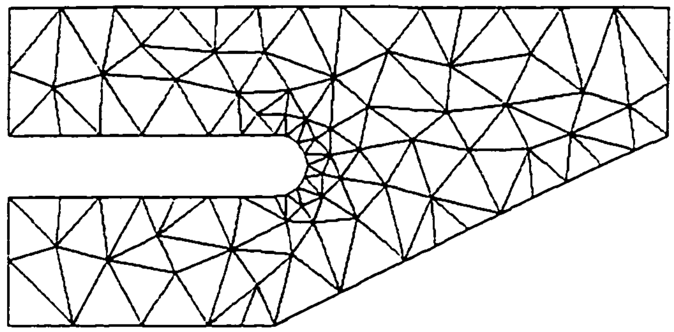

(a)

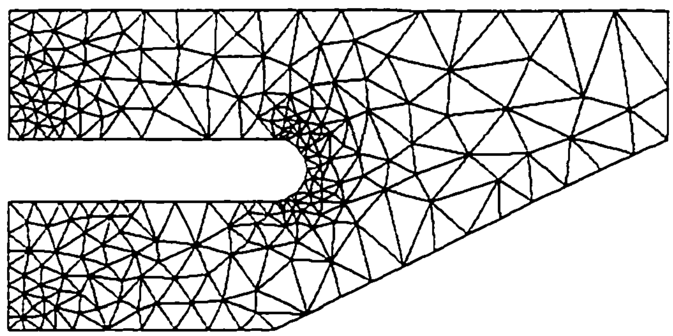

(b)

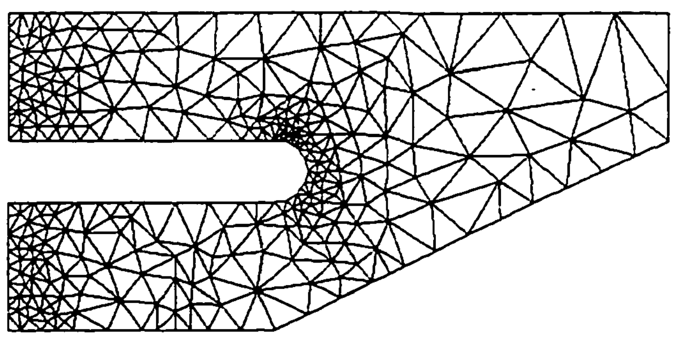

(c)

Figure 3.7: Meshes and the first refinements of bracket model

(a) initial mesh; (b) mesh from interior integration scheme; (c) mesh from edge integration scheme

3.4 Closure

This chapter presented the concepts, theory and implementation of finite element error estimations, stress recovery and adaptive mesh generation. It was demonstrated through the validation examples that the developed methods performed as expected. Further applications of stress recovery technique can be found in Chapter 7.

4 DESIGN SENSITIVITY ANALYSIS

Sensitivity analysis of both the objective function and the constraints will first be presented in terms of the derivatives of the isoparametric transformation Jacobian matrix, the stiffness matrix and the force vector. A compact form of sensitivity formulae for the strength constraints is then presented based on either the maximum shear stress theory or the von Mises effective stress theory.

4.1 Introduction

The area for each individual element can be expressed in the isoparametric coordinates (ξ,η) as

$$A_e = \int_{\eta_0}^{\eta_1}\int_{\xi_0}^{\xi_1} \left|[J]_e\right| \, d\xi \, d\eta \tag{4.1}$$

where the integration limits are set such that

$$\begin{aligned} \xi_0 &= 0, \; \xi_1 = 1-\eta \\ \eta_0 &= 0, \; \eta_1 = +1 \end{aligned} \tag{4.2}$$

for the triangular element and

$$\begin{aligned} \xi_0 &= -1, \; \xi_1 = +1 \\ \eta_0 &= -1, \; \eta_1 = +1 \end{aligned} \tag{4.3}$$

for the quadrilateral element. The derivative of the area with respect to a design variable, p, can be expressed by

$$\frac{\partial A_e}{\partial p} = \int_{\eta_0}^{\eta_1}\int_{\xi_0}^{\xi_1} \frac{\partial \left| [J]_e \right|}{\partial p} \, d\xi \, d\eta \tag{4.4}$$

As a result, the sensitivity analysis for the total area (objective function) can be summed up from the contribution of each element to yield

$$\frac{\partial A}{\partial p} = \sum_e \frac{\partial A_e}{\partial p}$$

A group of constraint functions may be expressed by

$$g_i(\{u\},\{p\}) \le 0, \quad (1 \le i \le N_c)$$

It is noted that the displacements have been explicitly included as primary variables due to the fact that the displacement and strength constraints depend on these variables. In this way, less manipulation is required to conduct the sensitivity analysis. In fact, one of the primary goals in this analysis is to develop the expression for $\partial\{u\}/\partial p$. By using the chain rule of differentiation, the 1st order derivatives of a constraint function g_i can be expressed as

$$\frac{dg_i}{dp} = \frac{\partial g_i}{\partial p} + \{z^i\}^T \left\{ \frac{\partial u}{\partial p} \right\} \tag{4.5}$$

where $\{z^i\}$ is a vector with its components defined by

$$z_k^i = \frac{\partial g_i}{\partial u_k}, \quad (1 \le k \le M) \tag{4.6}$$

In general, it is relatively easy to calculate the first term on the right hand side of Equation (4.5). To compute the second term, two methods can be used. Both start from the following expression

$$\{z^i\}^T \frac{\partial\{u\}}{\partial p} = \{z^i\}^T [K]^{-1}\left(\frac{\partial\{f\}}{\partial p} - \frac{\partial[K]}{\partial p}\{u\}\right) \tag{4.7}$$

which can be obtained by first differentiating the FE equations (cf. Equation (A.1)), resulting in

$$[K]\frac{\partial\{u\}}{\partial p} = \frac{\partial\{f\}}{\partial p} - \frac{\partial[K]}{\partial p}\{u\} \tag{4.8}$$

and then premultiplying it by $\{z^i\}^T [K]^{-1}$.

The two methods differ in their numerical implementation. The first method, referred to as the direct method in the literature, consists of first solving Equation (4.8) directly for $\partial\{u\}/\partial p$ and then taking the inner product with the vector $\{z^i\}$. The second method, referred to as the adjoint variable method in the literature, begins by defining an adjoint variable vector $\{\lambda^i\}$ such that

$$[K]\{\lambda^i\} = \{z^i\}^T \tag{4.9}$$

and ends up with the calculation

$$\{z^i\}^T \frac{\partial\{u\}}{\partial p} = \{\lambda^i\}^T\left(\frac{\partial\{f\}}{\partial p} - \frac{\partial[K]}{\partial p}\{u\}\right) \tag{4.10}$$

where the fact that the stiffness matrix $[K]$ is symmetric is used.

Determining which of the above two methods should be employed is problem-dependent. Generally speaking, if the number of the design variables is less than that of the constraints, the direct method is recommended. Because relatively few design variables are used in this work, only the direct method will be considered in what follows.

In order to evaluate the displacement and constraint sensitivities, it is required to compute $\frac{\partial g_i}{\partial p}$ in Equation (4.5) and the right hand side of Equation (4.8). Again, there exist two approaches to fulfill the above calculations. For non-isoparametric elements, the finite difference technique is generally used, which is referred to as the semi-analytical method in the literature. One of the serious drawbacks associated with this method is that its accuracy depends heavily on the amount of perturbation in design variables. An alternative approach is to derive analytical expressions for these terms using isoparametric transformation properties. This latter method will be used exclusively in this work and its applications to a number of quantities are given in following sections.

4.2 Sensitivity Analysis Formulae

4.2.1 Calculation of $\frac{\partial |[J]_e|}{\partial p}$

As indicated before, the Jacobian $|[J]_e|$ can be expressed in terms of the nodal coordinates (x_i, y_i) and the derivatives of the shape functions in the isoparametric coordinates (ξ, η). By applying the chain rule, it can be seen that

$$\frac{\partial |[J]_e|}{\partial p} = \sum_{i=1}^{\tilde{N}} \left(\frac{\partial |[J]_e|}{\partial x_i} \frac{\partial x_i}{\partial p} + \frac{\partial |[J]_e|}{\partial y_i} \frac{\partial y_i}{\partial p} \right) \tag{4.11}$$

which can be computed by further noting that

$$\frac{\partial}{\partial x_i}\left(\frac{\partial x}{\partial \xi}\right)=\frac{\partial N_i}{\partial \xi}, \quad \frac{\partial}{\partial x_i}\left(\frac{\partial y}{\partial \xi}\right)=0$$
$$\frac{\partial}{\partial x_i}\left(\frac{\partial x}{\partial \eta}\right)=\frac{\partial N_i}{\partial \eta}, \quad \frac{\partial}{\partial x_i}\left(\frac{\partial y}{\partial \eta}\right)=0 \tag{4.12}$$

$$\frac{\partial}{\partial y_i}\left(\frac{\partial x}{\partial \xi}\right)=0, \quad \frac{\partial}{\partial y_i}\left(\frac{\partial y}{\partial \xi}\right)=\frac{\partial N_i}{\partial \xi}$$
$$\frac{\partial}{\partial y_i}\left(\frac{\partial x}{\partial \eta}\right)=0, \quad \frac{\partial}{\partial y_i}\left(\frac{\partial y}{\partial \eta}\right)=\frac{\partial N_i}{\partial \eta} \tag{4.13}$$

and

$$\frac{\partial\left|[J]_e\right|}{\partial x_i}=\frac{\partial N_i}{\partial \xi}\frac{\partial y}{\partial \eta}-\frac{\partial N_i}{\partial \eta}\frac{\partial y}{\partial \xi}$$
$$\frac{\partial\left|[J]_e\right|}{\partial y_i}=\frac{\partial N_i}{\partial \eta}\frac{\partial x}{\partial \xi}-\frac{\partial N_i}{\partial \xi}\frac{\partial x}{\partial \eta} \tag{4.14}$$

4.2.2 Calculation of $\frac{\partial[K]}{\partial p}\{u\}$

Various analytical expressions have been developed for the vector $\frac{\partial[K]}{\partial p}\{u\}$. The work by Wang *et al.* [79] seems to be the first one to develop analytical derivative expressions of the stiffness matrix and the force vector, although it is based on a specific type of isoparametric element. Brockman [19] formulated the vector for general isoparametric elements using tensor notation and differential geometry techniques. The equations used here are derived with direct manipulation and are easily used in calculations.

Consider the stiffness matrix of a single isoparametric element (cf. Appendix A) in its integration form of

$$[K]_e = h\int_{\eta_0}^{\eta_1}\int_{\xi_0}^{\xi_1}[B]^T[C][B]|[J]_e|\,d\xi\,d\eta \tag{4.15}$$

Its derivative with respect to the design variable p can be found as

$$\frac{\partial[K]_e}{\partial p}\{u\}_e = h\int_{\eta_0}^{\eta_1}\int_{\xi_0}^{\xi_1}\left\{\left[\frac{\partial[B]^T}{\partial p}[C][B]+[B]^T\frac{\partial[C]}{\partial p}[B]\right]|[J]_e|+\frac{\partial|[J]_e|}{\partial p}[B]^T[C][B]\right\}\{u\}_e\,d\xi\,d\eta \tag{4.16}$$

where $\{u\}_e$ represents the local displacement vector. To numerically evaluate the above vector, we need only to demonstrate how to calculate the matrix $\dfrac{\partial[B]^T}{\partial p}$. This can be done by noting that the matrix $[B]$ is composed of the terms $N_{i,x}$ and $N_{i,y}$ with the following derivative expressions

$$\frac{\partial}{\partial p}\begin{Bmatrix}N_{i,x}\\N_{i,y}\end{Bmatrix} = -[J]^{-1}\frac{\partial[J]}{\partial p}\begin{Bmatrix}N_{i,x}\\N_{i,y}\end{Bmatrix} \tag{4.17}$$

and

$$\frac{\partial[J]}{\partial p}=\begin{bmatrix} N_{1,\xi} & N_{2,\xi} & \cdots & N_{\tilde{N},\xi} \\ N_{1,\eta} & N_{2,\eta} & \cdots & N_{\tilde{N},\eta} \end{bmatrix}\frac{\partial}{\partial p}\begin{bmatrix} x_1 & y_1 \\ x_2 & y_2 \\ \vdots & \vdots \\ x_{\tilde{N}} & y_{\tilde{N}} \end{bmatrix} \tag{4.18}$$

4.2.3 Calculation of $\frac{\partial\{f\}}{\partial p}$

By assuming that the intensity of the distributed loads is invariant to the perturbed structural boundary shape, it can be found that

$$\begin{aligned} \frac{\partial f_{x,i}}{\partial p} &= h\int_{-1}^{+1} p_x N_i(\xi)\frac{\partial\left|[J]_s\right|}{\partial p}d\xi \\ \frac{\partial f_{y,i}}{\partial p} &= h\int_{-1}^{+1} p_y N_i(\xi)\frac{\partial\left|[J]_s\right|}{\partial p}d\xi \end{aligned} \tag{4.19}$$

It should be further noted that from Equation (A.14)

$$\frac{\partial\left|[J]_s\right|}{\partial p}=\sum_{i=1}^{\tilde{N}_b}\left(\frac{\partial\left|[J]_s\right|}{\partial x_i}\frac{\partial x_i}{\partial p}+\frac{\partial\left|[J]_s\right|}{\partial y_i}\frac{\partial y_i}{\partial p}\right) \tag{4.20}$$

and

$$\begin{aligned} \frac{\partial\left|[J]_s\right|}{\partial x_i} &= \frac{N_{i,x}}{\left|[J]_s\right|}\frac{dx(\xi)}{dp} \\ \frac{\partial\left|[J]_s\right|}{\partial y_i} &= \frac{N_{i,x}}{\left|[J]_s\right|}\frac{dy(\xi)}{dp} \end{aligned} \tag{4.21}$$

with

$$\frac{dx(\xi)}{dp} = \sum_{j=1}^{\tilde{N}_b} N_{j,\xi}\, x_j$$
$$\frac{dy(\xi)}{dp} = \sum_{j=1}^{\tilde{N}_b} N_{j,\xi}\, y_j \tag{4.22}$$

4.2.4 Strength Sensitivity Analysis

Compact design sensitivity formulae of the strength constraints, based on either the maximum shear stress theory or the von Mises effective stress theory, are developed here. In matrix notation, these two criteria, for a planar structural problem, can be represented by

$$\sigma_{\chi}^{2} = \{\sigma\}^{T} [V_{\chi}] \{\sigma\} \tag{4.23}$$

where the subscript can be taken as S or V to represent the maximum shear stress or the von Mises stress, respectively. The corresponding matrices are expressed as

$$[V_S] = \begin{bmatrix} \frac{1}{4} & -\frac{1}{4} & 0 \\ -\frac{1}{4} & \frac{1}{4} & 0 \\ 0 & 0 & 1 \end{bmatrix}$$
$$[V_S] = \begin{bmatrix} 1 & -\frac{1}{2} & 0 \\ -\frac{1}{2} & 1 & 0 \\ 0 & 0 & 3 \end{bmatrix} \tag{4.24}$$

The strength constraint is expressed by

$$g = \frac{\sigma_\chi^2}{\sigma_A^2} - 1 \tag{4.25}$$

where σ_A^2 is the square of the prescribed failure strength values, which in general can be either one of σ_C^2, σ_T^2 or $\sigma_C \sigma_T$ (σ_C and σ_T denote the allowable stresses for compressive and tensile failures, respectively.) It can be shown for a pointwise strength constraint that

$$\frac{dg}{dp} = \frac{2}{\sigma_A^2} \{\sigma\}^T [V_\chi][D] \left([B] \frac{\partial \{u\}}{\partial p} + \frac{\partial B}{\partial p} \{u\} \right) \tag{4.26}$$

Similar sensitivity results are also developed for the constraint in the integral form. Note that the constraint in the area integral form is defined for each element by

$$\bar{g} = \frac{1}{A_e} \int_{A_e} g \, dA = \frac{1}{A_e} \int\int \frac{\sigma_\chi^2}{\sigma_A^2} |[J]| \, d\xi \, d\eta - 1 \tag{4.27}$$

The sensitivity of this constraint form with respect to a design variable p can be found as

$$\frac{d\bar{g}}{dp} = \frac{1}{A_e} \int_{\eta_1}^{\xi_1} \int_{\eta_2}^{\xi_2} \frac{dg}{dp} |[J]| \, d\xi \, d\eta - \frac{1}{A_e} \int_{\eta_1}^{\xi_1} \int_{\eta_2}^{\xi_2} \frac{d|[J]|}{dp} d\xi \, d\eta \int_{\eta_1}^{\xi_1} \int_{\eta_2}^{\xi_2} g |[J]| \, d\xi \, d\eta \tag{4.28}$$

or simply

$$\frac{d\bar{g}}{dp} = \frac{1}{A_e}\left[\int_{A_e}\frac{dg}{dp}\,dA - \bar{g}\int_{\eta_1\eta_2}^{\xi_1\xi_2}\int\frac{d|[J]|}{dp}\,d\xi\,d\eta\right] \tag{4.29}$$

which is implemented in our package as a default option.

4.3 Implementation Notes

It is felt necessary to include a few supplementary notes that have been found to be helpful in actual implementation of the foregoing formulae.

It is first noted that the solution of Equation (4.8) requires the inverse of the stiffness matrix $[K]$, the reduced form (i.e., the matrix after adding the essential boundary conditions) of which is available in the factorized banded form used to solve for the displacement from Equation (A.1). To take advantage of this in computing $\frac{\partial\{u\}}{\partial p}$, it is important to note that this vector must have the same restrictions as those used in the solution of the displacement vector imposed by the boundary conditions.

It was found that by multiplying some objective function sensitivities by a value of greater than unity during the early stage of optimization iterations helps to accelerate the convergence of the whole optimization process. This can be explained by Figure 4.1. Moving of an interior design point D to D' causes a larger area change than moving a boundary design point A to A'. Before any constraint is reached, it is more likely for point D to move faster than point A. As a result of a large area sensitivity value at design point A, the movement of this can be speeded up.

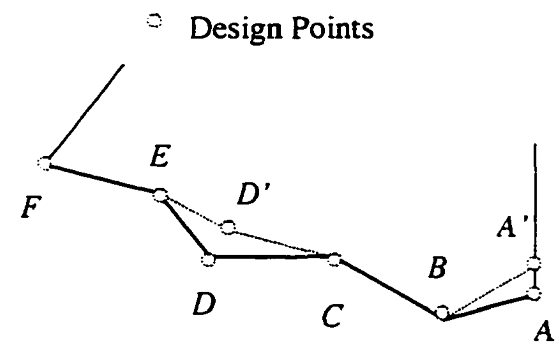

Figure 4.1: Illustration of objective function sensitivity by moving design points.

5 DUAL KRIGING B-SPLINE FITTING

5.1 Background

With the rise of relatively inexpensive computing, great strides have been made in curve and surface fitting and interpolation. The need to fit curves and surfaces arises primarily from the fact that, although most physical phenomena are continuous, their measurement is made by discretization. From such discrete information, it is often desired to reconstruct the continuum features in detail using numerical fitting tools. Traditionally, the regression technique has been the primary tool used for such a purpose. Its major drawback is that such a reconstructed curve or surface may not pass through the available data points. An alternative is to use a pure interpolation technique. The interpolated results, however, usually contain undesirable oscillations. In this work, the dual kriging technique is used to recover parametric three-dimensional curves and surfaces by using a limited number of available data. An important feature of the dual kriging method is that the continuous, fitted curves and surfaces are constrained to pass through each and every discretized data point. Briefly, the dual kriging approach is to represent a curve or surface by the sum of draft and covariance functions. While an open-type cubic B-spline function is used for the draft, attention will be paid here to the effects on the resulting curve and surface interpolations of using different functions to model the covariance part. It will be shown that proper selection of a covariance function can enhance certain desirable properties in the recovered shapes.

A brief summary of the dual kriging technique is given first. This will be followed by the theoretical formulation of the parametric curve and surface. Three parametrization schemes, uniform, chord-length and surface-area based, are emphasized. A new scheme, referred to as a quasi-uniform parametrization, is proposed for surface fitting based on computational efficiency considerations. Finally, some results of applying the dual kriging scheme to curve and surface interpolations are given. In these examples, the issue of selecting a suitable covariance function is addressed.

5.2 Theoretical Development

We start with the development of the dual kriging interpolation technique for a 3-D curve. The B-spline function is introduced along with a brief discussion of the selection of its knot vector and parametrization. This is followed by the formulation of the dual kriging interpolation algorithm by adding a covariance function part to the B-spline curve-fitting scheme. With these preliminaries completed, surface interpolation is investigated via the dual kriging scheme. As will be pointed out, significant improvements in computational efficiency are achieved if certain parametrization procedures are used.

5.2.1 Curve Interpolation

A three-dimensional curve can be defined parametrically by

$$P(t) = \left[x(t), y(t), z(t)\right] \tag{5.1}$$

where t is referred to as the parameter restricted in the interval [0,1]. To introduce the dual kriging technique, we approximate the curve defined above with a combination of two parametric curves

$$P(t) = P_d(t) + P_c(t) \tag{5.2}$$

where the first part, $P_d(t)$, referred to as the draft, can be any traditional interpolating function, and $P_c(t)$ is the generalized covariance function (or simply the covariance function). A brief account of issues involved in the selection of covariance functions will be given below.

In this work, B-spline functions are selected exclusively for the draft part. That is, $P_d(t)$ can be written as

$$P_d(t) = \sum_{i=1}^{M} B_i N_{i,K}(t) \tag{5.3}$$

where M points B_i $(1 \le i \le M)$ are referred to as the control polygon points on which the B-spline fitting technique is based, and $N_{i,K}$ $(1 \le i \le M)$ are called the normalized K-th order B-spline basis functions, which are defined by the Cox-deBoor recursion relationship

$$\begin{aligned} N_{i,1}(t) &= \begin{cases} 1 & , \quad x_i \le t \le x_{i+1} \\ 0 & , \quad \text{otherwise} \end{cases} \\ N_{i,K}(t) &= \frac{(t - x_i)N_{i,K-1}(t)}{x_{i+K-1} - x_i} - \frac{(t - x_{i+K})N_{i,K-1}(t)}{x_{i+K} - x_{i+1}}, \text{if } K \ge 2 \end{aligned} \tag{5.4}$$

The values of x_i form a knot vector [X] and it is assumed that $x_i < x_{i+1}$. The entities in the knot vector may be specified in different ways. However, the open uniform knot vector is used exclusively in this study. As a consequence, this knot vector [X] can be expressed by

$$x_i = \begin{cases} 0 & , \quad 1 \le i \le K-1 \\ \dfrac{i-K+1}{M-K+1} & , \quad K \le i \le M-K+1 \\ 1 & , \quad M-K+2 \le i \le M \end{cases} \tag{5.5}$$

For N available data points, a set of parametric values corresponding to these data points $\{P_i\}_{i=1}^{N}$ can be formed according to the chord length

$$[T] = [t_1 \, t_2 \cdots t_N] \tag{5.6}$$

such that

$$\begin{cases} t_1 = 0 \\ t_j = \dfrac{D_{j-1,j}}{D}, \quad (2 \le j \le N-1) \\ t_N = 1 \end{cases} \tag{5.7}$$

where $D_{j-1,j}$ is the chord distance between the data points P_{j-1} and P_j and $D = \sum_{j=2}^{M} D_{j-1,j}$.

Chord length parametrization is a convenient method for evaluating B-spline functions because it is independent of the coordinate system employed and can be generally regarded as a sufficient approximation to the arc length of the curve. An alternative parametrization is to set parametric values uniformly such as

$$t_j = \frac{j-1}{N-1}, \; (1 \le j \le N) \tag{5.8}$$

It will be shown later that selecting a different parametrization for a curve rarely affects the computational efficiency of the whole procedure. However, this conclusion cannot be extended to surface fitting, as will be discussed below.

Now suppose that we want to approximate a body of N data by constructing a continuous curve $P(t)$ passing through each of the given data points and the integer M in Equation (5.3) is less than or equal to N. This can be established by imposing an additionally restricted condition in Equation (5.3). In the dual kriging method, the covariance part is generally assumed to be of the form

$$P_c(t) = \sum_{j=1}^{N} C_j K(h_j) \tag{5.9}$$

where $h_j = |t - t_j|$ and $t_j \; (1 \le j \le N)$ denote N parametric values. $K(h)$ represents a covariance function. The most widely used covariances in the dual kriging method will be discussed in the following section (see Table 5.1). With Equations (5.3) and (5.9), we have a total of $N+M$ unknowns (B_i, C_j). It is noted that the N data points give us only N equations

$$P(t_k) = \sum_{i=1}^{M} B_i \, N_{i,K}(t_k) + \sum_{j=1}^{N} C_j \, K(h_{k,j}) \qquad (1 \le k \le N) \tag{5.10}$$

where $h_{k,j} = \left|t_k - t_j\right|$. The remaining M equations come from the dual equations

$$\sum_{k=1}^{N} C_j N_{i,K}(t_j) = 0, \ (1 \le i \le M) \tag{5.11}$$

Combining Equations (5.10) and (5.11) yields the equations in the matrix form

$$\begin{bmatrix} [K] & [A] \\ [A]^T & [0] \end{bmatrix} \begin{bmatrix} [C] \\ [B] \end{bmatrix} = \begin{bmatrix} [P] \\ [0] \end{bmatrix} \tag{5.12}$$

where

$$[K] = \begin{bmatrix} K(0) & K(h_{1,2}) & \cdots & K(h_{1,N}) \\ K(h_{2,1}) & K(0) & \cdots & K(h_{2,N}) \\ \vdots & \vdots & \ddots & \vdots \\ K(h_{N,1}) & K(h_{N,2}) & \cdots & K(0) \end{bmatrix} \tag{5.13}$$

$$[A] = \begin{bmatrix} N_{1,K}(t_1) & N_{2,K}(t_1) & \cdots & N_{M,K}(t_1) \\ N_{1,K}(t_2) & N_{2,K}(t_2) & \cdots & N_{M,K}(t_2) \\ \vdots & \vdots & \ddots & \vdots \\ N_{1,K}(t_N) & N_{2,K}(t_N) & \cdots & N_{M,K}(t_N) \end{bmatrix} \tag{5.14}$$

and

$$[C] = \begin{bmatrix} C_1 \\ C_2 \\ \vdots \\ C_N \end{bmatrix} \quad [B] = \begin{bmatrix} B_1 \\ B_2 \\ \vdots \\ B_M \end{bmatrix}, \quad [P] = \begin{bmatrix} P_1 \\ P_2 \\ \vdots \\ P_N \end{bmatrix} \tag{5.15}$$

where $P_k = P(t_k), (1 \le k \le N)$. Thus, the N+M coefficients B_i and C_j can be determined if the coefficient matrix in Equation (5.12) is regular. The required regularity of this matrix can be shown if the matrix $[K]$ is regular and $[A]$ is a full-column rank matrix (i.e. $\text{rank}([A]) = M$, which is also an important condition in using the least squares B-spline fitting) due to the following identity

$$\begin{bmatrix} [I] & [0] \\ -[A]^T[K]^{-1} & [I] \end{bmatrix} \begin{bmatrix} [K] & [A] \\ [A]^T & [0] \end{bmatrix} = \begin{bmatrix} [K] & [A] \\ [0] & -[A]^T[K]^{-1}[A] \end{bmatrix} \tag{5.16}$$

where $[I]$ denotes a unit matrix. The traditional least squares B-spline fitting can be derived as a special example by identifying $[K]$=$[I]$ and $[C]$=$[0]$. In fact, it can be shown that with $[K]$=$[I]$

$$\begin{aligned} [B] &= \left([A]^T[A]\right)^{-1}[A]^T\,[P] \\ [C] &= \left([I]-[A]\left([A]^T[A]\right)^{-1}[A]^T\right)[P] \end{aligned} \tag{5.17}$$

It should be mentioned that with the calculated polygon points B_i, a new knot vector may be constructed that depends on the chord length formed from these polygon points, also referred to as the nonuniform B-spline method [63]. Two reasons motivated consideration of only a uniform knot vector: exact interpolation of the available data points is our primary requirement; and, our calculations show very little difference between the results computed by uniform and nonuniform B-splines.

5.2.2 Surface Interpolation

The next topic to be discussed is the dual kriging surface fitting. A surface can be described by a set of two-parameter equations

$$
\begin{aligned}
x &= P_x(u,v) \\
y &= P_y(u,v) \\
z &= P_z(u,v)
\end{aligned}
\tag{5.18}
$$

where, as usual, x, y and z are the three coordinates in the Cartesian system. For simplicity, and with no loss of generality, we will deal with one of the three components in the above equations. This component can be denoted by

$$P(u,v) = P_v(u) = P_u(v) \tag{5.19}$$

where the range of each of the parametric values u and v is restricted to a unit interval $[0,1]$. It is noted that the last two equalities in Equation (5.19) represent two different interpretations of a parametric surface. $P_v(u)$ represents a curve which is created from a one-parameter u equation with fixed v and similar explanation is applied to $P_u(v)$.

Let $\{P_{n,m}\}$ $(1 \le n \le N_u, 1 \le m \le N_v)$ be $N_u \times N_v$ data points. It is emphasized that the chord-distance parametric values from the discrete curve data with a fixed index m, for example m_1, may not be identical to the parametric values with a different index m. As a result, the notations u_n^v and ${}^u v_m$ will be used to indicate the parametric values in the u direction with fixed v and in the v direction with fixed u, respectively.

Similar to Equation (5.2), two one-parameter curve equations can be described by

$$P_v(u) = \sum_{i=1}^{M_u} B_{i,v}^{(1)} N_{i,K_u}^{(1)}(u) + \sum_{j=1}^{N_u} C_{j,v}^{(1)} K^{(1)}\left(h_j^v\right) \tag{5.20}$$

and

$$P_u(v) = \sum_{i=1}^{M_v} B_{u,i}^{(2)} N_{i,K_v}^{(2)}(v) + \sum_{j=1}^{N_v} C_{u,j}^{(2)} K^{(2)}\left({}^u h_j\right) \tag{5.21}$$

where $h_j^v = \left|u - u_j^v\right|$ and ${}^v h_j = \left|v - {}^u v_j\right|$. The forms of the covariance functions $K^{(1)}(h)$ and $K^{(2)}(h)$, as well as the orders of the B-spline basis functions $N_{i,K_u}^{(1)}(u)$ and $N_{i,K_v}^{(2)}(v)$, are independent of parameters v and u, respectively.

For a fixed value $v = v_m$, Equation (5.20) reduces to

$$P_{v_m}(u) = \sum_{i=1}^{M_u} B_{i,m}^{(1)} N_{i,K_u}^{(1)}(u) + \sum_{j=1}^{N_u} C_{j,m}^{(1)} K^{(1)}\left(h_j^m\right) \tag{5.22}$$

where $h_j^m = \left|u - u_j^m\right|$. The dual kriging fitting with N_u available data points can be expressed, similar to Equation (5.12), as

$$\begin{bmatrix} \left[K_m^{(1)}\right] & \left[A_m^{(1)}\right] \\ \left[A_m^{(1)}\right]^T & [0] \end{bmatrix} \begin{bmatrix} \left[C_m^{(1)}\right] \\ \left[B_m^{(1)}\right] \end{bmatrix} = \begin{bmatrix} \left[P_m^{(1)}\right] \\ [0] \end{bmatrix} \tag{5.23}$$

where

$$\left[K_m^{(1)}\right] = \begin{bmatrix} K^{(1)}(0) & K^{(1)}\left(h_{1,2}^m\right) & \cdots & K^{(1)}\left(h_{1,N_u}^m\right) \\ K^{(1)}\left(h_{2,1}^m\right) & K^{(1)}(0) & \cdots & K^{(1)}\left(h_{2,N_u}^m\right) \\ \vdots & \vdots & \ddots & \vdots \\ K^{(1)}\left(h_{N_u,1}^m\right) & K^{(1)}\left(h_{N_u,2}^m\right) & \cdots & K^{(1)}(0) \end{bmatrix} \tag{5.24}$$

$$\left[A_m^{(1)}\right]=\begin{bmatrix} N_{1,K_u}^{(1)}\left(u_1^m\right) & N_{2,K_u}^{(1)}\left(u_1^m\right) & \cdots & N_{M_u,K_u}^{(1)}\left(u_1^m\right) \\ N_{1,K_u}^{(1)}\left(u_2^m\right) & N_{2,K_u}^{(1)}\left(u_2^m\right) & \cdots & N_{M_u,K_u}^{(1)}\left(u_2^m\right) \\ \vdots & \vdots & \ddots & \vdots \\ N_{1,K_u}^{(1)}\left(u_{N_u}^m\right) & N_{2,K_u}^{(1)}\left(u_{N_u}^m\right) & \cdots & N_{M_u,K_u}^{(1)}\left(u_{N_u}^m\right) \end{bmatrix} \tag{5.25}$$

and

$$\left[C_m^{(1)}\right]=\begin{bmatrix} C_{1,m}^{(1)} \\ C_{2,m}^{(1)} \\ \vdots \\ C_{N_u,m}^{(1)} \end{bmatrix} \quad \left[B_m^{(1)}\right]=\begin{bmatrix} B_{1,m}^{(1)} \\ B_{2,m}^{(1)} \\ \vdots \\ B_{M_u,m}^{(1)} \end{bmatrix}, \quad \left[P_m^{(1)}\right]=\begin{bmatrix} P_{1,m} \\ P_{2,m} \\ \vdots \\ P_{N_u,m} \end{bmatrix} \tag{5.26}$$

where $h_{k,j}^m = \left|u_k^m - u_j^m\right|$, $\left(1 \le k, j \le N_u\right)$. Similarly, for a fixed value u, the dual kriging equations passing through N_v data points can be developed from Equation (5.21) as

$$\begin{bmatrix} \left[K_u^{(2)}\right] & \left[A_u^{(2)}\right] \\ \left[A_u^{(2)}\right]^T & [0] \end{bmatrix} \begin{bmatrix} \left[C_u^{(2)}\right] \\ \left[B_u^{(2)}\right] \end{bmatrix} = \begin{bmatrix} \left[P_u^{(2)}\right] \\ [0] \end{bmatrix} \tag{5.27}$$

where

$$\left[K_u^{(2)}\right]=\begin{bmatrix} K^{(2)}(0) & K^{(2)}\left({}^u h_{1,2}\right) & \cdots & K^{(2)}\left({}^u h_{1,N_v}\right) \\ K^{(2)}\left({}^u h_{2,1}\right) & K^{(2)}(0) & \cdots & K^{(2)}\left({}^u h_{2,N_v}\right) \\ \vdots & \vdots & \ddots & \vdots \\ K^{(2)}\left({}^u h_{N_v,1}\right) & K^{(2)}\left({}^u h_{N_v,2}\right) & \cdots & K^{(2)}(0) \end{bmatrix} \tag{5.28}$$

$$\left[A_u^{(2)}\right]=\begin{bmatrix} N_{1,K_u}^{(2)}\left({}^u v_1\right) & N_{2,K_v}^{(1)}\left({}^u v_1\right) & \cdots & N_{M_v,K_v}^{(1)}\left({}^u v_1\right) \\ N_{1,K_v}^{(2)}\left({}^u v_2\right) & N_{2,K_v}^{(1)}\left({}^u v_2\right) & \cdots & N_{M_v,K_v}^{(1)}\left({}^u v_2\right) \\ \vdots & \vdots & \ddots & \vdots \\ N_{1,K_v}^{(1)}\left({}^u v_{N_v}\right) & N_{2,K_v}^{(1)}\left({}^u v_{N_v}\right) & \cdots & N_{M_v,K_v}^{(1)}\left({}^u v_{N_v}\right) \end{bmatrix} \tag{5.29}$$

and

$$\left[C_u^{(2)}\right]=\begin{bmatrix} C_{n,1}^{(2)} \\ C_{n,2}^{(2)} \\ \vdots \\ C_{n,N_v}^{(2)} \end{bmatrix} \quad \left[B_u^{(2)}\right]=\begin{bmatrix} B_{n,1}^{(2)} \\ B_{n,2}^{(2)} \\ \vdots \\ B_{n,M_v}^{(2)} \end{bmatrix}, \quad \left[P_u^{(2)}\right]=\begin{bmatrix} P(u,v_1) \\ P(u,v_2) \\ \vdots \\ P\left(u,v_{N_v}\right) \end{bmatrix} \tag{5.30}$$

where ${}^u h_{k,j}=\left|{}^u v_k-{}^u v_j\right|, \left(1\le k,j\le N_v\right)$. It is noted that

$$P_u(v)=\left[F_u^{(2)}\right]\left[Q_u^{(2)}\right]^{-1}\begin{bmatrix}\left[P_u^{(2)}\right] \\ \\ [0]\end{bmatrix} \tag{5.31}$$

where

$$\left[Q_u^{(2)}\right]=\begin{bmatrix}\left[K_u^{(2)}\right] & \left[A_u^{(2)}\right] \\ \\ \left[A_u^{(2)}\right]^T & [0]\end{bmatrix} \tag{5.32}$$

and

$$\left\lfloor F_u^{(2)}\right\rfloor=\left\lfloor K^{(2)}\left({}^u h_1\right) \;\cdots\; K^{(2)}\left({}^u h_{N_v}\right) \;\; N_{1,K_v}^{(2)}(v) \;\cdots\; N_{M_v,K_v}^{(2)}(v)\right\rfloor \tag{5.33}$$

where ${}^u h_j=\left|v-{}^u v_j\right|, \left(1\le j\le N_v\right)$.

To develop an expression for $\left[P_u^{(2)}\right]$, we note that $P(u, v_m) = P_{v_m}(u)$ and

$$P_{v_m}(u) = \left[F_m^{(1)}\right]\left[Q_m^{(1)}\right]^{-1}\begin{bmatrix}\left[P_m^{(1)}\right] \\ [0]\end{bmatrix} \tag{5.34}$$

where

$$\left[Q_m^{(1)}\right] = \begin{bmatrix}\left[K_m^{(1)}\right] & \left[A_m^{(1)}\right] \\ \left[A_m^{(1)}\right]^T & [0]\end{bmatrix} \tag{5.35}$$

and

$$\left[F_m^{(1)}\right] = \left[K^{(1)}\left(h_1^m\right) \quad \cdots \quad K^{(1)}\left(h_{N_u}^m\right) \quad N_{1,K_u}^{(1)}(u) \quad \cdots \quad N_{M_u,K_u}^{(1)}(u)\right] \tag{5.36}$$

where $h_j^m = \left|u - u_j^m\right|, \left(1 \le j \le N_u\right)$. Some simplifications can be made by considering the x, y and z coordinates of each data point. For the sake of presentation, the same notation as above is retained, but note that the formulation should be applied to each coordinate separately. Consequently, the scalar expression given by Equation (5.34) can be recast as

$$P_{v_m}(u) = \left[\left[P_m^{(1)}\right]^T \quad [0]\right]\left[Q_m^{(1)}\right]^{-T}\left[F_m^{(1)}\right]^T \tag{5.37}$$

and by reference to Equation (5.30), we find

$$\left[P_u^{(2)}\right]=\begin{bmatrix} \left[\left[P_1^{(1)}\right]^T \quad [0]\right]\left[Q_1^{(1)}\right]^{-T}\left[F_1^{(1)}\right]^T \\ \left[\left[P_2^{(1)}\right]^T \quad [0]\right]\left[Q_2^{(1)}\right]^{-T}\left[F_2^{(1)}\right]^T \\ \vdots \\ \left[\left[P_{N_u}^{(1)}\right]^T \quad [0]\right]\left[Q_{N_u}^{(1)}\right]^{-T}\left[F_{N_u}^{(1)}\right]^T \end{bmatrix} \tag{5.38}$$

The foregoing discussions can be simplified when the quasi-uniform parametrization is used for both u and v variables. That is, a parametrization of u at a specific v value is used for all other v values, and a similar technique is applied to the parametrization of v. For this special case, it is noted that $\lfloor Q_m^{(1)} \rfloor$ and $\lfloor F_m^{(1)} \rfloor$ are independent of m $(1 \le m \le N_v)$ and therefore will be denoted by $\lfloor Q^{(1)} \rfloor$ and $\lfloor F^{(1)} \rfloor$, respectively. Similarly, $\lfloor Q_u^{(2)} \rfloor$ and $\lfloor F_u^{(2)} \rfloor$ can be denoted by $\lfloor Q^{(2)} \rfloor$ and $\lfloor F^{(2)} \rfloor$. Furthermore, the two matrices $\lfloor Q^{(1)} \rfloor$ and $\lfloor Q^{(2)} \rfloor$ are constant matrices, while $\lfloor F^{(1)} \rfloor$ and $\lfloor F^{(2)} \rfloor$ are functions of only u and v, respectively, and will be denoted by $\lfloor F^{(1)}(u) \rfloor$ and $\lfloor F^{(2)}(v) \rfloor$ for clarity. Equation (5.38) can now be reduced to

$$\left[P_u^{(2)}\right]=\begin{bmatrix} \left[\left[P_1^{(1)}\right]^T \quad [0]\right]\left[Q_1^{(1)}\right]^{-T}\left[F_1^{(1)}\right]^T \\ \left[\left[P_2^{(1)}\right]^T \quad [0]\right]\left[Q_2^{(1)}\right]^{-T}\left[F_2^{(1)}\right]^T \\ \vdots \\ \left[\left[P_{N_u}^{(1)}\right]^T \quad [0]\right]\left[Q_{N_u}^{(1)}\right]^{-T}\left[F_{N_u}^{(1)}\right]^T \end{bmatrix} \tag{5.39}$$

Substituting Equation (5.39) into Equation (5.31) yields

$$P(u,v)=P_u(v)=\left[F^{(2)}(v)\right]\left[Q^{(2)}\right]^{-1}\left[\hat{P}\right]\left[Q^{(1)}\right]^{-T}\left[F^{(1)}(u)\right]^{T} \tag{5.40}$$

where

$$\left[\hat{P}\right]=\begin{bmatrix} \begin{bmatrix} P_{1,1} & P_{2,1} & \cdots & P_{N_u,1} \\ P_{1,2} & P_{2,2} & \cdots & P_{N_u,2} \\ \vdots & \vdots & \ddots & \vdots \\ P_{1,N_v} & P_{2,N_v} & \cdots & P_{N_u,N_v} \end{bmatrix} & [0] \\ [0] & [0] \end{bmatrix} \tag{5.41}$$

Once the matrix

$$\left[Q^{(2)}\right]^{T}\left[\hat{P}\right]\left[Q^{(1)}\right]^{-T} \tag{5.42}$$

is computed, a point on the surface characterized by parameters (u,v) can be calculated easily and efficiently by Equation (5.40).

In applying the quasi-uniform parameterization, one may intuitively choose specific u- and v-indices from the available data to develop chord-length parametrization. The choice of proper indices may not be obvious for some applications. As a compromise, uniform parameterization in the u- and v-directions may be used. Various parametrization procedures related to surface fitting have been reviewed by Theodoracatos and Bobba [69]. Based on that investigation and comparison, they proposed a surface-area based parametrization method. This method makes use of the area information associated with a patch formed by data points. A very brief account of this parametrization procedure is given in Appendix B.

5.3 Covariance Functions

Careful selection of the covariance function in the dual kriging method is important because the model chosen is used throughout the process and may influence all results and conclusions. It was mentioned [28] that the most widely used models in the geostatistical community are polynomials with odd order up to five. Matheron [52] proposed another model, $K(h) = h^2 \ln(h)$, which was not based on a rigorous geostatistical analysis. (Dubrule referred to it as spline covariance [29].) In this work, attention is focused on the first three covariance functions listed in Table 5.1; their graphic representations are shown in Figure 5.1.

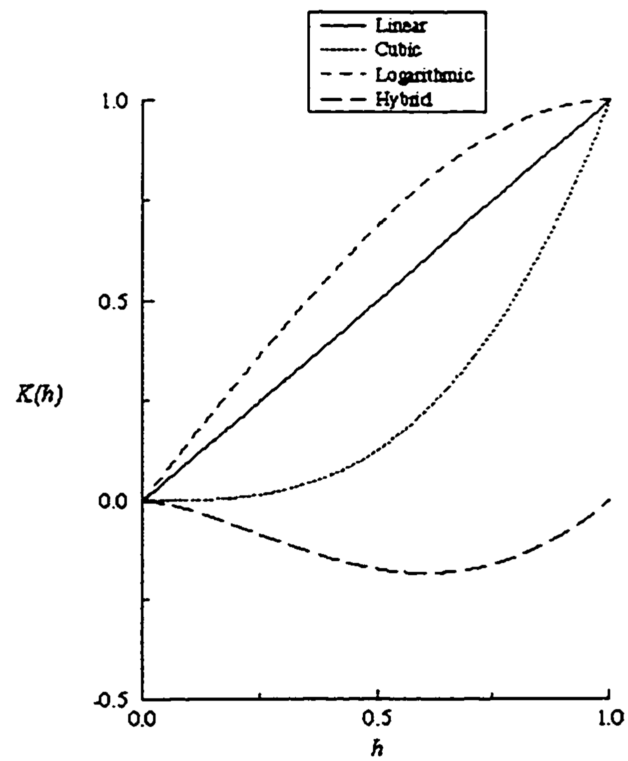

Figure 5.1: Graphic representation of covariance functions

These functions were also used by Gilbert, et al. [32] and Limaiem and El Marghy [50]. It has been observed that the results obtained with the hybrid covariance function are almost identical to those found using the linear covariance function. Consequently, the hybrid covariance function will not be used in what follows. It is noted that a "nugget effect" (i.e., a constant term in the covariance function) is not included here based on the assumption that the data are given without error. As will be demonstrated by the following examples, among the covariance models in Table 5.1, the linear function performs best for data characterized by a low degree of continuity, because it reaches both ends in a nonsmooth fashion. As a result, it is expected that the use of this model will yield a good approximation to a curve with a low degree of continuity. The examples shown later will support this assertion.

Table 5.1: Covariance functions

Functions	$K(h)$
Linear	h
Cubic	h^3
Logarithmic	$\begin{cases} 0 & h=0 \\ h^2\ln(h) & \text{otherwise} \end{cases}$
Hybrid	$\frac{1}{2}\left(3h-h^3\right)$

5.4 Applications and Discussion

The cubic B-spline function is used exclusively as the draft function in the examples considered below. All graphic presentations shown here are generated by dividing each interval of parametric values into a number of subintervals. As a result, the generated curves and surfaces pass through every data point, except for discrepancies due to round-off errors introduced in the computations. Note also that selecting the number of control polygon points is important in that the desired curve or surface is generally better approximated using a large number of control polygon points, while using an excessive number of control polygon points may result in a considerable increase in computational time and severe oscillation in the approximation. Thus, the selection of the number of control polygon points in this work is a compromise made for each case.

It is known that the Gaussian and mean curvatures can be used as tools to characterize a number of important properties associated with a fitted surface. For example, the algebraic sign of a Gaussian curvature value indicates the classification of the surface. In general, one of the many criteria used to evaluate competing surface fitting methods is that smaller variations of the curvature should be observed in smooth areas, while larger variations are expected in nonsmooth areas. Because the dual kriging approximation in general does not result in an expression which can be differentiated analytically (unlike the B-spline approximation, which can be differentiated), it is necessary to resort to numerical procedures to compute the Gaussian and mean curvatures. It is important to note that forcing the curve or the surface to pass through the data points disrupts the local smoothness of the recovered functions. As a result, the smoothness of the fitted surface tends to become worse as the density of the data points increases. This phenomenon becomes more pronounced near the boundaries because the draft function consists of the open type B-spline functions. On the other hand, this nonsmooth tendency may become beneficial in recovering some surfaces. In this work, second-order-accurate finite-difference approximations will be used to differentiate the kriging functions. The associated formulae can be found in Appendix B.

5.4.1 Curve Interpolation

To investigate the effects of different covariance functions and parametrization schemes on dual kriging interpolation, a two-dimensional curve is considered first. The data are generated by a hybrid function commonly used in computational fluid dynamics community to validate the shock capturing schemes because of its complex shape [67]. The analytical function is given by

$$y(x) = \begin{cases} |\sin(2\pi x)|, & |x| \le \dfrac{1}{3} \\ 2x - 1 - \dfrac{\sin(3\pi x)}{6}, & \dfrac{1}{3} < x < 1 \end{cases} \tag{5.43}$$

The data set consists of 21 points on the analytical curve, as shown by solid points in Figure 5.2. The fitting and interpolating results are shown in Figure 5.3 through Figure 5.6 for the uniform (dotted lines) and the chord-length (dashed lines) parameterization. Seven control polygon points are used in computing these results.

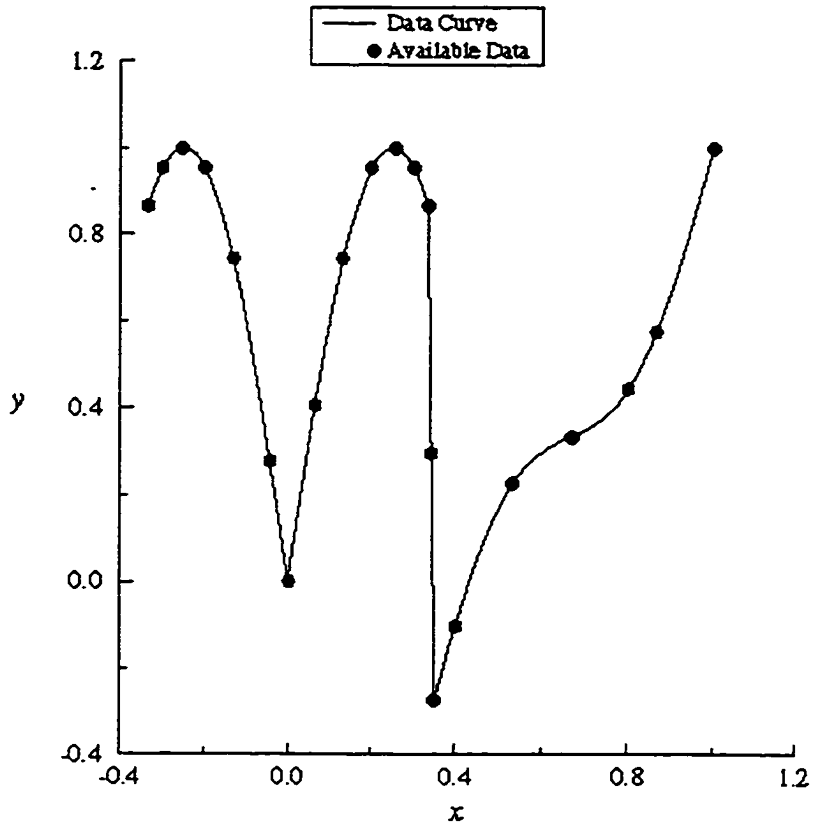

Figure 5.2: Available data points of the curve

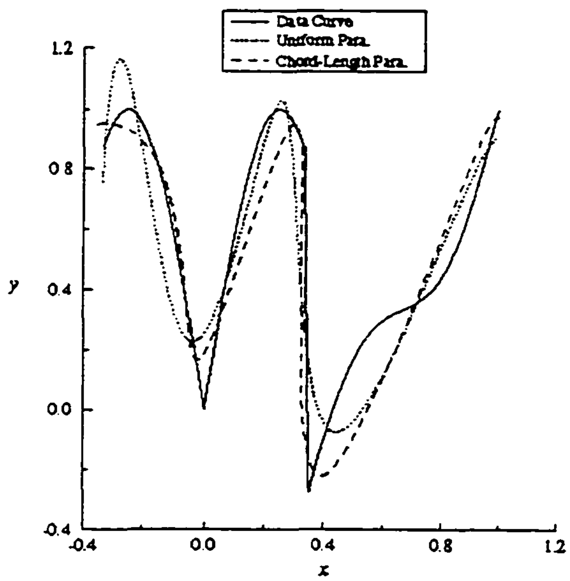

Figure 5.3: Pure B-spline fitting of the curve

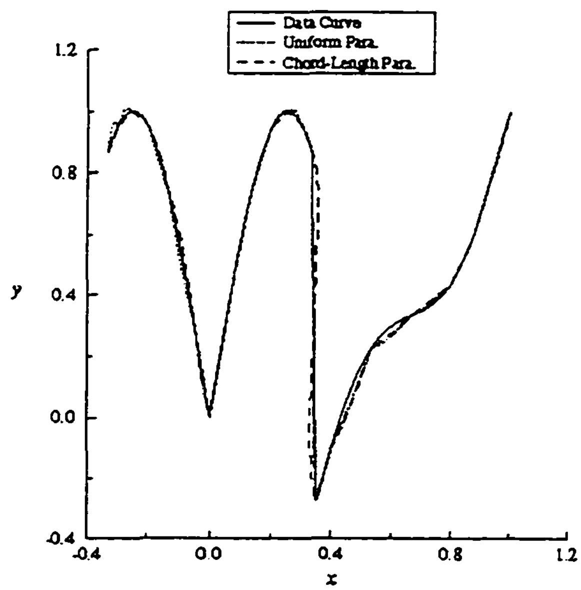

Figure 5.4: Linear covariance dual kriging interpolation of the curve

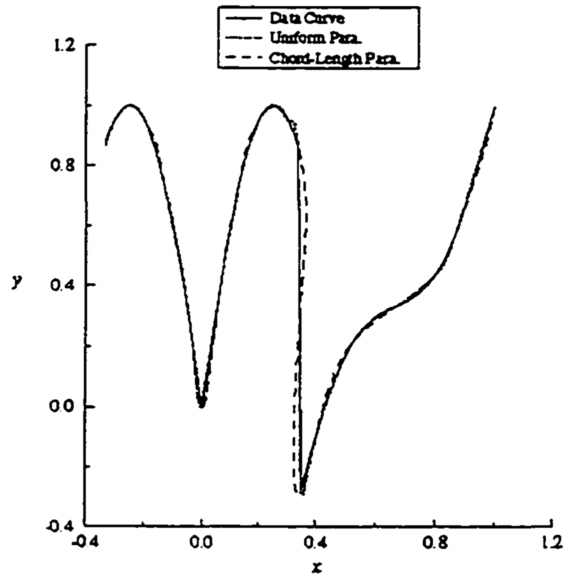

Figure 5.5: Cubic covariance dual kriging interpolation of the curve

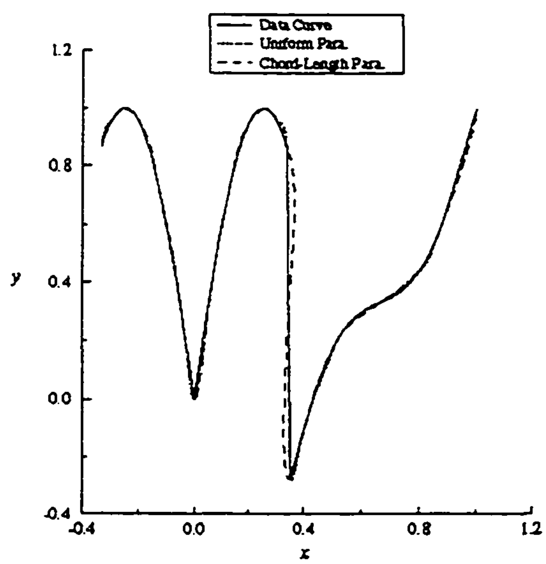

Figure 5.6: Logarithmic covariance dual kriging interpolation of the curve

It can be seen from Figure 5.3 that the pure B-spline fitting scheme (without a covariance part) yields overall unreasonable fitted curves, especially when the uniform parametrization is used. It is worth pointing out that the end points of the fit curves do not coincide to the end data points even though the open B-spline function is used. The explanation of this phenomenon is associated with the control polygon points calculated by the least squares solver. As a remedy, a constrained least squares solver or simply enforcement of the end polygon points equal to the end data points may be used. On the other hand, Figure 5.4 through Figure 5.6 demonstrate the power of the dual kriging method to recover complicated curves. Selection of the covariance functions and parameterization, however, has notable effects on the quality of the interpolated curves. It is observed that the interpolated curve using the linear covariance function can approximate very well a segment with a small curvature, for example, near the sharp point at $x \approx 0.37$ but deteriorates near the saddle point, just as in the B-spline fitting method. The interpolated curves using cubic and logarithmic covariance functions are qualitatively similar to each other, though the former recovers the original curve slightly better.

As shown in Figure 5.4 through Figure 5.6, kinks are induced around x = -0.3 and +0.32 in the interpolated curves when the uniform parametrization is used, which can be considered as a serious problem. Consequently, it may be concluded that the chord-length parametrization is preferred. A close examination of this issue may be conducted via Figure 5.7, which shows the absolute error values between the interpolated values using the logarithmic covariance function and the data generating function by Equation (5.43).

On average, the error values of the interpolations using two parametrization schemes are comparable. Our experiences show that generally this conclusion is correct when a curve is considered. When switching to surface fitting and interpolation, however, the opposite conclusion may be drawn, as will be shown in the next example.

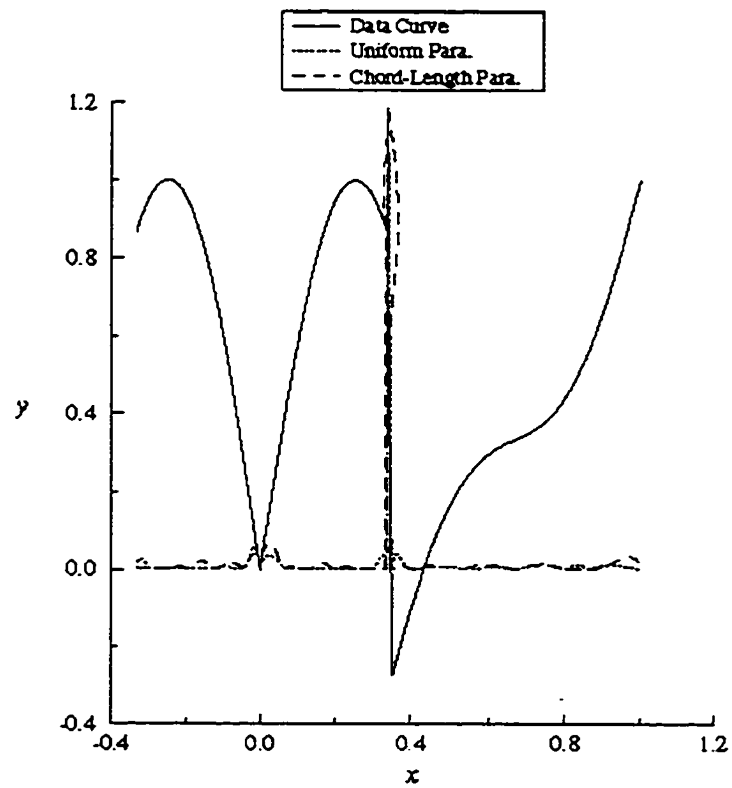

Figure 5.7: Absolute error values between interpolated and original curves with logarithmic covariance

5.4.2 Ship Hull Interpolation

The first example in applying the dual kriging method to surface approximation is a three-dimensional ship hull surface. Figure 5.8 shows a half perspective through the ship centerline (consisting of stem, keel and stern lines) and top views of the hull surface.

These data were generated from Reference [30]. In this example, we choose not to construct the surface from symmetry by creating half of the ship hull and then mirroring the other half. The purpose is to evaluate the accuracy of the dual kriging interpolation technique to represent the ship step line area where the slope discontinuity has not been prevented by imposing slope conditions. The given data points are on the shear line, W.L.3, W.L.2, W.L.1, D.W.L., 0.75 W.L., 0.5 W.L., and keel lines from stations 1 to 13. To have a rectangular parametric domain for these points, extra data points must be created for D.W.L., 0.75 W.L., 1.5 W.L., and keel lines by applying a 3-D line fitting. The total number of given data points is 11 by 25, meaning that there are twenty five points in the fore-aft direction and eleven points from the shear line to the keel line. Due to the insufficient data and incomplete ship layout from the aforementioned reference, the aft part is not considered in this work. The number of control polygon points is prescribed to be 8 by 12.

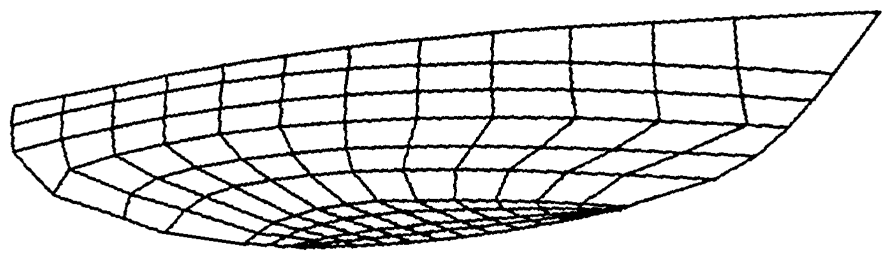

(a)

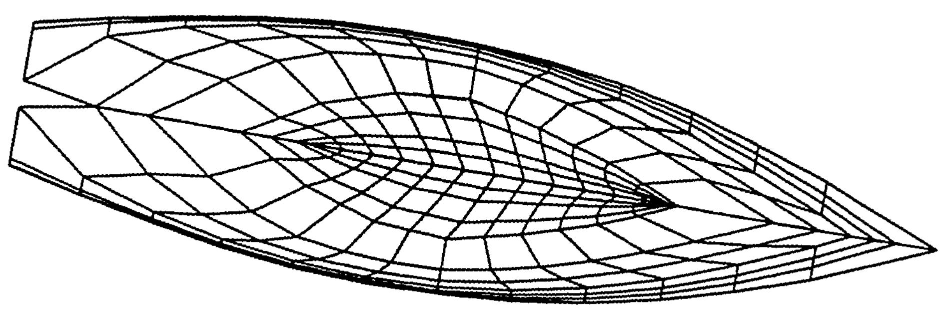

(b)

Figure 5.8: Available data points of ship hull configuration

Figure 5.9 through Figure 5.11 show the interpolated surfaces using the uniform parametrization with the different covariance functions, in which half perspective and whole top views are given by (a) and (b), respectively. It is noted that physically, all these functions result in "pulling" or "pushing" effects, which mean that the resulting surfaces are forced to pass the prescribed data points. However, the influenced areas and magnitudes of effects due to these covariance functions are different. As can be observed from Figure 5.9, a strong pulling effect appears in the narrow region near the stem line. In contrast, the pulling effect seen in Figure 5.10 and Figure 5.11 is more gentle, especially that associated with the cubic covariance function. Furthermore, a close examination reveals that in Figure 5.9(b) there appears a notable kink on the stem line. However, the kink is much smaller in Figure 5.11(b) and totally disappears in Figure 5.10(b). It may be concluded by referring to these figures that the dual kriging scheme using the cubic covariance function performs best overall, producing overall contour smoothness and a well fit stem line.

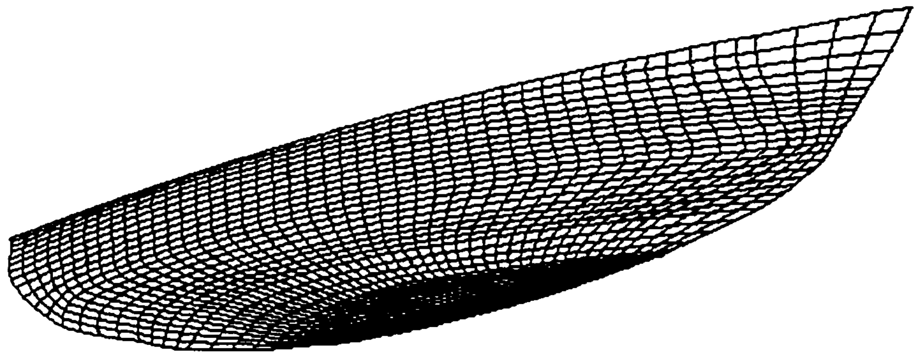

(a)

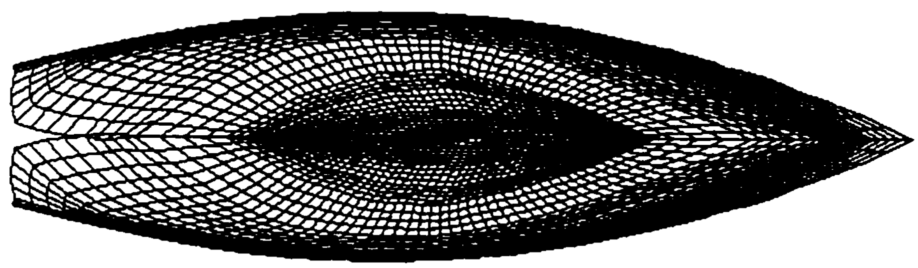

(b)

Figure5.9: Linear covariance dual kriging interpolation of the ship hull: (a) perspective view; (b) top view

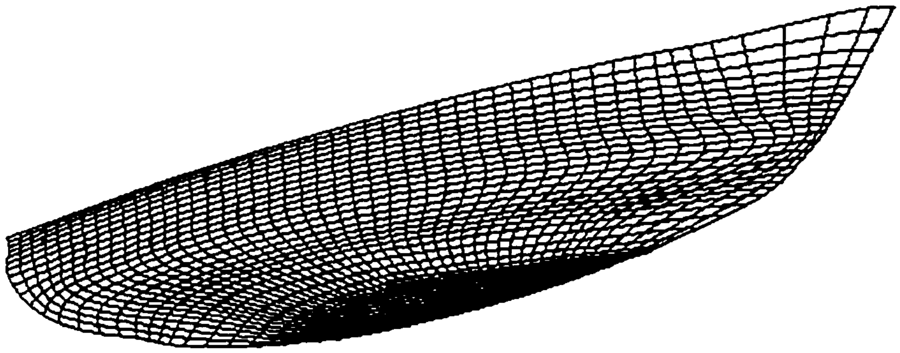

(a)

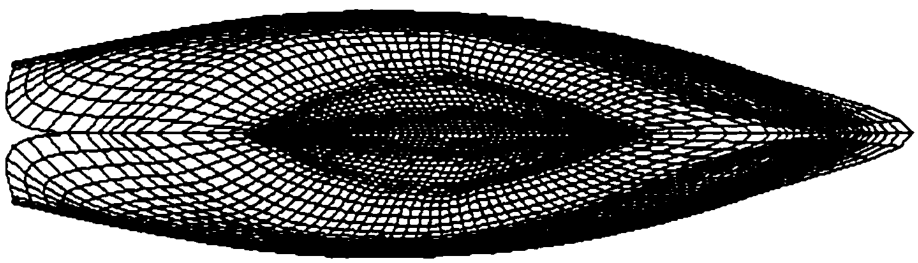

(b)

Figure5.10: Cubic covariance dual kriging interpolation of the ship hull: (a) perspective view; (b) top view

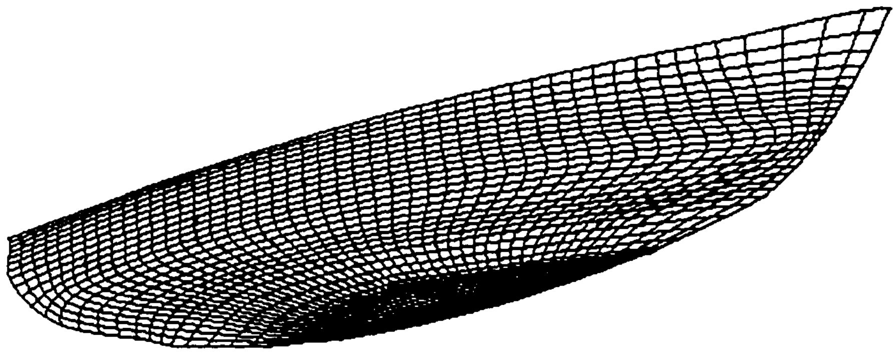

(a)

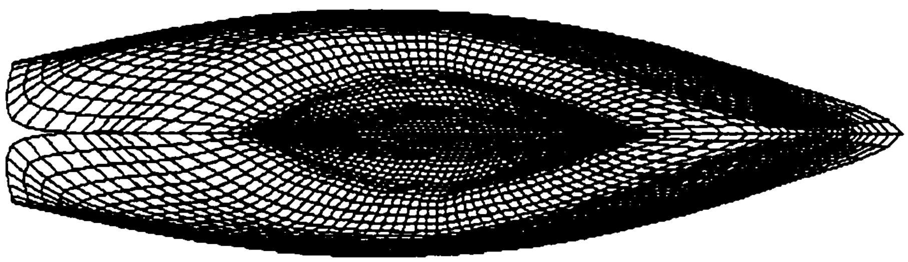

(b)

Figure5.11: Logarithmic covariance dual kriging interpolation of the ship hull: (a) perspective view; (b) top view

Figure 5.12 shows the fitted surface using an identical formulation as Figure 5.10, except that here the chord-length parametrization is invoked. The chord distances along the sixth and twelfth index curves are used for parametric u and v directions. As is obvious, severe oscillation occurs over a large portion of the interpolated surface. An explanation for this behavior can be found by referring to the chord-length plot, shown in Figure 5.13. The u chord-length curve next to the v middle one has a cluster of u parametric values near u =1. Further simulations confirm that the chord-length parameterization along the first indices u and v curves result in smooth recovery of the ship hull surface.

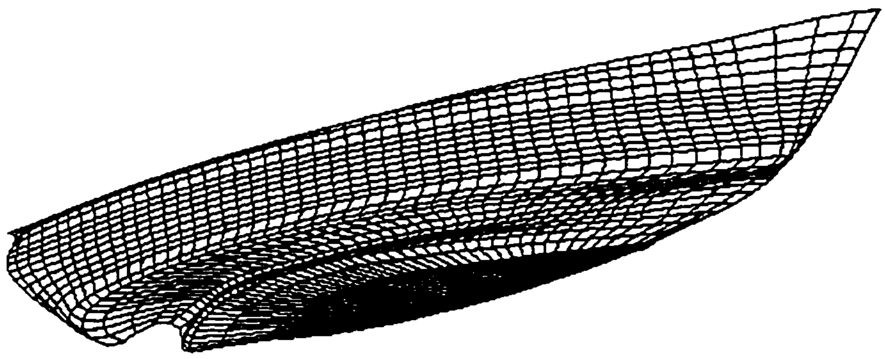

(a)

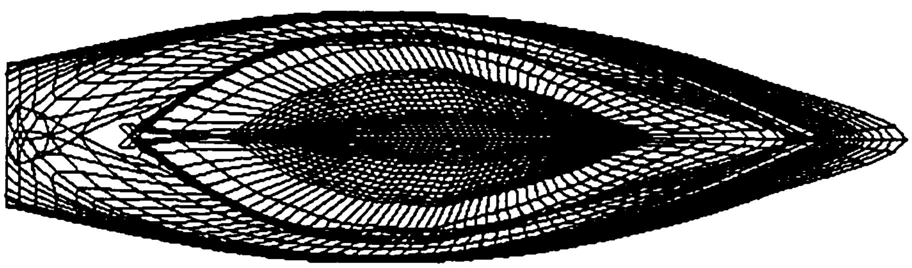

(b)

Figure 5.12: Cubic covariance dual kriging interpolation of the ship hull with chord-length parametrization: (a) perspective view; (b) top view

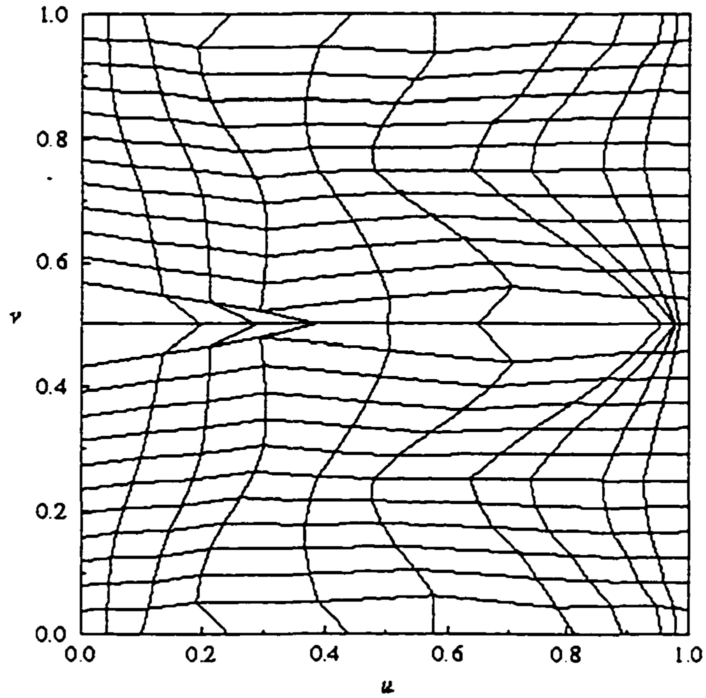

Figure 5.13: Stencil of chord-length parameterization

The above-mentioned difficulties can be partially overcome using the surface-area based parametrization technique. Figure 5.14 shows the results corresponding to Figure 5. 9 (i.e., linear covariance function) but with the surface-area based parametrization. It can be seen that the kinks experienced in using the uniform parametrization disappear (c.f. Figure 5.9). A similar phenomenon has also been observed in the results corresponding to Figure 5.11.

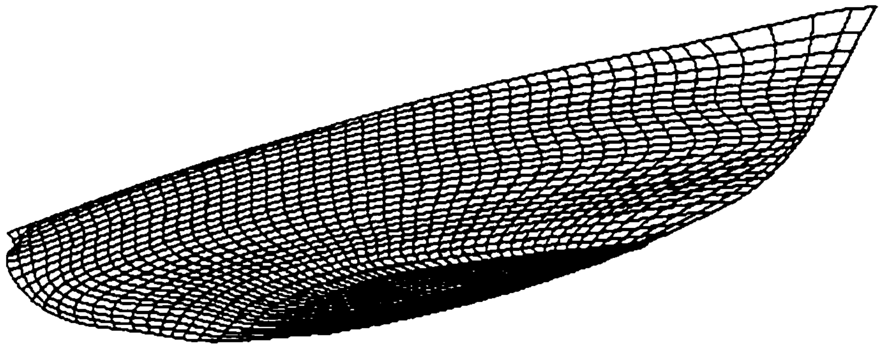

(a)

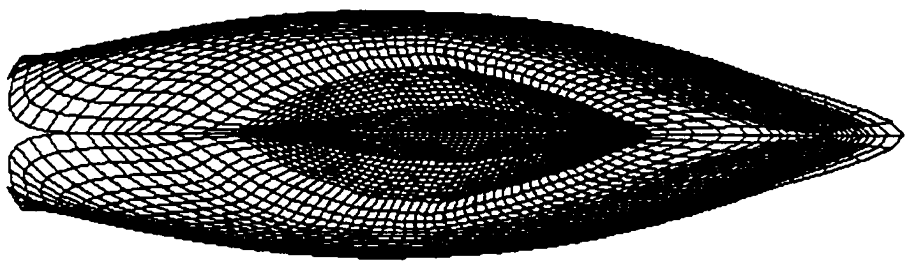

(b)

Figure 5.14: Linear covariance dual kriging interpolation of the ship hull with surface-area based parametrization: (a) perspective view; (b) top view

Further evaluation of the relative performance of different covariance functions and parametrization methods can be obtained by comparing the Gaussian and mean curvatures of the fitted surfaces. It was observed, however, that at several locations in the parameter domain (i.e., near the stern line) the curvatures have very large magnitudes that are inconsistent with the rest of the domain. This is expected given that the stern part was not fully modeled. A plot including these large values may exaggerate their importance and obscure the curvature results elsewhere. To avoid this, a prescribed cutoff value of 10 was set so that the absolute value of the curvature is within the limit of the cutoff. Two such plots are shown in Figure 5.15(a) and (b); corresponding to the uniform and the surface-area based parametrizations with the cubic covariance function, respectively. Both plots show correctly the large variation of the Gaussian curvatures near the center line ($v = 0.5$), though the result given by the surface-area based parametrization shows a wider area of influence. Both calculations show a similar phenomenon around the stern line ($u = 1$), but in this case, the surface-area based parametrization delivers a much smaller area of large curvature differences.

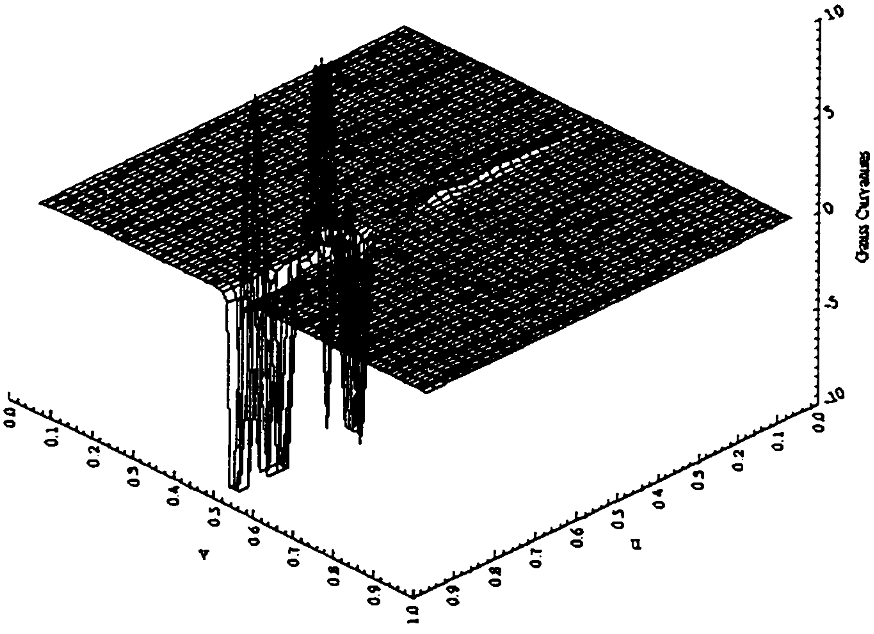

(a)

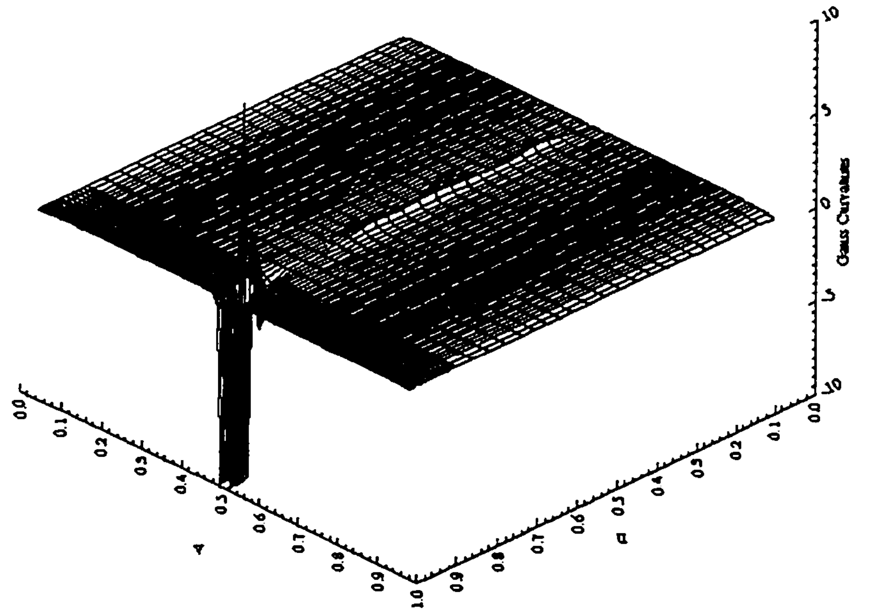

(b)

Figure 5.15: Gaussian curvatures of fitted ships with cubic covariance by (a) uniform; (b) surface-area based parametrizations

5.4.3 Human Face Interpolation

The last application example illustrates surface interpolating of a human face. Its shaded surface, consisting of 47 by 60 points, is shown in Figure 5.16. The interpolated faces by different covariance functions with either uniform or surface-area based parameterization are qualitatively very similar; thus, the cubic covariance function with uniform parametrization was selected to generate Figure 5.17. The number of control polygon points in this case was specified by 10 by 15.

The quantitative difference between various fitted faces can be demonstrated from their associated curvature calculations. Here, the effect of the parametrization is emphasized. The Gaussian curvatures of the faces corresponding to the uniform and surface-area based parametrizations with the cubic covariance function are illustrated in Figure 5.18(a) and (b). As can be seen, the surface-area based parametrization correctly distributes the grid points in the parameter domain, notably in the v-direction. It was not expected, however, that the approximated curvatures have such a small magnitude.

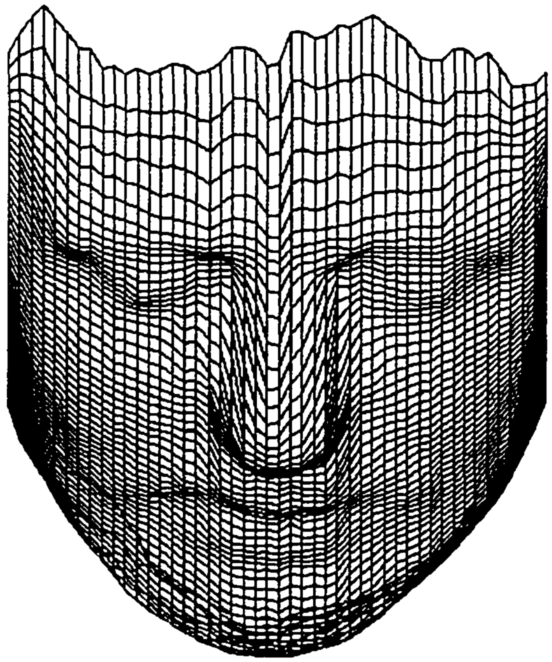

Figure 5.16: Available data points of human face

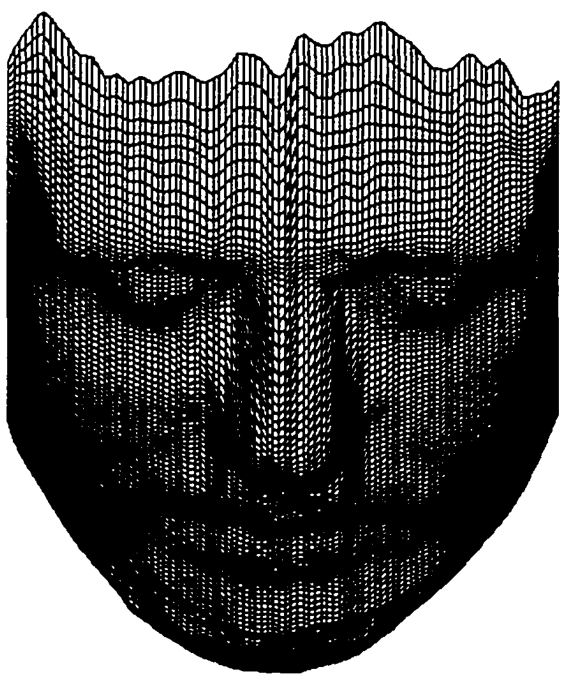

Figure 5.17: Cubic covariance interpolation of human face

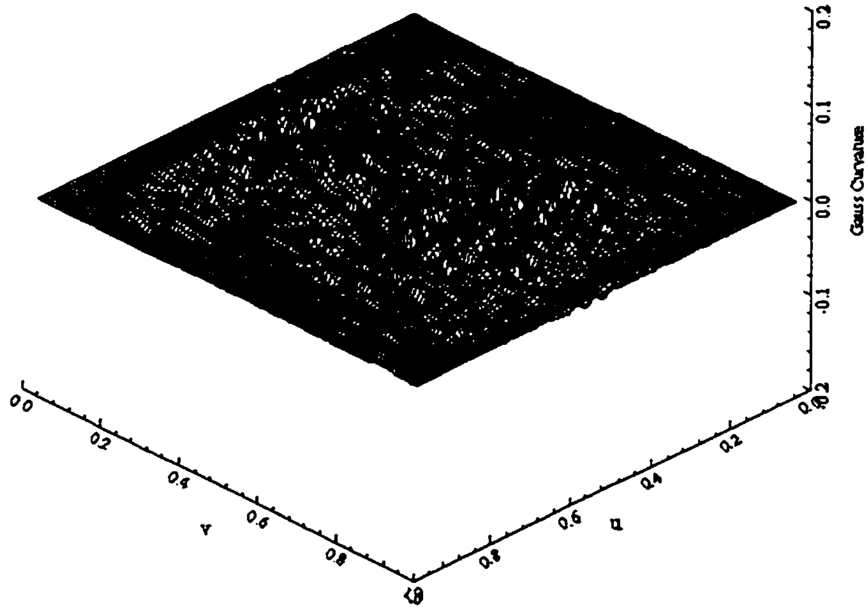

(a)

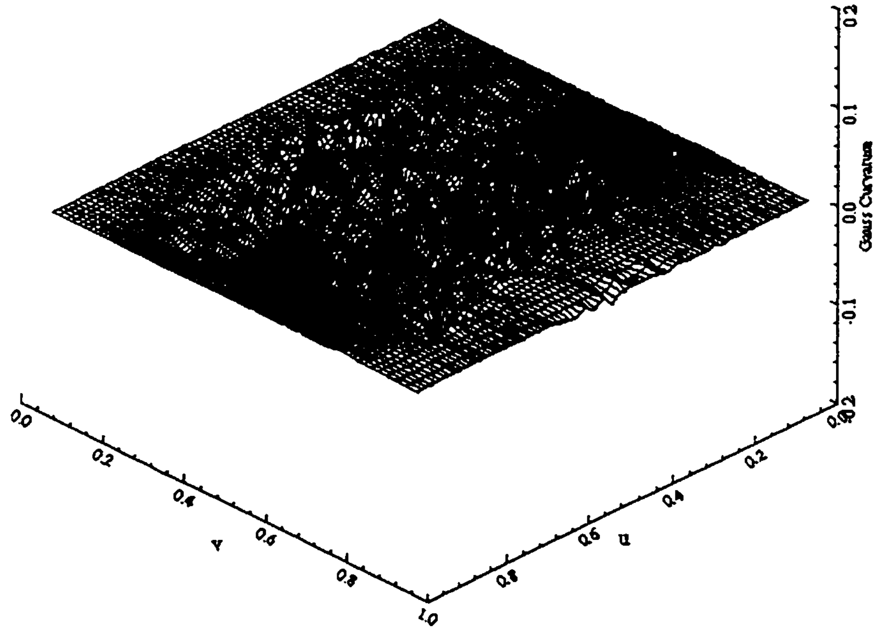

(b)

Figure 5.18: Gaussian curvatures of fitted faces by (a) uniform; (b) surface-area based parametrizations

5.5 Closure

In this chapter, derivations of the dual kriging curve and surface interpolation technique were presented in a format suitable for quasi-uniform parametrization and their rationale were discussed. Within the framework of the dual kriging method, the recovering curves and surfaces are determined by two separate parts: the draft function and the covariance function. As there are a virtually infinite number of possible combinations of these two functions, attention was limited to the cubic B-spline function as the draft function and one of four functions as the covariance function. One of the objectives is to investigate the effect of different covariance functions on the quality in the interpolated curves and surfaces. Examples lead to the conclusion that the cubic covariance is preferred overall for general shapes of curves and surfaces. On the other hand, the results with the linear covariance function show good shape recovery in regions of low continuity.

It was noted in the derivation that computational efficiency is offered for fast surface fitting by selecting a specific parametrization scheme. Three possible parametrizations, uniform, chord-length and surface-area based, were emphasized and compared. Although it is generally recommended in the literature to use either uniform or chord-length as a primary parametrization technique for a curve fitting, our results show that it may be beneficial to use the surface-area based scheme for a surface fitting because it utilizes the information of the data distribution and yields a more reasonable distribution of the parameters.

6 NODE-BASED STRUCTURAL SHAPE OPTIMIZATION

A novel node-based shape optimization method is developed for planar structures based on consideration that the critical strength and displacement constraints are generally located along or near the structural boundary. In this new method, the maximum weights were put on the selected boundary nodes of the FE model; as a result, the time-consuming sensitivity analysis is limited to the perturbation of only these nodes.

6.1 Background

Proper specification of design variables has long been one of the most important ingredients for successful shape optimization applications and many ways have been proposed to deal with this issue. The most popular methods include the design element approach [40] in which the underlying structure was divided into a number of substructures on which the overall FE model was based. The design variables were first specified at the substructure level, and then other necessary information came from interpolating by FE shape functions, for example. The approach was generally restricted to problems expected to achieve the optimal shape with a very limited range of structural shape change, because a dramatic change in structural shape may result in severe distortion of the boundary elements and leads to unreliable FE solutions.

Difficulties arise when mesh topology varies during the optimization process due to adaptive modeling, as it inevitably alters the number of nodes and elements. It may be argued, however, that the adaptive modeling is inevitable for most structural shape optimization applications for at least two reasons. First, during the iterations, the boundaries may move to such an extent that problems associated with excessive element distortions and unreasonably large aspect ratios can occur in some elements if the mesh topology is kept fixed. Figure 6.1shows such an example, in which the meshes (initial and after five iterations) consist of eight-node quadrilateral elements. As is clearly shown, a number of elements in the altered mesh have large aspect ratios which would be expected to lead to inaccurate stress solutions. Second, it is generally required for an adaptive FE model of a large structure to accurately and economically predict the locations and values of critical stresses. A uniformly refined mesh is very costly and unnecessary. On the other hand, a coarse mesh will generally underestimate the stress value in an average sense, especially near the structural boundary. Thus, adaptive meshing is also valuable in this respect.

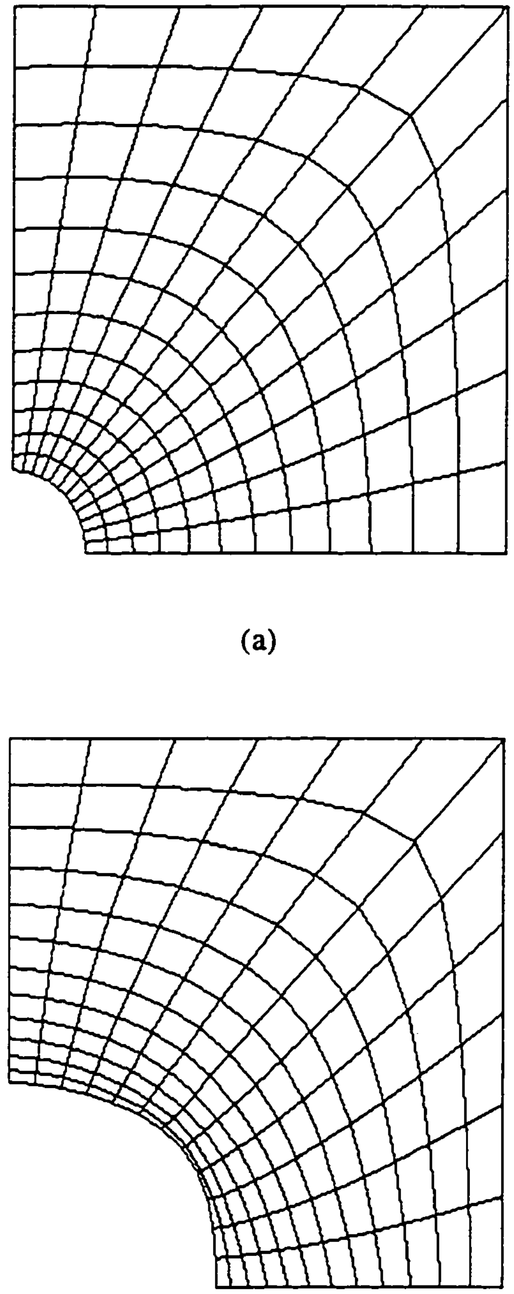

(a)

(b)

Figure 6.1: Illustration of varying meshes whose topology is fixed;

(a) initial mesh; (b) high distorted mesh

It should be pointed out that the node-based shape optimization concept itself was not initiated here. In fact, it was proposed by Zienkiewicz and Campbell [86] two and a half decades ago. Since then many application have appeared in the literature and many improvements and refining modifications have been developed. As far as we know, all applications of the node-based shape optimization technique required important information, such as sensitivity analysis results, at all nodes in the FE model. This is obviously unnecessary due to the fact that the critical constraints associated are almost always located along or near the structural boundary. Furthermore, structural weight, which in most applications is the objective function, is perturbed only if the structural boundary changes. Based on this consideration and using a technique from the boundary layer concept in viscous fluid dynamics, the proposed method put the maximum weights on the boundary nodes, referred to as the design points, so that the time-consuming sensitivity analysis is based only on the perturbation of these nodes.

6.2 Proposed Shape Optimization Method

It is proposed that only boundary information (nodal point coordinates and types of elements) be used to specify all the design variables necessary for a shape optimization design. For a boundary node, its coordinates, $\vec{r} = (x, y)^T$, define a single design variable p as

$$\vec{r} = \vec{r}_o + p\vec{s} \tag{6.1}$$

The vector $\vec{s}$ is referred to as the nodal moving velocity that can be either predetermined or recalculated at each step. Most of the optimization studies reported in the literature have employed the predetermined moving velocity methodology. The major disadvantage of this method is that it discourages the convergence of the overall iterative process because, as the structural boundary varies, the predetermined velocity may have to have its direction parallel to the boundary segment to be changed to achieve an optimal shape.

The moving velocities used in our work were recalculated at every iterative step. It is of interest to note that the nodal moving velocity can be simply expressed by

$$\bar{s} = \frac{\partial \bar{r}}{\partial p} \tag{6.2}$$

As a result, explicit expressions can be developed for moving velocities at boundary nodes as follows. Suppose that a segment of the structural boundary consists of a number of quadratic curve elements, as shown in Figure 6.2. A boundary node in this segment is identified to be either the interior node or an end node of a quadratic element. It is noted that a quadratic element consisting of three nodes i, j and k in an adequate sequence can be approximated by

$$\begin{aligned} x(\xi) &= N_i(\xi)x_i + N_j(\xi)x_j + N_k(\xi)x_k \\ y(\xi) &= N_i(\xi)y_i + N_j(\xi)y_j + N_k(\xi)y_k \end{aligned} \tag{6.3}$$

where $N_i(\xi)$ and (x_i, y_i) denote the shape function and the coordinates of the i-th node. Similar expressions can be developed for the other two nodes.

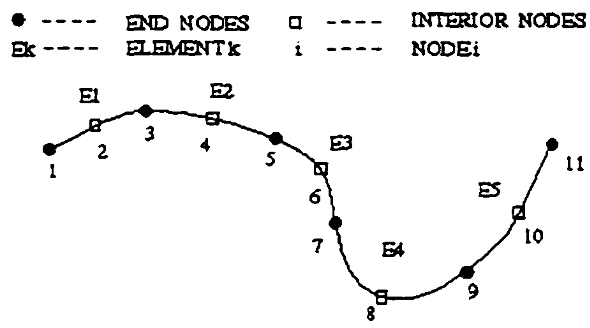

Figure 6.2: Illustration of a segment of quadratical 1-D elements

The normal vector at an arbitrary point of this element can now be represented by

$$\vec{n} = \left(y'(\xi), -x'(\xi)\right) \tag{6.4}$$

This vector can readily be used to determine the nodal moving velocities. For a node that connects to only a single element, the velocity $\vec{s}$ is simply identified as the normal vector itself. For end nodes that connect two elements, the average of two normal vectors obtained from two connected elements is used to yield the velocity. A nodal moving velocity generally includes both magnitude and direction. The magnitude may be absorbed into the design variable p so that $\vec{s}$ can be always assumed to be a normalized vector.

It has been mentioned that a design point is associated with a single design variable p. Therefore, the number of design variables can be reduced by decreasing the number of design points. It has been a common belief that curved elements are not recommended for FE solutions. Even if it is absolutely necessary to use them, interior nodes should be the midpoints of the end nodes, except when modeling a structure with singularity. Consequently, it is further proposed that only end nodes be selected as the candidates for design points. As a result of this simplification, each design variable perturbs the geometry of only one or two boundary elements, although its effects may likely be propagated into other elements by subsequent automatic mesh generation.

The sensitivity results of the objective function, the force vector and constraints with respect to p can be expressed as a summation of the product of the nodal moving velocities and the derivatives of the functions with respect to the nodal point coordinates by

$$\frac{\partial f}{\partial p} = \sum \left(\frac{\partial f}{\partial \bar{r}_i} \right)^T \frac{\partial \bar{r}_i}{\partial p} = \sum \left(\frac{\partial f}{\partial \bar{r}_i} \right)^T \bar{s}_i \tag{6.5}$$

Note that the vector $\frac{\partial f}{\partial \bar{r}_i}$ is zero if the coordinates $\bar{r}_i$ are not associated with design variables. Consequently, there are only a few nonzero sensitivities of components of the force vector and the stiffness matrix. On the other hand, the sensitivities of constraints involving the displacement are likely nonzero through the perturbation of displacement vector $\frac{\partial \{u\}}{\partial p}$. More details can be found in Chapter 4.

6.3 Implementation

To implement the present method, it is necessary to select a number of nodes as design points. As stated previously, these design points should always be on the structural boundary. Taking this into consideration, the structural boundary is first divided into a certain number of boundary segments. Each segment may be regarded as a design segment which is subjected to modification in finding an optimal structural shape. The selection of design segment is usually problem-dependent and will be discussed in the next chapter dealing with applications. Once design segments are identified, a certain number of nodes are then assigned to each segment as design points. The number of design points on each segment is initially prescribed and fixed in subsequent iterations. It should be pointed out that other boundary segments also need to be supplied with nodal points for meshing purposes. These boundary nodes can then be used to create an initial mesh system by using an automatic mesh generator.

After each iteration, the modified segment is smoothed by the dual kriging B-spline fitting technique. This smoothing procedure requires inputs of data points and number of control polygon points. Here, only design points are used to provide the required data points. Also, the number of control polygon points is specified before beginning the iterations. A suitable number depends on how the smoothed curve behaves. Too large a number of control polygon points would likely return a curve with an inordinate number of kinks. On the other hand, an underestimated number may results in a curve far from the predicted optimal shape. It was found that in general a number between one-third and one half of the number of data points is adequate.

6.4 Shape Optimization Package

The present method is incorporated into a FE solver to form an automatic adaptive shape optimization program. The main modules are shown in the flow charter, Figure 6.3. A simple description for these modules is presented as follows.

The first module requires primary information about locations of the design points and number of control polygon points. It also reads in the data concerning the initial FE

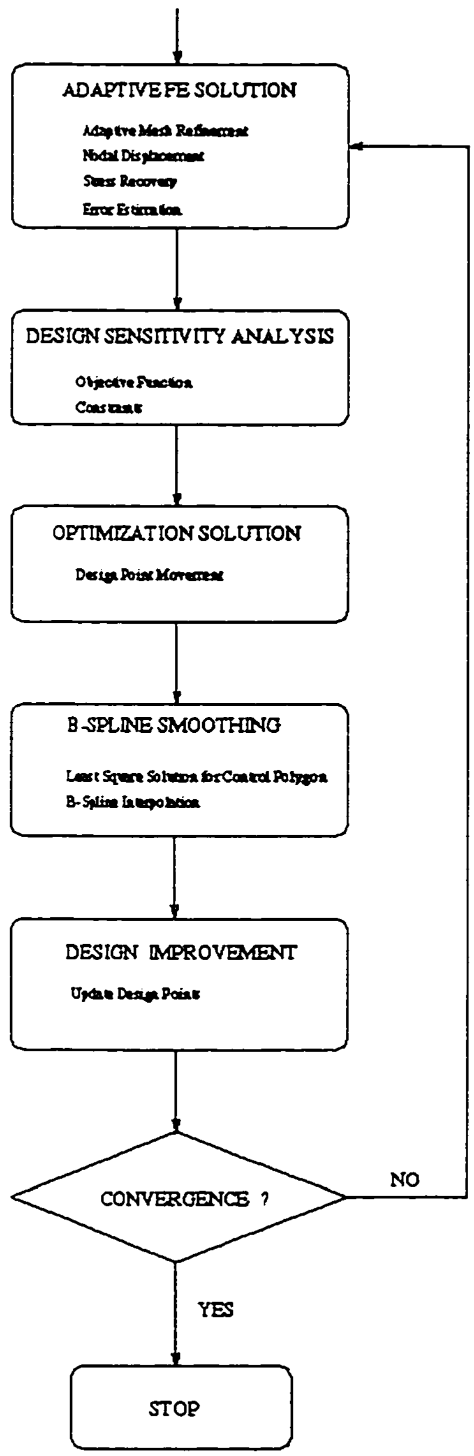

Figure 6.3: Flow chart of the proposed optimization package

model, types of constraints, the stress allowable values, and the threshold value $\bar{\eta}$ for adaptive mesh refinement.

After the input module, a certain number of iterations are performed to achieve the optimal shape design by a series of new designs. The adaptive FE solution module is intended to provide reasonably accurate displacement and stress solutions. For a new design, the initial mesh is primarily based on distortion consideration that is enforced by limiting the minimum angle allowed for each element. Based on this initial model, a FE solution, stress recovery and error estimation are then performed. Adaptive mesh refinement is invoked from the information contained in the error estimation results. During this mesh refinement process, the boundary conditions may be updated as an option because the number of boundary nodes may be increased. This is automatically done in the program by assigning sets of specific indices for the new created boundary nodes.

The design sensitivity analysis module performs the sensitivity calculations of the objective function and the constraints. In this work, the constraint information is provided by checking only the boundary elements that include at least one boundary node. This is based on the observation that the maximum stress typically occurs at the structural boundary.

With the sensitivity results available, the modified CONMIN routine is used to provide the optimal design points from the predicted optimal design variables.

The next module performs the boundary smoothing for each design segment using the dual kriging B-spline fitting technique (cf. Chapter 5). It should be pointed out that smoothing alters the predicted optimal design, but it is the present investigator's experience that this effect can be ignored because a wavy boundary is generally associated with larger values of the stress.

The final module performs the shape update. An auxiliary routine was developed for this purpose. Its used a number of system calls to automatically update input files requiring invoking automatic mesh generation.

The convergence conditions used in the package consist of checking the objective function and feasible iteration condition. If the objective function improves only marginally during five consecutive iterations, or if all of ten consecutive iterations stay in the infeasible domain, iteration stops.

7 APPLICATIONS AND DISCUSSION

In this chapter, the methods developed in the previous chapters are applied to a number of problems. The first problem is the application of the stress recovery technique to in-plane stress calculations to find the lateral buckling load factors of plate structures. Then, the applications of the proposed node-based shape optimization are demonstrated.

7.1 Plate Lateral Buckling Analysis

7.1.1 Introduction

As it is known, accurate determination of in-plane stress field is critical in predicting a buckling load and the associated mode shape. The stress recovery technique discussed in Chapter 3 can be used for this purpose. In this section, we present such an application in which a Reissner-Mindlin plate finite element approximation is used to compute the plate lateral buckling loads. The in-plane stress field induced by various in-plane loads is provided by a plane stress FE solution using nine-node isoparametric elements with the help of our SPR method.

The preference of quadrilateral elements to triangular elements is due to the following consideration. It may be recalled that one should in general avoid using a triangular plate element in any FE application in which a plate structure may be subjected to any type of bending, torsional and buckling loads. Therefore, although a triangular element mesh may be used to compute the in-plane stress field for a planar structure, the adequate quadrilateral elements (in terms of the elemental skewness, warpness and aspect ratio) are strongly recommended in FE applications with plate structures.

7.1.2 Background

While the lateral stability of beams has been explored both theoretically and numerically [71, 78, 61], few lateral buckling analyses of plates are available in the literature. The work by Kondo [46] apparently was the first one to address the lateral buckling of beams in terms of the lateral buckling analysis of plates. Using a simple plate analog to beam buckling analysis and the Rayleigh-Ritz technique, Cheng [21] presented the critical loads for several loading conditions. It should be pointed out that only part of the potential energy due to the in-plane deformations was included in his work. Cheng also found that his technique produced excessive errors whenever the plate configuration is outside of a certain range specified by the plate aspect and length-to-thickness ratios. Recently, Reissner [62] proposed a procedure to investigate theoretically the lateral buckling of plates.

The lateral buckling loads of several plate structures will be calculated using a finite element discretization based on the Reissner-Mindlin plate theory. It is known that when this approximation is applied to thin plates, a non-physical phenomenon, referred to as plate shear locking in the literature, usually occurs. To alleviate this problem, a selective reduced integration technique is used; that is, certain terms of the strain energy expression are integrated using numerical integration schemes of different orders. The effects of the aspect ratio and the length-to-thickness ratio of a rectangular plates on the buckling loads are highlighted through a set of validation problems. Other effects such as the presence of a circular hole and plate skewness are also considered and lateral buckling parameters for those cases are developed.

Before turning to other topics, it is noted that one of the major advantages in using the Reissner-Mindlin plate theory is that it is relatively easy to implement in finite element approximations with isoparametric element techniques because it allows one to neglect the issue of conforming element construction.

7.1.3 Buckling Consideration and Formulation

The Reissner-Mindlin plate theory and its FE approximation are given in the second part of Appendix A. It is shown there that the determination of the lateral buckling load is equivalent to solving for a specific eigenvalue in the following eigenproblem

$$\left([K]-\lambda[K_G]\right)\{q\}=\{0\} \tag{7.1}$$

The above generalized eigenvalue problem can be recast in the following form

$$\left(\mu[I]-[R]^{-T}[K_G][R]^{-1}\right)[R]\{q\}=\{0\} \tag{7.2}$$

where $[R]$ is an upper triangular matrix forming the Cholesky decomposition of the positive definite matrix $[K]$ such that $[K]=[R]^T[R]$. Note that the product $[R]^{-T}[K_G][R]^{-1}$ can be simply formed because $[R]^{-1}$ can be written as the product of a series of matrices, each of which differs from the unit matrix only in a single column [81]. The standard eigenvalue solver is then applied to Equation (7.2). The reciprocal of the maximum eigenvalue is an approximation of the critical load parameter P_{cr} defined by

$$k=\frac{P_{cr}L}{D} \tag{7.3}$$

where L is the characteristic length of the structure and D is the flexural rigidity. The Poisson ratio is set at 0.3 in this presentation.

7.1.4 Results and Discussion

For verification purposes, the developed FE formulation is first applied to two standard plate buckling problems in which uniform initial stress fields are predefined:

1) a rectangular plate with simply supported or clamped boundaries and a prescribed uniform uniaxial load on the two opposite edges; and
2) the same plate subjected to uniform in-plane shear loading on its edges.

These examples were also used by Cheung *et al.* [23] to validate their formulations. It was observed that the buckling loads computed here are consistently lower than those from the preceding reference, especially for moderately thick plates. The reason for this difference is that their results were generated by neglecting the rotational effects in forming the initial stress matrix, which effectively made the structures stiffer. Other than these few percent differences, the results from our calculations agree well with the known analytical, as well as the FE, solutions.

The validation results are summarized in Figure 7.1 and Figure 7.2 for uniform uniaxial and shearing loading cases, respectively, with all edges being either simply supported or clamped. The nondimensional critical parameter used in these figures is defined by

$$k = \frac{N_{cr}}{D}\left(\frac{b}{\pi}\right)^2 \tag{7.4}$$

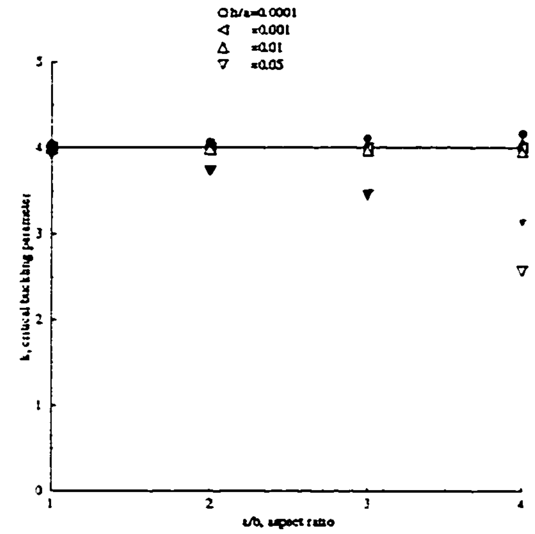

(a)

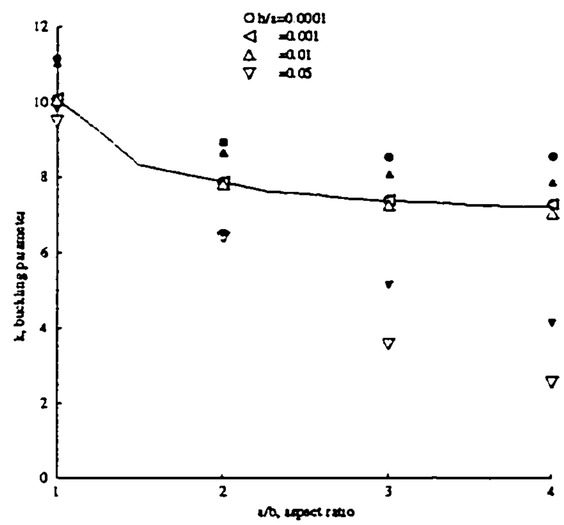

(b)

Figure 7.1: Uniaxial buckling parameters with selectively reduced (open symbols) and full integration schemes (solid symbols) for (a) S-S-S-S; (b) C-C-C-C edge boundary condition. Solid line represents the thin plate solution from [71]

where N_{cr} is the critical in-plane force per unit length (note that in general the plane stress results in this force).

Figure 7.1 and Figure 7.2 show that the selectively reduced scheme works well for relatively thin plate calculations, while it may underestimate shear stiffness in thick plate cases and consequently predict an unrealistic buckling parameter value. On the other hand, it has been noted in the literature that the full integration scheme tends to overestimate shear stiffness (shear locking) and thus overestimates the buckling load. It was observed during this study that the selectively reduced integration scheme predicted lower values of the buckling parameter compared to the values computed by the full integration scheme.

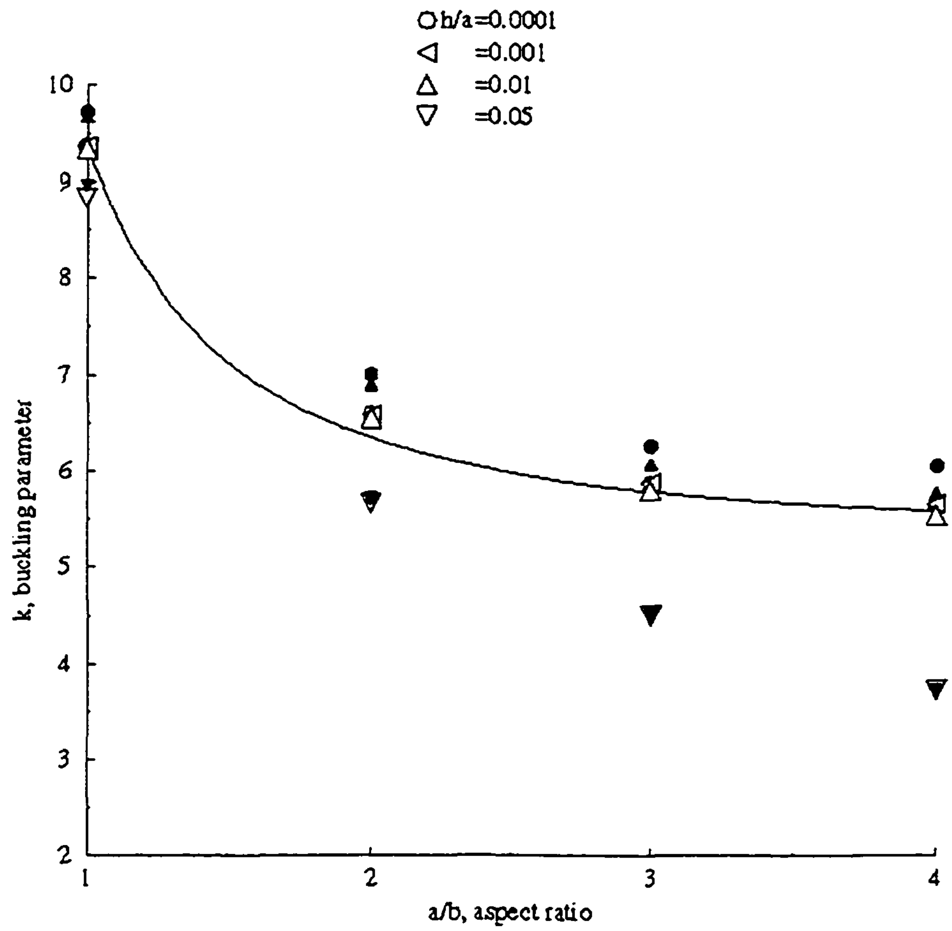
O h/a=0.0001
=0.001
=0.01
=0.05
10
9
8
7
6
5
4
3
2
k, buckling parameter
1
2
3
4
a/b, aspect ratio

(a)

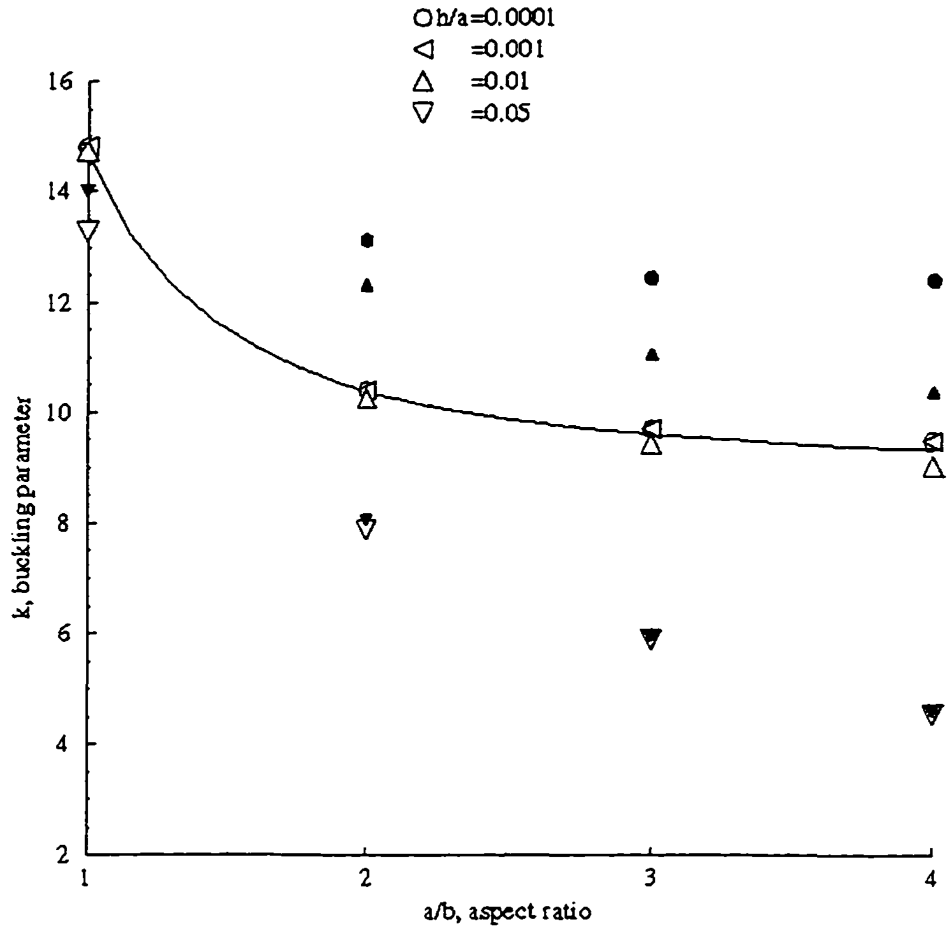

(b)

Figure 7.2: Shear buckling parameters with selectively reduced (open symbols) and full integration schemes (solid symbols) for (a) S-S-S-S; (b) C-C-C-C edge boundary condition. Solid line represents the thin plate solution from [71]

In the third validation case, the buckling load of a four-edge simply supported rectangular plate compressed by two equal concentrated loads on the two opposite edges, as shown in Figure 7.3, is computed to compare with the results from Timoshenko and Gere [71]. No displacement boundary conditions were imposed on the loaded edges in calculating the stresses and the double symmetries were used. The associated buckling parameter is defined by

$$k = \frac{P_{cr}}{D}\frac{b}{\pi} \tag{7.5}$$

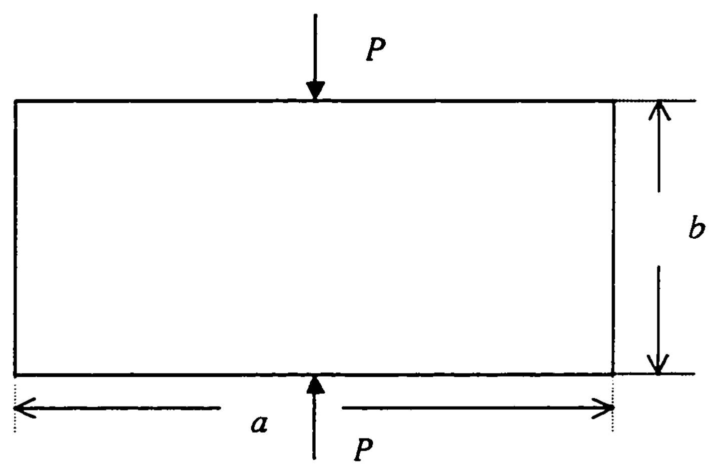

Figure 7.3: Simply supported plate compressed by two opposite concentrated loads

The buckling parameter is shown in Figure 7.4 for various plate aspect and length-to-thickness ratios. It should be emphasized that the results in the above reference were calculated in such a way that the effect of the in-plane stresses was approximated by a simple potential energy term associated with the points where the loads were applied. The regions near the loads were in compression mode and thus the exact value of the potential energy should generally be less than this simple approximation used there. Despite these differences, our calculated buckling parameters are generally in good agreement with the results in the above reference. It is also noted that, for this specific example, the neglected compressed regions are relatively small and their effect is much less critical than it would be in calculating the lateral buckling load of a rectangular cantilever plate.

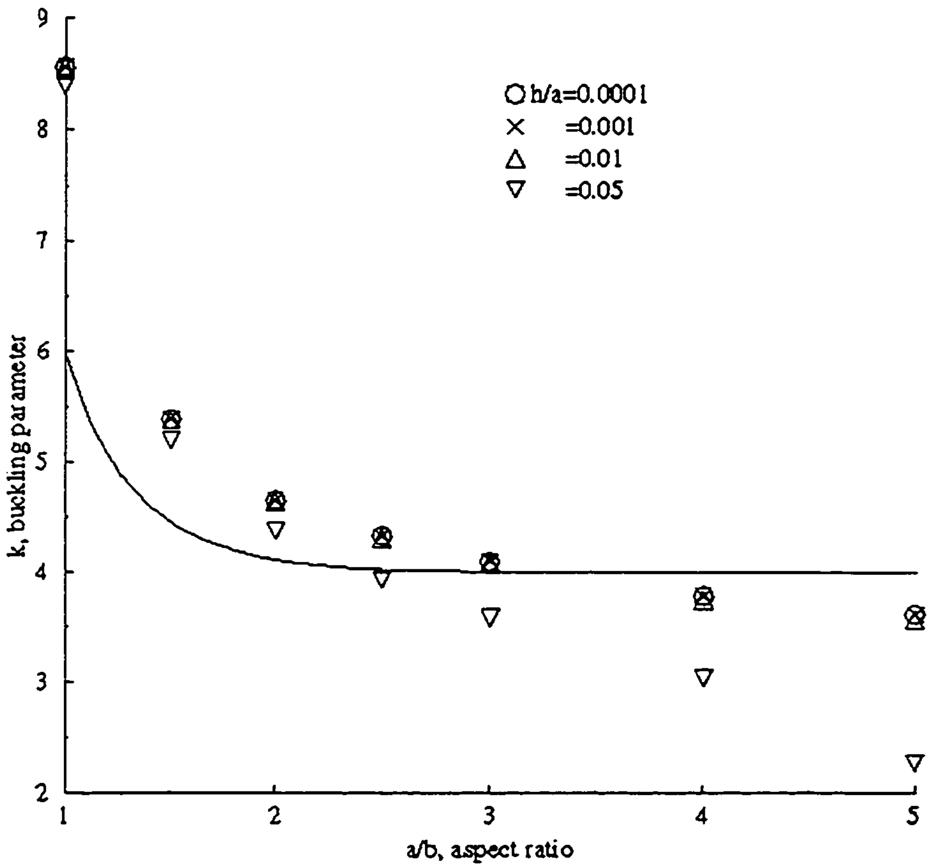

Figure 7.4: Buckling parameters for the plate configuration shown in Figure 7.3. Solid line represents the thin-plate solution from [71]

7.1.4.1 Rectangular cantilever plate

The developed FE procedure is now applied to investigate the lateral buckling problem of a simple rectangular cantilever plate. Consider a flat rectangular and isotropic plate with uniform thickness h, length a and width b, as depicted in Figure 7.5. Concentrated and distributed loads in the y direction were applied at the top edge of the mid-plane. This problem has been considered by Kondo [46] using the Rayleigh-Ritz approximation technique. There, the trial function for the lateral deflection w was approximated by a summation of characteristic functions of slender beam free vibration and the in-plane stress distribution was approximated with the simple beam solution. To our knowledge, the paper by Cheng [21] was the only other published work dealing directly with the numerical calculation of the lateral buckling loads of a simple rectangular cantilever plate. In Cheng's formulation, the potential energy due to the initial stress was approximated by an oversimplified formulation in which only a very limited area (in fact, only the concentrated loading position) was used, while the effects on the vast majority of the plate area due to the in-plane stresses were neglected. This approach works well for a beam structure, as demonstrated from our calculation when the aspect ratio is very large.

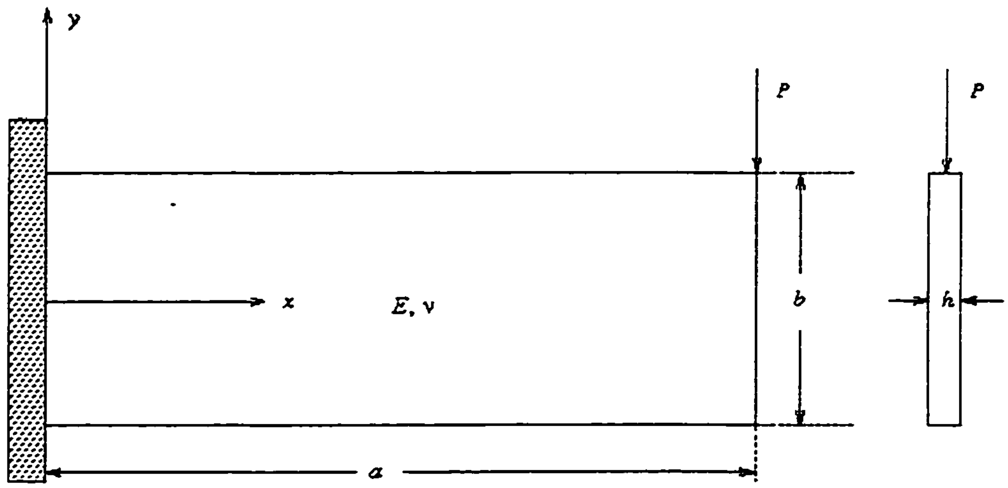

Figure 7.5: A rectangular cantilever plate with concentrated top load

As was the case for uniform in-plane loading, the buckling parameter in this case depends strongly on the plate aspect ratio and, to a lesser extent, on the length-to-thickness ratio. We first consider the case of concentrated load at the free end of the plate. Two typical loading positions are at the top ($y = b/2$) and centerline ($y = 0$) locations. The results are summarized in Figure 7.6 and Figure 7.7 in which the characteristic length L was set to b. It can be seen that when the length-to-thickness ratio is sufficiently small, the buckling parameters differ by only a few percent. In other words, those parameters in a thin plate application can be viewed as if they were not dependent on the thickness variation. The results from Cheng's work, based on the thin plate theory, are also included in the figures for comparison. It is noted in Figure 7.7 that relatively large differences exist between the current centerline loading case and Cheng's calculations for relatively small plate aspect ratios. It is not surprising that centerline loading leads to higher buckling loads than top loading, especially for the plates with small aspect ratios. As the aspect ratio increases, however, the current results tend to converge to Cheng's results, reflecting an insensitivity to end loading details. This is an illustration of Saint-Venant's principle.

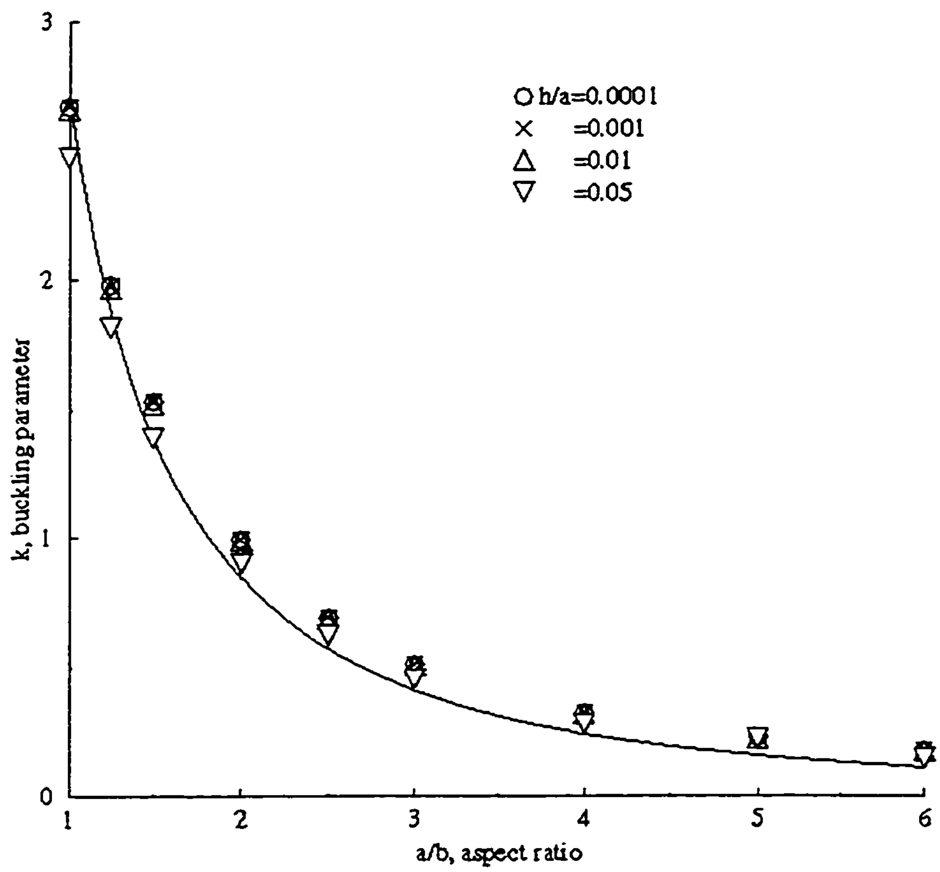

Figure 7.6: Lateral buckling parameters of a rectangular cantilever plate with a top concentrated load at $x = a$, $y = b/2$. Solid line represents the approximate solution from [21]

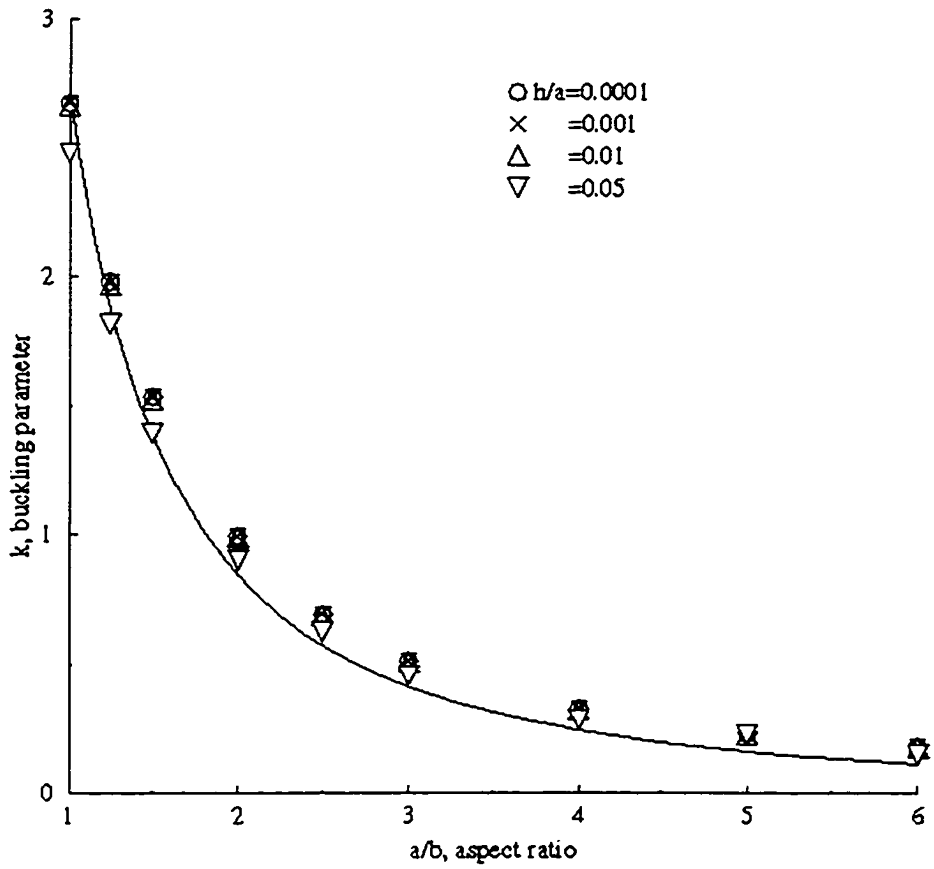

Figure 7.7: Lateral buckling parameters of a rectangular cantilever plate with a mid-width concentrated load at $x = a$, $y = 0$. Solid line represents the approximate solution from [21]

Figure 7.9 and Figure 7.10 show the values of the lateral buckling parameter for uniformly distributed loading (UDL) and triangularly distributed loading (TDL) on the top edge for typical thin plates (h/a= 0.001) (as illustrated in Figure 7.8(a) and (b)) together with Cheng's results. The buckling parameter in this case is defined by

$$k = \frac{q_{0,cr} b^2}{D} \tag{7.6}$$

where $q_{0,cr}$ represents the critical loading intensity in the UDL case or scale factor defined by

$$q = q_{0,cr}\left(1 - \frac{x}{a}\right), \tag{7.7}$$

in the TDL case. It can be seen in the figures that the differences between the results from two calculations for the UDL are minor except for the square plate case (a/b = 1), where the difference exceeded 10 percent. On the other hand, for the TDL case, larger differences exist between the two calculations across the aspect ratio range, reaching 40 percent at a/b = 1.

It can be observed from these results that the compression effects (and thus the buckling parameters) were underestimated in Cheng's approximation for the concentrated loads, while they were overestimated for the distributed loads. Recall that Cheng accounted for energy contribution only at the point where the load is applied, whereas the current analysis fully accounts for the plane deformation throughout the plate.

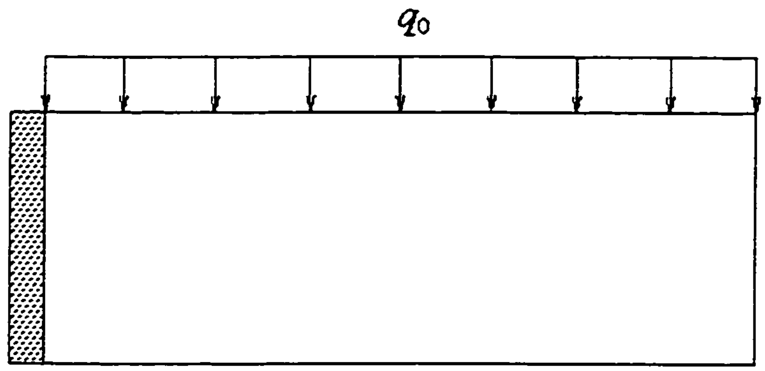

(a)

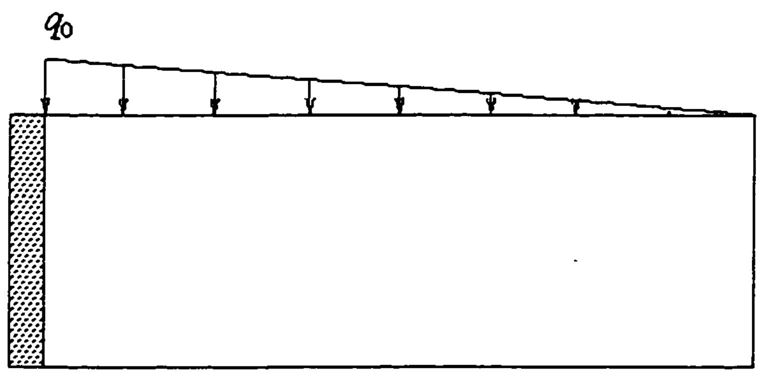

(b)

Figure 7.8: A rectangular cantilever plate with the (a) UDL; (b) TDL

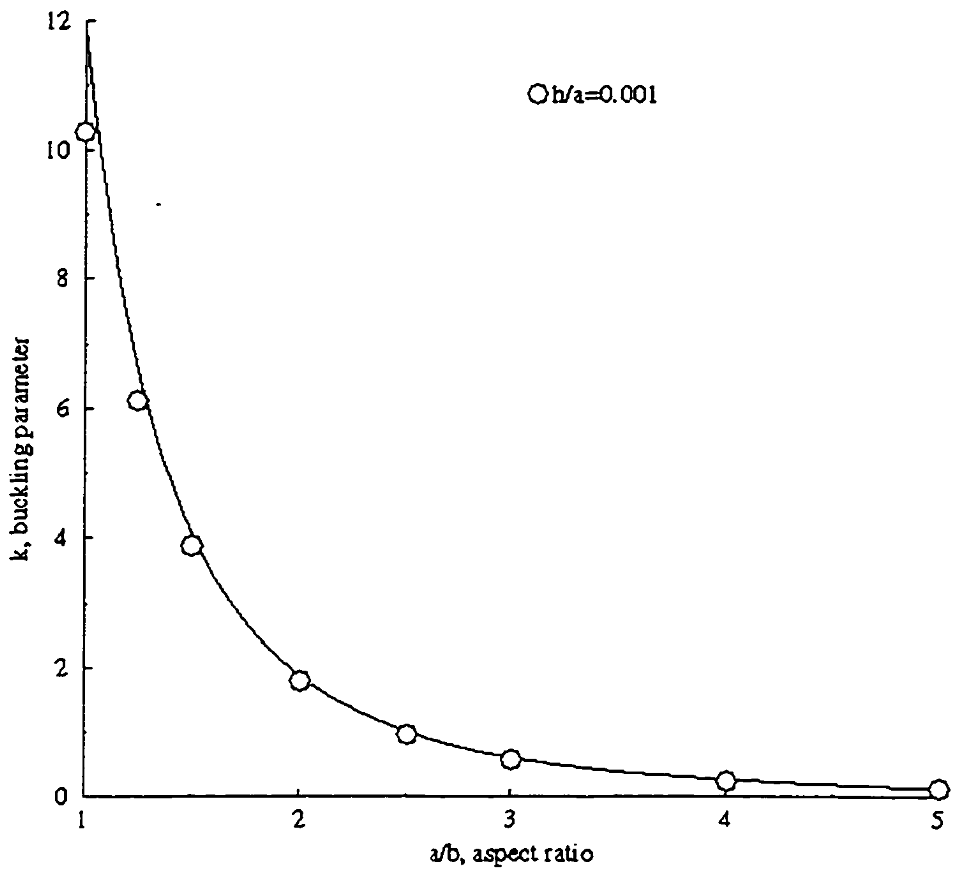

Figure 7.9: Lateral buckling parameters of a rectangular cantilever plate with a UDL (q_0)

along $y = b/2$. Solid line represents the approximate solution from [21]

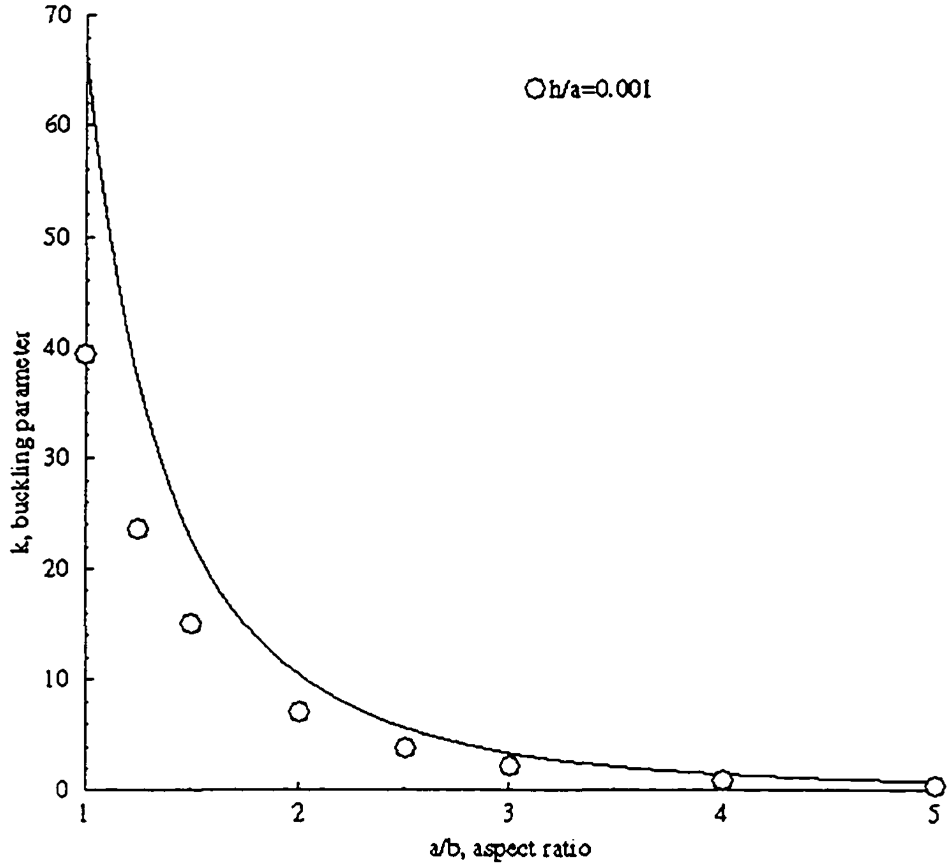

Figure 7.10: Lateral buckling parameters of a rectangular cantilever plate with a TDL given by Equation (6.9) along $y = b/2$. Solid line represents the approximate solution from [21]

7.1.4.2 Skew cantilever plate

The lateral buckling of skew cantilever plates due to tip concentrated loads is also considered. The skewness of the plate is controlled by the angle α, as shown in Figure 7.11. It is noted that a plate with skew angle $\alpha = 90°$ becomes rectangular. Also, the buckling parameter is defined in the same form as for the rectangular plate, Equation (7.4) or Equation (7.5). The calculated results are shown in Figure 7.12 for three skew angles. It can be seen that as the skew angle increases, the value of the buckling parameter also increases. Additional results for plates with skew angle larger than 90 degrees are shown in Figure 7.13 for a typical thin plate ($h/a = 0.001$). It is instructive to redefine the buckling parameter using the square root of plate area as the characteristic length L, i.e.

$$k = \frac{P_{cr}}{D}\frac{\sqrt{ab\sin\alpha}}{\pi} \tag{7.8}$$

In this way, the critical buckling parameter may be used as the buckling resistance per unit area that is useful in weight optimization practice. Figure 7.14 illustrates this area-based buckling parameter for a thin plate ($h/a= 0.001$).

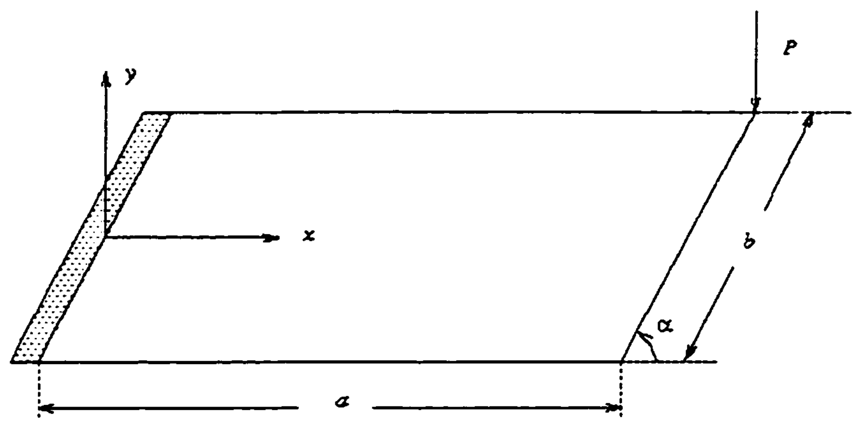

Figure 7.11: A skew cantilever plate with clamped boundary on the left edge

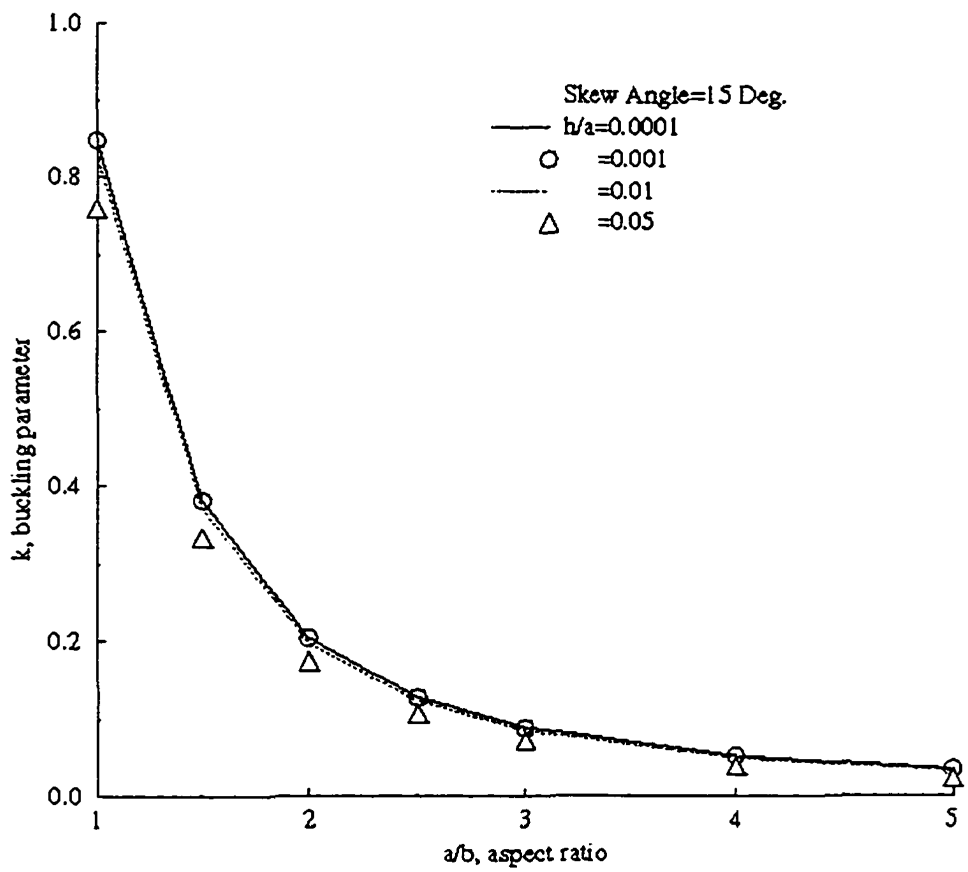
1.0
0.8
0.6
0.4
0.2
0.0
k, buckling parameter
1
2
3
4
5
a/b, aspect ratio
Skew Angle=15 Deg.
h/a=0.0001
=0.001
=0.01
=0.05

(a)

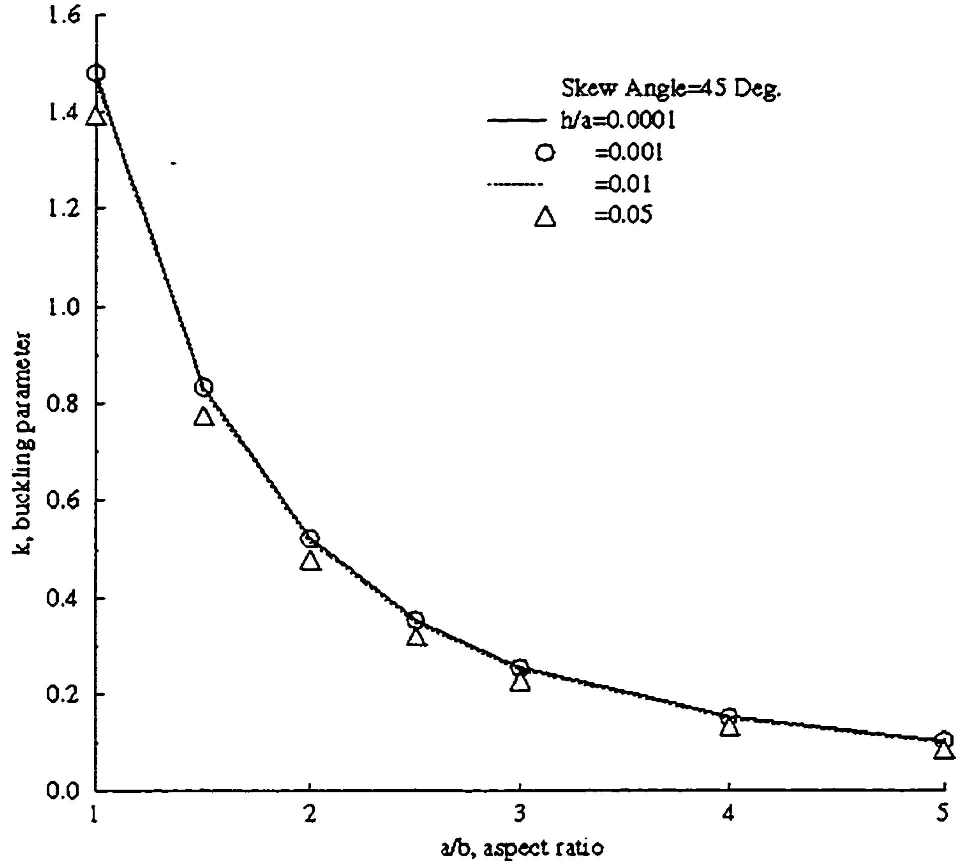
Skew Angle=45 Deg.
h/a=0.0001
=0.001
=0.01
=0.05
k, buckling parameter
0.0
0.2
0.4
0.6
0.8
1.0
1.2
1.4
1.6
1
2
3
4
5
a/b, aspect ratio

(b)

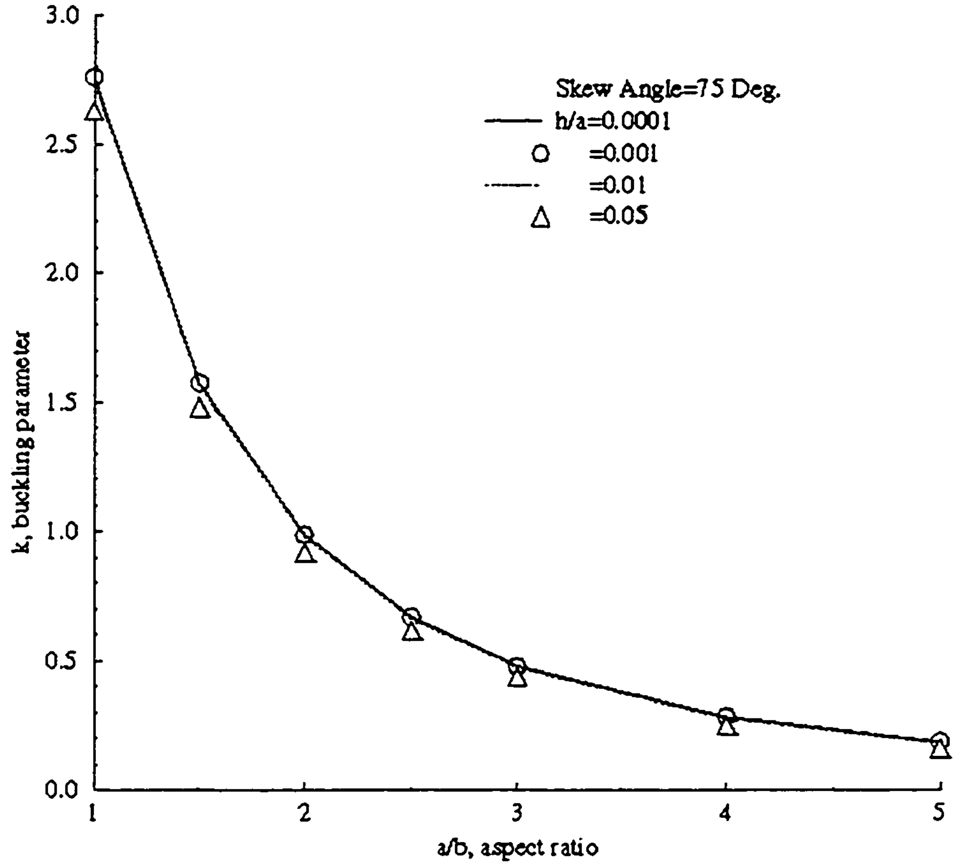

(c)

Figure 7.12: Lateral buckling parameters for concentrated top load of skew cantilever plates: (a) $\alpha = 15°$; (b) $\alpha = 45°$; (c) $\alpha = 75°$.

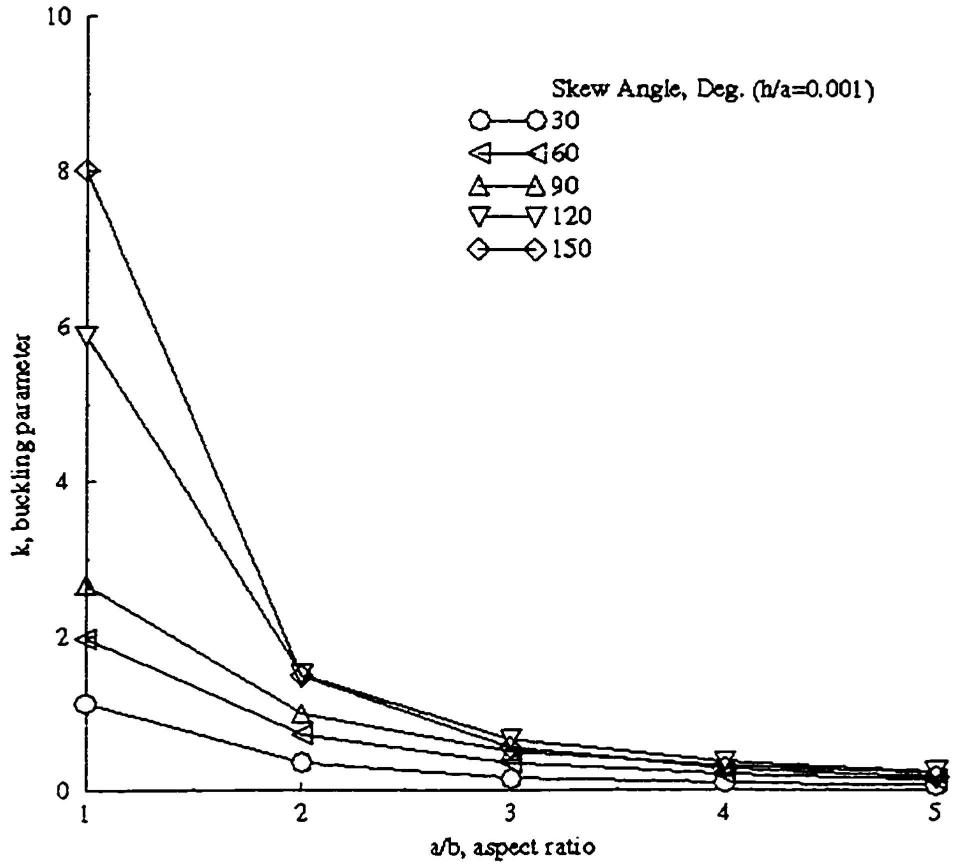

Figure 7.13: Width-based lateral buckling parameters for concentrated top load of skew cantilever plates for various skew angles

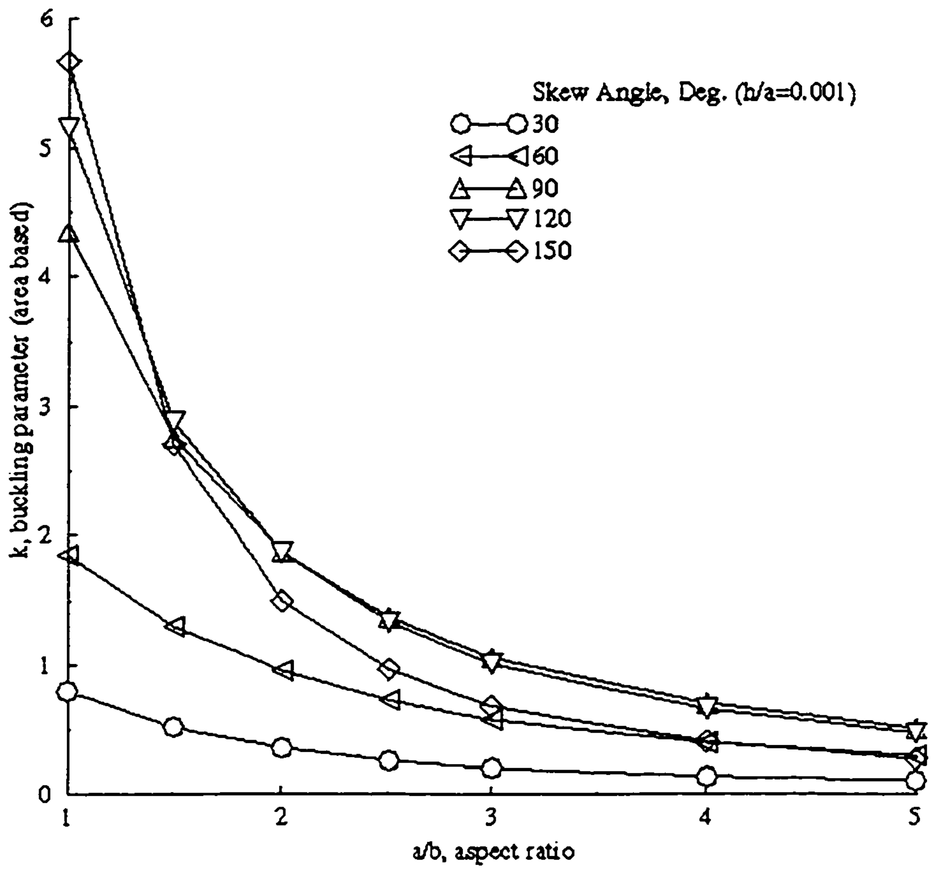

Figure 7.14: Area-based lateral buckling parameters for concentrated top load of skew cantilever plates for various skew angles

7.1.4.3 Circularly perforated cantilever plate

The lateral buckling analysis of circularly perforated cantilever plates has been reported in the literature [20]. Such plates are used extensively as the tubesheets in certain shell-tube heat exchangers and also appear in weight critical structures where the holes are created for lightening. Various loading conditions (axial, shear and bending along the edges) and locations of circular openings (concentric or eccentric) have been considered in those studies. Here, a study of the effect of circular openings on the lateral buckling loads in a rectangular cantilever plate is performed. The notation given in Figure 7.5 for the rectangular cantilever plate is retained. The radius of a circular opening is denoted by R. The center location of the opening is defined by (x_c, y_c). Alternatively, the eccentricity may also be characterized by the relative position of the opening center to the plate center, (x_e, y_e). However, as no eccentricity is considered in the current work, the geometric configuration can be specified by two ratios of aspect (a/b) and diameter-to-width ($2R/b$). Figure 7.15 shows meshes for relatively small ($2R/b = 0.1$) and large ($2R/b = 0.5$) holes, respectively.

Lateral buckling results for circularly perforated cantilever thin plates ($h/a = 0.001$) are summarized in Figure 7.16 and Figure 7.17 for loads applied at top and centerline locations, respectively. Comparing Figure 7.7 and Figure 7.16 shows that for top loading, the buckling parameter is only slightly reduced by the presence of the hole. Figure 7.8 and Figure 7.17, however, reflect a dramatic reduction in critical load for the centerline loaded case.

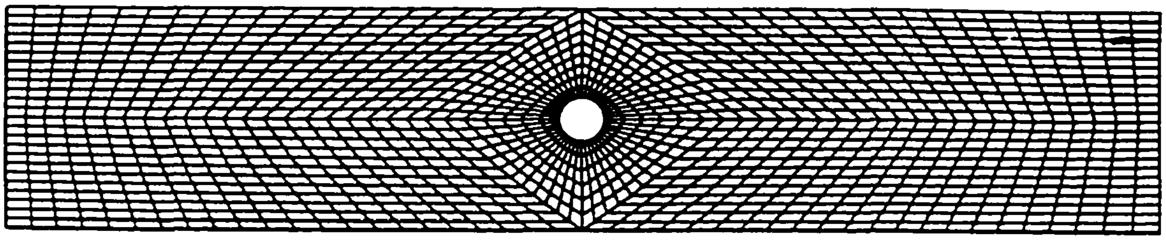

(a)

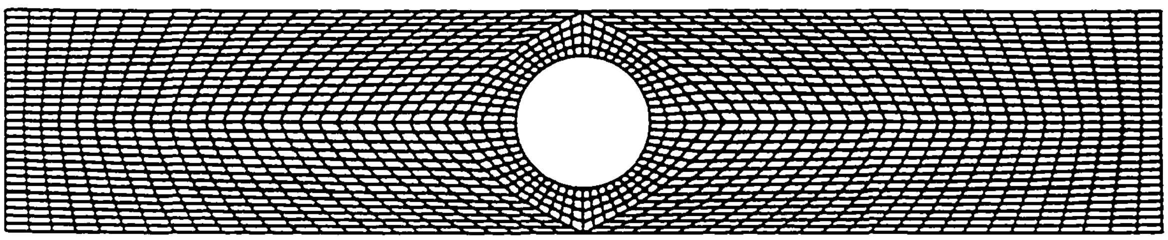

(b)

Figure 7.15: Meshes of circularly perforated plates with

(a) small hole ($2\,R/b = 0.1$); (b) large hole ($2\,R/b = 0.5$)

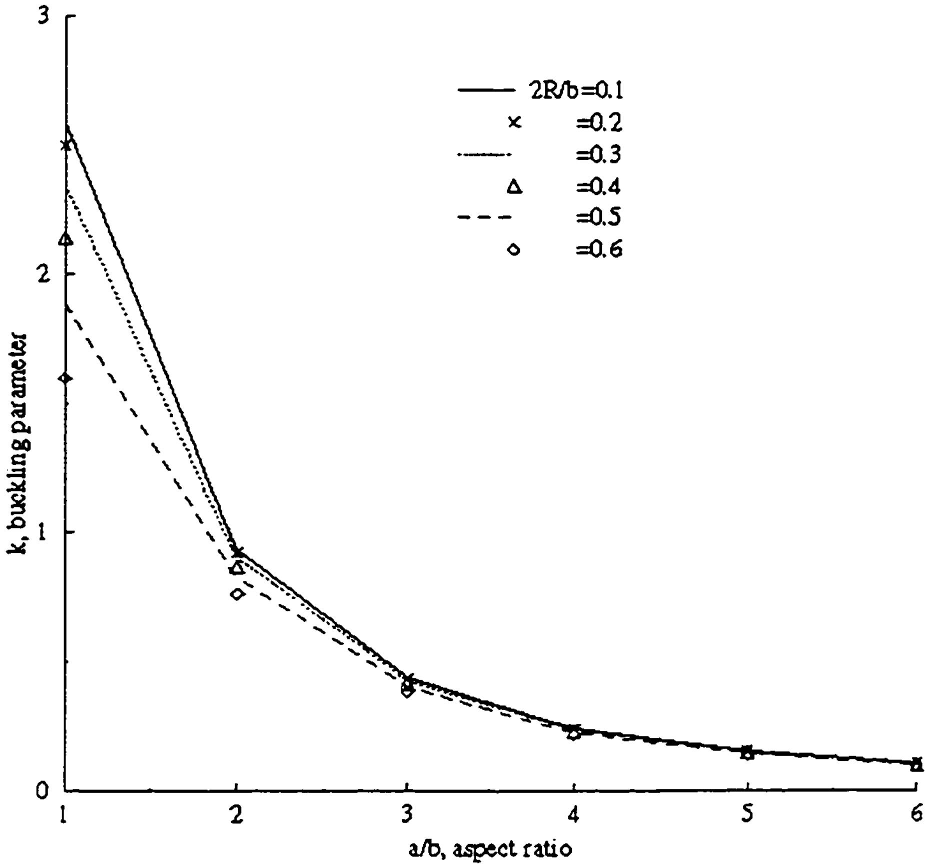

Figure 7.16: Lateral buckling parameters for circularly perforated cantilever plates under concentrated top loading.

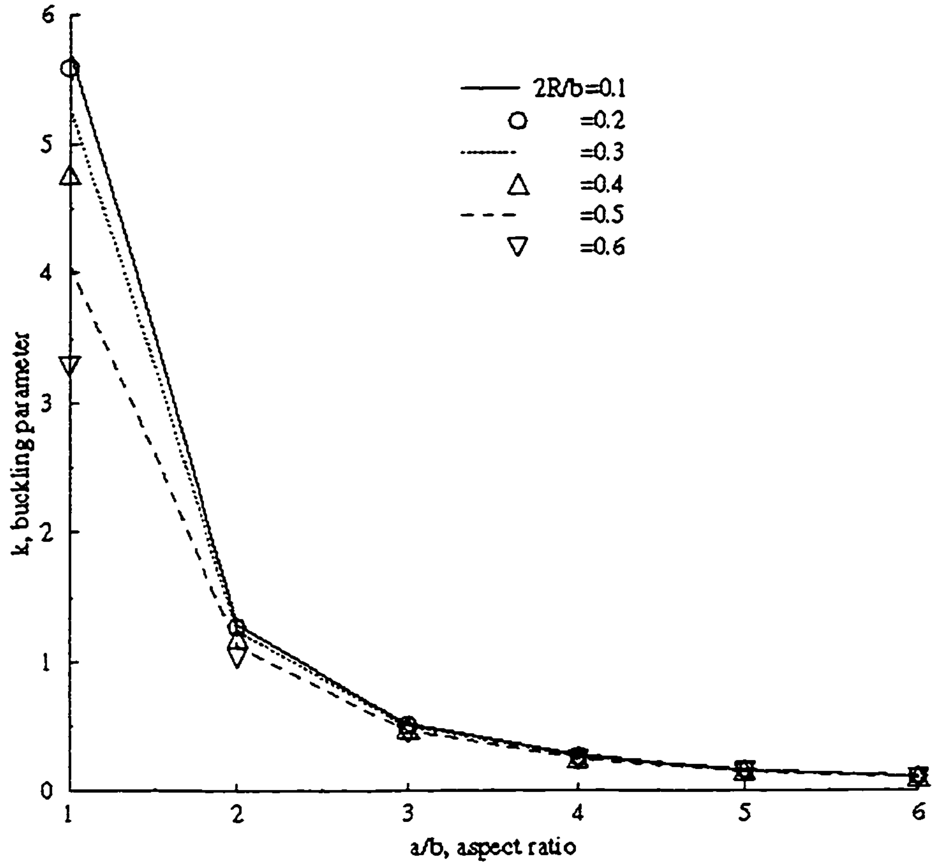

Figure 7.17: Lateral buckling parameters for circularly perforated cantilever plates under concentrated top loading

7.1.5 Closure

Calculations of the lateral buckling loads of cantilever plates using an isoparametric Reissner-Mindlin plate finite element analysis are presented. The effects of the aspect ratio and the length-to-thickness ratio of plates on the buckling loads are highlighted through a set of validation problems; the analysis was shown to be accurate. Other effects such as the presence of a circular hole and plate skewness are also considered and buckling parameters for those cases are emphasized. It was observed from the calculations that the shear locking phenomenon due to the use of full integration in the shear strain energy term did not result in any overwhelming error in predicting buckling loads as has been reported in thin plate bending computation, although it apparently does overestimate the plate stiffness.

7.2 Applications of Node-Based Structural Shape Optimization

The proposed node-based shape optimization method outlined above has been applied to several planar structures. Some of the application examples are presented next. It is noted that in using the dual kriging smoothing method, the 3rd order B-spline basis and the cubic covariance functions are chosen exclusively for these examples, unless stated otherwise.

7.2.1 Cantilever beam

We consider the optimal shape of a tip-loaded cantilever beam of rectangular cross section subjected to a yield strength constraint. The configuration and the associated FE model are shown in Figure 7.18, in which the distributed load is specified as $p = 5$ psi and the uniform thickness $t = 0.5$ in. The beam is composed of an isotropic material with an elastic Young modulus $E = 3\times10^7\,\text{psi}$ and a Poisson ratio ν = 0.0; the maximum allowable von Mises stress is $\bar{\sigma}_{\text{vm}} = 670\,\text{psi}$, which is set to be slightly greater than the maximum normal stress, 660 psi, in the initial beam predicted by classical beam theory. It should be mentioned that the Poisson ratio is set to zero to remain consistent with beam theory, which neglects the Poisson effect.

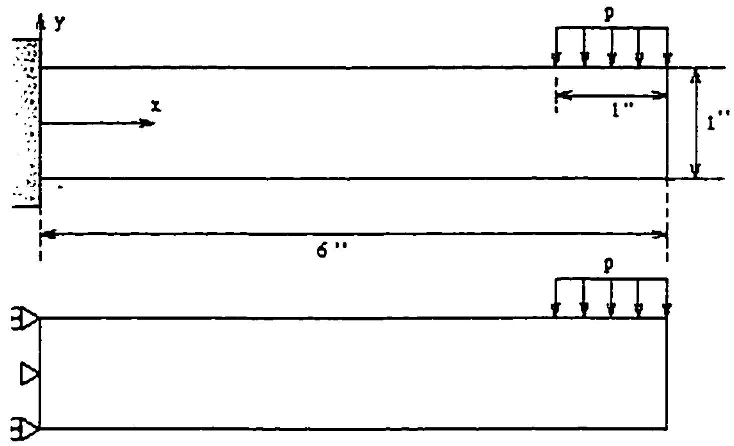

Figure 7.18: Plane stress model of a cantilever beam

Twelve design points are assigned along the bottom boundary of the beam. A constraint that allows no movement in the x-direction is imposed on the design point at the tip. Also, the y-coordinates of all design points are restricted so that they are not greater than 0.950, i.e., the beam thickness cannot vanish. Six polygon points are used for cubic B-spline smoothing in the current problem.

It is not difficult to argue that the normal x-stress at the top and bottom edges of the beam controls. It is noted that the von Mises stress near the top and bottom edges can be approximated by the absolute value of the x-stress as

$$\sigma_{\mathrm{VM}} = \left| \frac{M(x)y}{2I} \right| \tag{7.9}$$

where $M(x)$ and I represent the bending moment and the moment of inertia, respectively. The bending moment can be expressed as

$$M(x) = -5\left[(x-5)^{+2} - 2x + 11\right] \tag{7.10}$$

where function $(x-a)^{+n}$ is defined by

$$(x-a)^{+n}=\begin{cases}(x-a)^n & ,x\geq a\\ 0 & ,x<a\end{cases}$$

and the optimal shape for the bottom boundary can be approximated by

$$y=1-\sqrt{\frac{6|M(x)|}{t\overline{\sigma}_{VM}}} \tag{7.11}$$

The optimum shapes of the bottom boundary from the theoretical solution, Equation (7.11), and the numerical result are compared in Figure 7.19. Only a few percent difference is observed. Note that theoretical solution vanishes at the end, whereas the numerical solution was constrained to remain finite. It should be emphasized that the current solution takes no account of possible out-of-plane deformation and therefore, does not account for buckling as a constraint.

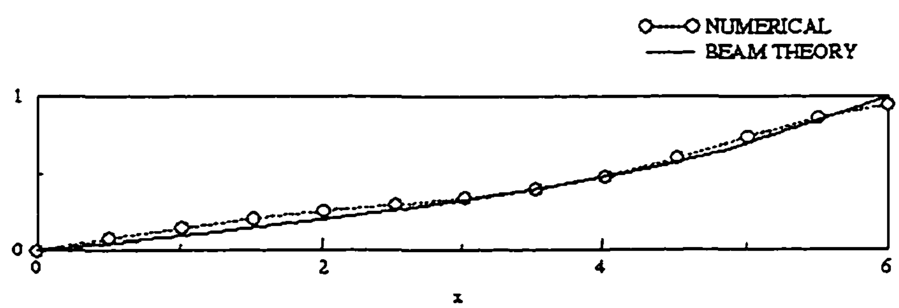

Figure 7.19: Optimal shape by numerical shape optimization and beam theory

Compared to the popular design element method (cf. Iman82), it can be seen that relatively little effort is required to set up a structural optimization process within the framework outlined here. Once the computational framework is in place, the analyst needs only to specify the initial geometry and design points. In general, it is far easier to locate the design points than to set up design element models and to prescribe moving directions for an arbitrary shape structure.

*7.2.2 **Flat plate with hole***

This classical problem has been widely investigated theoretically and numerically in the literature [48, 18, 56]. A thin 80 by 80 inches square flat plate with a central square hole of 12 by 12 inches and its FE quarter model are shown in Figure 7.20. The plate was made from an isotropic material with $E = 1.0\times10^7$ psi, $\nu = 0.3$ and the von Mises effective stress limit $\bar{\sigma}_{vm} = 3.4\times10^4$ psi. These parameters were set identical to those used by Naqib *et al.* [56]. The plate was assumed to have unit thickness. A biaxial stress field was applied by specifying p_1 = 15,000 psi and p_2 = 10,000 psi in the x- and y-directions, respectively.

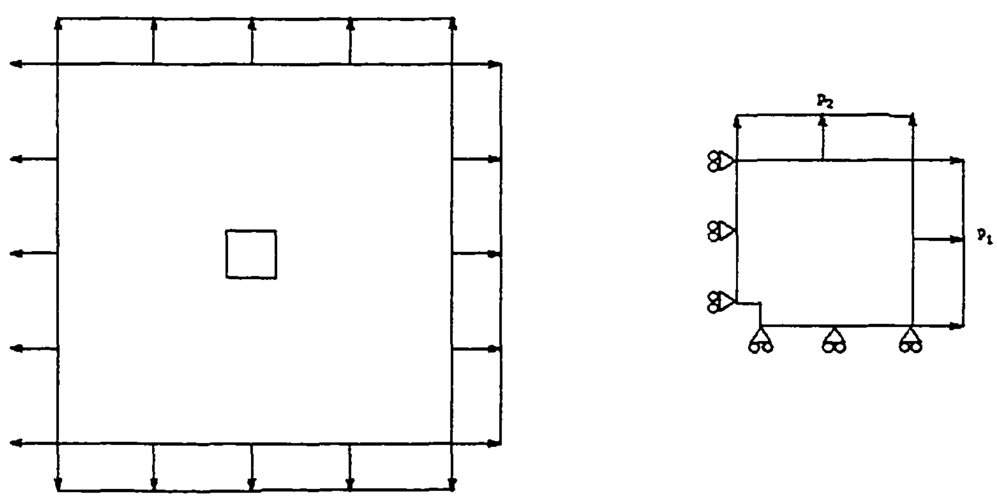

Figure 7.20: Plane stress model of plate with a square hole

The analytical solution for the optimum shape of the hole in an infinite plate under a biaxial loading conditions was summarized in [48], where it was shown that the hole should be an ellipse with the axis ratio *b/a* equal to the ratio of biaxial stresses, that is, $b/a = p_2/p_1$. The constants a and b represent the axes of the ellipse. Note however, that this conclusion was made for the infinite plate and by ignoring possible edge effects that occur when the hole axes were comparable to the plate length. Chong and Pinter [25] addressed this issue for a circular hole under the uniaxial loading conditions using FE solutions. They found that in general for the x-direction tensile load, as the hole diameter increased, the maximum x-direction normal stress, by which the stress concentration was calculated, increased as well, while absolute values of the maximum y-direction normal stress decreased.

Seventeen design points were assigned along the hole. Symmetry constraints that allowed no movement in the x- and y-directions were imposed on the design points on the y and x symmetric lines, respectively. Also, periodic re-imposition of constraints on the design points was made in such a way that their x-coordinates and y-coordinates form monotonically increasing values. It was found that this special treatment has served two purposes. First, far fewer number of iterations were needed to obtain an optimal solution since the numerical optimization procedure needed only to seek a local optimum. Second, the periodic adjustment helped to prevent premature iteration termination. Seven polygon points were used in the cubic B-spline smoothing.

The numerical optimization started with a 6 by 6 inches square quarter hole, as shown in Figure 7.20, where a high stress concentration was expected. During the first few iterations, the optimization routine tried to smooth the hole as much as possible. After five steps, the smoothed hole shape and FE mesh are shown in Figure 7.21(a). The changes in the hole shape during the next 90 iterations are shown in Figure 7.21(b)-(d). The major and minor axes ratio of the final shape was 1.43, which was only a 4.7 percent error compared with the analytical result. The contour plot of the von Mises stress at the final step is shown in Figure 7.22. It is evident that the lack of a clear local stress concentration is confirmation that material has been allocated to most efficiently carry the applied loading.

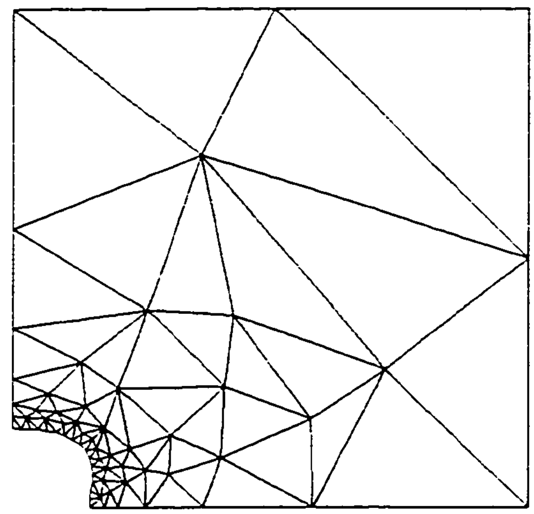

(a)

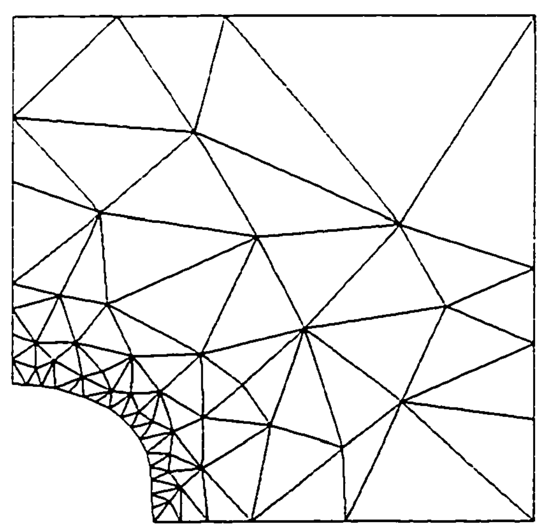

(b)

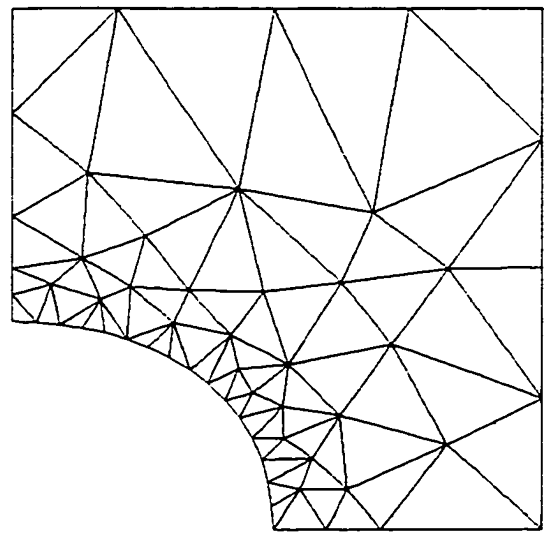

(c)

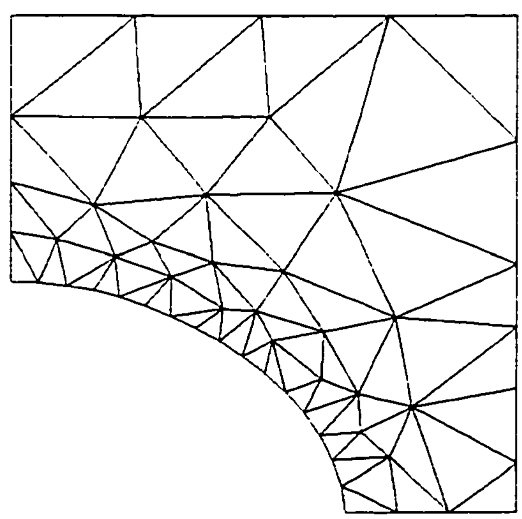

(d)

Figure 7.21: Snapshots and their meshes during shape optimization after

(a) 5 iterations; (b) 10 iterations; (c) 15 iterations; (d) 18 iterations

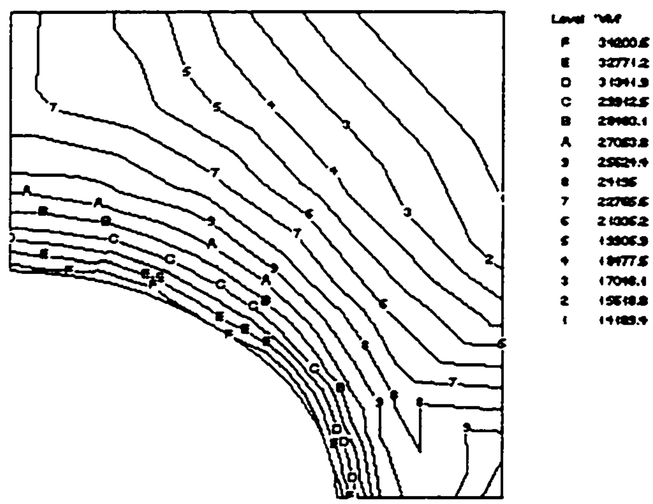

Figure 7.22: The von Mises stress contour plot

It should be mentioned that in two other runs with the initial holes being either a circle of 6 inches radius or a very irregular shape, little difference was observed between the three final optimal shapes. Thus, it has been demonstrated that this shape optimization algorithm was very robust in dealing with large shape changes. Another critical point that should be noted is that, once the problem geometry and design points were defined, the optimum shape solution proceeded automatically with no analyst intervention. Adaptive mesh refinement and local error estimation made this possible.

7.2.3 Bracket

The initial bracket and model are depicted in Figure 7.23 and the material is isotropic with $E = 1$ ksi and $\nu = 0.3$. The von Mises stress was set to be 32.5 psi.

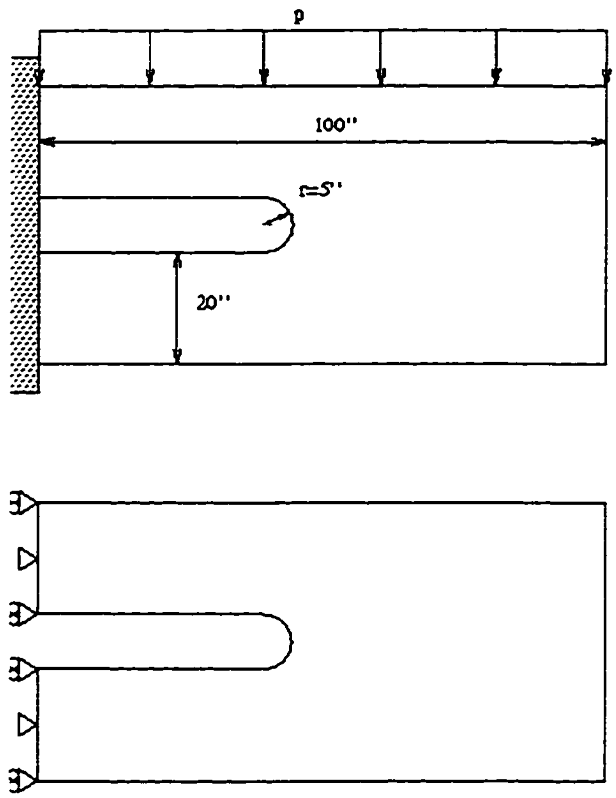

Figure 7.23: Plane stress model of a bracket

Thirteen design points and six polygon points were used along the bottom boundary in this example. Geometric constraints on the design points were imposed such that their maximum allowed y-coordinates were at least 25 inches below the top boundary. This type of constraint was necessary since the stresses in the tip region were relatively low. The numerical results are presented in Figure 7.24(a)-(d) by four snapshots, which represented the shapes at approximately the 25%, 50%, 75% and the final stages of a 21-iteration solution. In this figure one also sees continued mesh refinement near the bracket mounts and at the end of the hole. It was this continued mesh refinement that allowed the node-based technique to undergo large changes in shape during the course of the solution.

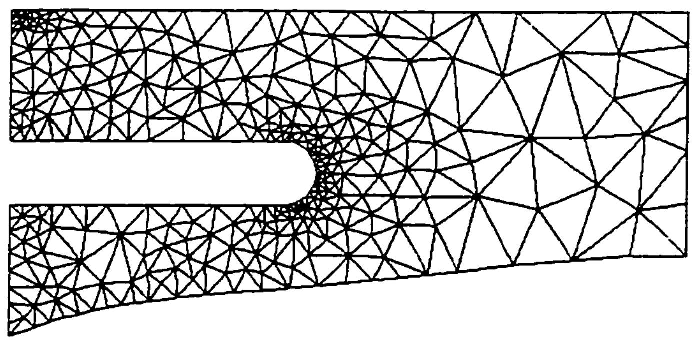

(a)

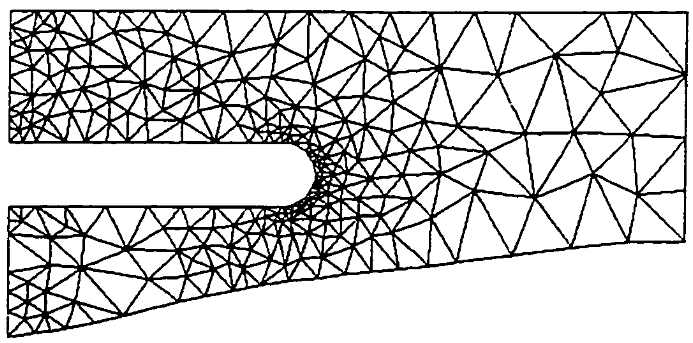

(b)

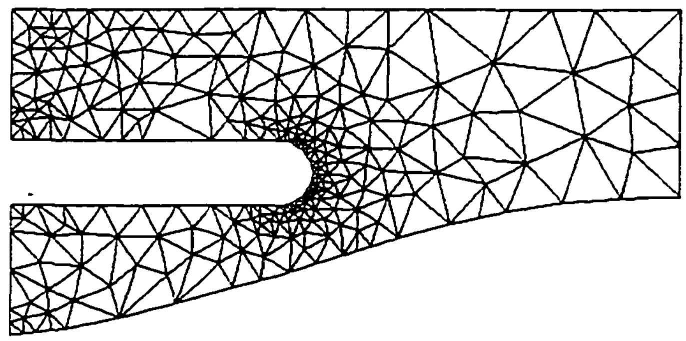

(c)

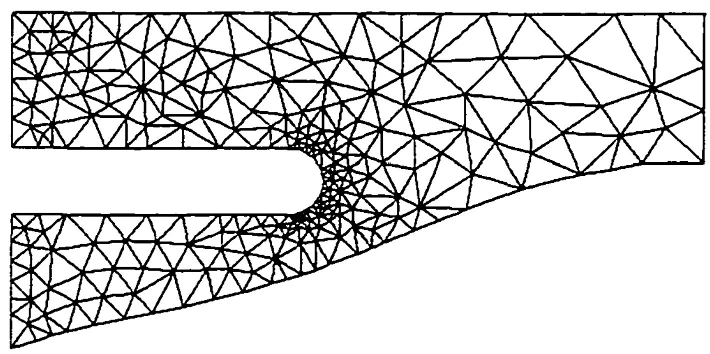

(d)

Figure 7.24: Snapshots and their meshes during shape optimization after

(a) 10 iterations; (b) 20 iterations; (c) 30 iterations; (d) 41 iterations

7.2.4 Closure

This section presents applications of a novel method of shape optimal design for general planar structures. These examples emphasize the use of information provided by boundaries of a structure, on which any area change depends and where the critical constraints normally occur. It combines the features of flexibility of nodal points and regularity of dual kriging B-spline blending functions. The varying structural shapes are modeled via adaptive mesh refinement processes so that the constraints can be calculated accurately and economically. It should be emphasized that this technique, unlike the design element method, is capable of producing large shape changes while maintaining appropriate finite element mesh distribution.

It can be concluded from these results that the present node-based shape optimization methodology avoids much of the time-consuming preprocessing required in specifying the proper design variables required by most existing shape optimization methods. By using this method, a designer is required to provide only the boundary nodes that define overall structure and the design segments connected by a number of the boundary nodes. The input required is therefore minimum.

8 CONCLUSIONS AND FUTURE STUDY

8.1 Conclusions

This dissertation covers the necessary developmental work for a computer node-based shape optimization code. Emphasis was placed on the development of error estimation, stress recovery, design sensitivity analysis, adaptive mesh generation, curve and surface smoothing methods and techniques for boundary design points and segments in which the maximum use of information provided by boundaries of a structure is made. The significance of the developed node-based shape optimization code becomes more apparent if one considers that it can handle easily the requirement that significant shape changes may take place during the optimization process. The various structural shapes are modeled using adaptive mesh refinement processes and the imposed constraints can be computed accurately and economically.

It has been pointed out that it is generally necessary for a user to try several sets of initial boundary segment and design node settings. The examples in Chapter 7 illustrated typical values of numbers for design points and polygon points. Even so, the present methodology avoids much time-consuming pre-process stage of specifying the proper design variables, as required in most existing shape optimization methods. Using the proposed method, the user is required only essentially to provide the boundary nodes that define the overall structure and the design segments connected by a number of the selected boundary nodes.

This work has successfully demonstrated that the developed automatic adaptive mesh generation, shape optimization process and the stress recovery technique work effectively, especially as a practical shape optimization tool.

8.2 Future Study

Due to the successful applications of the proposed methods to a number of 2-D planar structures, the methodology may be extended into general 3-D structural shape optimization designs. As evident from the preceeding applications, facilities for adaptive mesh generation can improve the reliability of the finite element model used during the redesign process and can therefore become a valuable tool for shape optimization. However, in general an unstructured 3-D mesh program is not available for public use, so it may be the only feasible choice to develop such a code, at least in a simplified version.

As can be seen, only plate finite elements are available at the present time. This obviously limits the application range of the current shape optimization package. So general shell elements should be investigated and implemented, which can be applied to a plate structure including the bending effects, or even to a simple shell structure. However, before such a process becomes a robust and practical tool in plate optimization design applications, the following issue must be addressed: developing robust and economical shell elements to accurately predict the bending and twist, maybe transverse shear contributions. This author started to work on this subject.

The primary feature that has made the finite element methodology so popular is its versilbility. A complicated structure can be discretized into a number of different type elements such as beams, trusses, shell elements and solid elements. One of the main future emphases is to apply the developed shape optimization methods to structures that may consist of different elements.

BIBLIOGRAPHY

1 Adelman, H.M. and Haftka, R.T., "Sensitivity Analysis for Discrete Systems," AIAA *J.*, Vol. 24(5), 814-831 (1986).

2 Akin, J.E., ***Finite Elements for Analysis and Design***, Academic Press, New York, 1994.

3 Andrews, J.D., "A Design Optimization Procedure to Minimize Fillet Bending Stresses in an Epicyclic Gear System," *Int. J. Numer. Methods Eng.*, Vol. 31, 859-878 (1991).

4 Arora, J.S., Lee, T.H. and Cardoso, J.B., "Structural Shape Sensitivity Analysis: Relationship Between Material Derivative and Control Volume Approaches," AIAA *J.*, Vol. 30(6), 1638-1648 (1992).

5 Atrek, E., Gallagher, R.H., Ragsdell, K.M. and Zienkiewicz, O.C., ***New Directions in Optimum Structural Design***, John Wiley & Son, New York, 1984.

6 Banichuk, N.V., ***Introduction to Optimization of Structures***, Springer-Verlag, New York, 1990.

7 Barlow, J., "Optimal Stress Locations in Finite Element Models," *Int. J. Numer. Methods Eng.*, Vol. 10, 243-251 (1976).

8 Bathe, K-J, ***Finite Element Procedures***, Prentice-Hall, Englewood Cliffs, New Jersey, 1996.

9 Belegundu, A.D. and Rajan, S.D., "A Shape Optimization Approach Based on Natural Design Variables and Shape Functions," *Comput. Meth. Appl. Mech. Eng.*, Vol. 66, 87-106 (1988).

10 Bendsoe, M.P. and Kikuchi, N., "Generating Optimal Topologies in Structural Design Using a Homogenization Method," *Comput. Meth. Appl. Mech. Eng.*, Vol. 71, 197-224 (1988).

11 Bendsoe, M.P., ***Optimization of Structural Topology, Shape, and Material***, Springer-Verlag, New York, 1995.

12 Bennett, J.A. and Botkin, M.E., "Structural Shape Optimization with Geometric Description and Adaptive Mesh Refinement," AIAA *J.*, Vol. 23(1), 458-464 (1985).

13 Bennett, J.A. and Botkin, M.E., ***The Optimum Shape - Automated Structural Design***, Plenum, New York, 1986.

14 Berke, L. and Khot, N.S., "Structural Optimization Using Optimality Criteria," in ***Computer Aided Structural Design: Structural and Mechanical Systems***, Edited by C.A. Mota Soares, Springer-Verlag, New York, 1987.

15 Bhavikatti, S.S. and Ramakrishnan, C.V., "Optimum Shape Design of Rotating Disks," *Comput. Struct.*, Vol. 11, 397-401 (1980).

16 Botkin, M.E., "Shape Optimization of Plate and Shell Structures, "AIAA *J.*, Vol. 20(2), 268-273 (1982).

17 Botkin, M.E. and Bennett, J.A., "Shape Optimization of Three-Dimensional Folded-Plate Structures," AIAA *J.*, Vol. 23(11), 1804-1810 (1985).

18 Braibant, V. and Fleury, C., "Shape Optimal Design Using B-Spline," *Comput. Meth. Appl. Mech. Eng.*, Vol. 44, 247-267 (1984).

19 Brockman, R.A. and Lund, F.A., "Sensitivity Analysis with Plate and Shell Finite Elements," *Int. J. Numer. Methods Eng.*, Vol. 26, 1129-1143 (1988).

20 Cheng, P. and Redwood, R.C., "Elastic buckling of web plates with eccentric openings," in ***Modeling and Simulation in Engineering***, Edited by W.F. Ames, *et al.*, North Holland Publishing Company, Amsterdam, 1983.

21 Cheng, X.S., "On Several Problems for Lateral Instability of Cantilever Plates," *Appl. Math. Mech.*, Vol. 9, 787-792(1988).

22 Cheu, T., "Sensitivity Analysis and Shape Optimization of Axisymmetric Structures," *Int. J. Numer. Methods Eng.*, Vol. 28, 95-108 (1989).

23 Cheung, Y.K., Chan. A.H.C. and Tham, L.G., "A Study on the Linear Elastic Stability of Mindlin Plates," *Int. J. Numer. Methods Eng.* Vol. 22, 117-132(1986).

24 Choi, K.K. and Twu, S., "Equivalence of Continuum and Discrete Methods of Shape Design Sensitivity Analysis," AIAA *J.*, Vol. 27(10), 1418-1424 (1989).

25 Chong, K.P. and Pinter, W.J., "Stress Concentrations of Tensile Strips With Large Holes," *Comput. Struct.*, Vol. 19, 583-589(1984).

26 Davis, J.C., ***Statistics and Data Analysis in Geology***, 2nd Edition, John Wiley, New York, 1986.

27 Ding, Y., "Shape Optimization of Structures - A Literature Survey," *Comput. Struct.*, Vol. 24(6), 985-1004 (1986).

28 Dowd, P.A., "A Review of Geostatistical Techniques for Contouring" in ***Fundamental Algorithms for Computer Graphics***, R.A. Earnshaw, Ed., Springer-Verlag, Berlin/Heidelberg, Germany, 1995, 481-529

29 Dubrule, O., "Two Methods with Different Objectives: Splines and Kriging", *J. of Intern. Assoc. Math. Geol.*, Vol. 15, No. 2, 245-257 (1983)

30 Duncan, J.P., and Mair, S.G., ***Sculptured Surfaces in Engineering and Medicine***, Cambridge University Press, New York, 1983.

31 Gates, A.A. and Accorsi, M.L., "Automatic Shape Optimization of Three-Dimensional Shell Structures with Large Shape Changes," *Comput. Struct.*, Vol. 49, 167-178, (1993).

32 Gilbert, R., Carrier, R., Benoit, C., Soulie, M., and Schiettekatte, J., "Applications of Dual Kriging in Human Factors Engineering" in ***Advances in Industrial Ergonomics and Safety II***, Biman Das, Ed., Taylor & Francis, London, 1990, 873-880

33 Goldberg, D.E., ***Genetic Algorithms in Search, Optimization, and Machine Learning***, Addison-Wesley, Reading, Massachusetts, 1989.

34 Haftka, R.T. and Prasad, B., "Optimum Structural Design With Plate Bending Elements – A Survey," AIAA *J.*, Vol. 19(4), 517-522 (1981).

35 Haftka, R.T. and Grandhi, R.V., "Structural Shape Optimization - A Survey," *Comp. Meth. Appl. Mech. Eng.*, Vol. 57, 91-106 (1986).

36 Haftka, R.T. and Gurdal, Z., ***Elements of Structural Optimization***, 3rd Ed., Kluwer Academic Publisher, New York, 1992.

37 Haslinger, J. and Neittaanmaki, P., ***Finite Element Approximation for Optimal Shape Design: Theory and Applications***, John Wiley & Sons, New York, 1988.

38 Haug, E.J., Choi, K.K. and Komkov, V., ***Design Sensitivity Analysis of Structural Systems***, Academic Press, New York, 1986.

39 Hinton, E. and Campbell, J., "Local and Global Smoothing of Discontinuous Finite Element Functions Using a Least Square Method," *Int. J. Numer. Methods Eng.*, Vol. 9, 461-480 (1976).

40 Imam, M.H, "Three-Dimensional Shape Optimization," *Int. J. Numer. Methods Eng.*, Vol. 18, 661-673 (1982).

41 Kikuchi, N. and Tezuka, A., "Adaptive Finite Element Method and Its Applications," in ***Geometry and Optimization Techniques for Structural Design***, Edited by S. Kodiyalam and M. Saxena, Computational Mechanics Publications and Elsevier Applied Science, New York, 1994.

42 Kodiyalam, S. and Vanderplaats, G.N., "Shape Optimization of 3D Continuum Structures Via Force Approximation Technique", AIAA *J.*, Vol. 27(9), 1256-1263 (1989).

43 Kodiyalam, S., Kumar, V. and Finnigan, P.M., "Constructive Solid Geometry Approach to Three-Dimensional Structural Shape Optimization", AIAA *J.*, Vol. 30(5), 1408-1415 (1992).

44 Kodiyalam, S., "Structural Shape Optimization", in ***Geometry and Optimization Techniques for Structural Design***, Edited by S. Kodiyalam and M. Saxena, Computational Mechanics Publications and Elsevier Applied Science, New York, 1994.

45 Kohn, R.V. and Strang, G., "Optimal Design and Relaxation of Variational Problems", *Comm. Pure Appl. Math.*, Vol. 39, 113-137 (Part I), 139-182 (Part II), 353-377 (Part III) (1988).

46 Kondo, S., "Lateral Buckling of a Cantilever Beam as a Problem in Plate Theory," *Proc. 5^{th} Japan National Congress for Appl. Mech.*, 143-145(1955)

47 Krige, D.G., "A Statistical Approach to Some Basic Mine Valuation Problems on the Wit Water Rand", *J. Chem. Metal. Min. Soc. S. Afr.*, Vol. S2, 119-139 (1951).

48 Kristensen, E.S. and Madsen, N.F., "On the Optimal Shape of Fillets in Plates Subjected to Multiple In-Plane Loading Cases", *Int. J. Numer. Methods Eng.*, Vol. 10, 1007-1019 (1976).

49 Lee, N. and Bathe, K., "Effects of Element Distortions on the Performance of Isoparametric Elements," *Int. J. Numer. Methods Eng.*, Vol. 36, 3553-3576 (1993).

50 Limaiem, A and El Maraghy, H.A., "Analytical Solid Modeling Using Dual Kriging", *Advances in Design Automation*, Vol. 1, 127-132 (1995).

51 MacNeal, R.H., ***Finite Elements: Their Design and Performance***, Marcel Dekker, New York, 1994.

52 Matheron, G., ***Splines et Krigeage: Leur Equivalence Formelle***, Note Interne, COMM, Fontainebleau, France, 1980.

53 Mindlin, R.D., "Influence of Rotary Inertia and Shear in Flexural Motion of Isotropic, Elastic Plates," ASME *Journal of Applied Mechanics*, Vol. 18, 31-38(1951).

54 Montes, P., "Kriging Interpolation of a Bezier Curve", *Computer-Aided Design*, Vol. 23, No. 10, 713-716 (1991)

55 Mota Soares, C.A., ***Computer Aided Structural Design: Structural and Mechanical Systems***, Springer-Verlag, New York, 1987.

56 Naqib, R.A., Zureick, A. and Will, K.M., "New Approximate-Iterative Technique in Shape Optimization of Continuum Structures", *Comput. Struct.*, Vol. 51, 737-748 (1994).

57 Olhoff, N., Rasmussen, J. and Lund, E., "A Method of Numerical Differentiation for Error Elimination in Finite-Difference-Based Semi-Analytical Shape Sensitivity Analyses," *Mech. Struct. Mach.*, Vol. 21(1), 1-66 (1993).

58 Prager, W., "Conditions for Optimality," *Comput. Struct.*, Vol. 2, 833-840 (1972).

59 Rajan, S.D. and Belegundu, A.D., "Shape Optimal Design Using Fictitous Loads," AIAA *J.*, Vol. 27(1), 102-107 (1989).

60 Rao, S.S., Pan, T. and Venkayya, V.B., " Optimal Placement of Actuators in Actively Controlled Structures Using Genetic Algorithms," AIAA *J.*, Vol. 29(6), 942--943 (1991).

61 Reissner, E. "Lateral Buckling of Beams," *Comput. Struct.*, Vol. 33, 1289-1306(1989).

62 Reissner, E. "The Problem of Lateral Buckling of Plates," *Z. Angew. Math. Mech.*, Vol. 75, 615-621(1995).

63 Rogers, D.F. and Adams, J.A., ***Mathematical Elements for Computer Graphics***, 3rd Edition, McGraw-Hill, New York, 1985.

64 Saxena, M., "Recent Advances in Automatic Mesh Generation for Structural Domains", ***in Geometry and Optimization Techniques for Structural Design***, Edited by S. Kodiyalam and M. Saxena, Computational Mechanics Publications and Elsevier Applied Science, New York, 1994.

65 Schmit, L.A., "Structural Synthesis – Its Genesis and Development," AIAA *J.*, Vol. 19, 1249-1263 (1981).

66 Schramm, U. and Pilkey, W.D., "Optimal Shape Design for Thin-Walled Beam Cross-Sections," *Int. J. Numer. Methods Eng.*, Vol. 37, 4039-4058 (1994).

67 Shu, C., and Osher, S., "Efficient Implementation of Essentially Non-Oscillatory Shock-Capturing Schemes", *J. Comput. Physics*, Vol. 77, 439-471 (1988).

68 Svinivas, S. and Rao, A.K., "Buckling of Thick Rectangular Plates," AIAA *J.*, Vol. 7, 1645-1646 (1969).

69 Theodoracatos, V.E. and Bobba, V., "NURBS Surface Reconstruction from a Large Set of Image and World Data Points", *Advances in Design Automation*, Vol. 2, 15-33 (1993)

70 Timoshenko, S.P. and Woinowsky-Krieger, S., ***Theory of Plates and Shells***, 2nd Ed., McGraw-Hill, New York (1959).

71 Timoshenko, S.P. and Gere, J.M., ***Theory of Elastic Stability***, McGraw-Hill, 2nd Ed., New York, 1961.

72 Tseng, C.H. and Arora, J.S., "On Implementation of Computational Algorithms for Optimal Design 1: Preliminary Investigation," *Int. J. Numer. Methods Eng.*, Vol. 26, 1365-1382 (1988).

73 Tseng, C.H. and Arora, J.S., "On Implementation of Computational Algorithms for Optimal Design 2: Extensive Numerical Investigation," *Int. J. Numer. Methods Eng.*, Vol. 26, 1383-1402 (1988).

74 Vanderplaats, G.N., "CONMIN-A FORTRAN Program for Constrained Function Minimization," NASA TM X-62282 (1973).

75 Vanderplaats, G.N., ***Numerical Optimization Techniques for Engineering Design with Applications***, McGraw-Hill, New York, 1984.

76 Vanderplaats, G.N. and Salajegheh, E., "A New Approximation Method for Stress Constraints in Structural Synthesis," AIAA *J.*, Vol. 27, No.3, 352-358 (1989).

77 Venkayya, V.B., "Structural Optimization Using Optimality Criteria: A Review and Some Recommendations," *Int. J. Numer. Methods Eng.*, Vol. 13, 203-228 (1978).

78 Venugopal, N., Venkateswara Rao, G., and Shastry, B.P., "Lateral Stability of Cantilever Beams Subjected to Concentrated or Uniformly Distributed Loads," *Comput. Struct.*, Vol. 29, 351-352(1988)

79 Wang, B.P., "Improved Approximate Methods for Computing Eigenvector Derivatives in Structural Dynamics," AIAA *J.*, Vol. 29(6), 1018-1020 (1991).

80 Watson, G.S., "Smoothing and Interpolation by Kriging and with Splines," *J. Int. Assoc. Math. Geol.*, Vol. 16(6), 601-616 (1984)

81 Wilkinson, J.H., ***The Algebraic Eigenvalue Problem***, Clarendon Press, Oxford, 1965.

82 Yamazaki, K., "Design Sensitivity Analysis in Structural Optimization," in ***Geometry and Optimization Techniques for Structural Design***, Edited by S. Kodiyalam and M. Saxena, Computational Mechanics Publications and Elsevier Applied Science, New York, 1994.

83 Yang, R.J. and Botkin, M.E., "Comparison Between the Variational and Implicit Differentiation Approaches to Shape Design Sensitivities," AIAA *J.*, Vol. 24, 1027-1032 (1986).

84 Zhao, Z., ***Shape Design Sensitivity Analysis and Optimization Using the Boundary Element Method***, Lecture Notes in Engineering, Vol. 62, Spring-Verlag, New York, 1991.

85 Zhu, J.Z. and Zienkiewicz, O.C., "Superconvergence Recovery Techniques and A Posteriori Error Estimators," *Int. J. Numer. Methods. Eng.*, Vol. 30, 1321-1339 (1990).

86 Zienkiewicz, O.C. and Campbell, J.S., "Shape Optimization and Sequential Linear Programming," in ***Optimal Structure Design***, Edited by R.H. Gallagher and O.C. Zienkiewicz, John Wiley & Sons, New York, 1973.

87 Zienkiewicz, O.C. and Taylor, R.L., ***The Finite Element Method***, Vol. 1, 4th Ed., McGraw-Hill, New York, 1989.

88 Zienkiewicz, O.C., Taylor, R.L., Papdopoulos, P. And Onate, P., "Plate Bending Element with Discrete Constraints: New Triangular Elements," *Comput. Struct.*, Vol. 35, 505-522 (1990).

89 Zienkiewicz, O.C. and Zhu, J.Z., "Adaptivity and Mesh Generation," *Int. J. Numer. Methods Eng.*, Vol. 32, 783-810 (1991).

90 Zienkiewicz, O.C. and Taylor, R.L., ***The Finite Element Method***, Vol. 2, 4th Ed., McGraw-Hill, New York, 1992.

91 Zienkiewicz, O.C. and Zhu, J.Z., "Superconvergent Patch Recovery Techniques and Adaptive Finite Element Refinement," *Comp. Meth. Appl. Meth. Eng.*, Vol. 101, 207-224 (1992).

92 Zoutendijk, G., ***Methods of Feasible Directions,*** Elsevier, Amsterdam, 1960.

APPENDICES

A REVIEW OF FINITE ELEMENT ANALYSIS

In this appendix, we begin with highlighting the general procedure used in deriving a FE formulation. This will be followed by two sections in which two specific FE formulations are developed for both planar and plate structures. A validation section is presented at last.

A.1 General

The solution procedure in a displacement-based finite element (FE) modeling for an elastic structure can be divided into the following eight steps:

1) discretizing the continuum into a finite number of elements;
2) representing the displacement field of an element by its nodal displacements;
3) expressing the internal stress and strain in terms of the nodal displacements via the strain-displacement equations and the constitutive relationships;
4) forming the element-level FE equation for each element;
5) assembling the obtained elemental FE equations into the global FE equations;
6) applying the boundary conditions to obtain the reduced global equations;
7) solving the resulting equations for the nodal displacements; and finally
8) recovering the strains, the stresses, and the reaction forces if desirable.

By applying steps 1) to 6), a structural FE analysis can be based on the solution $\{u\}$ of the following linear system of equations

$$[K]\{u\}=\{f\} \tag{A.1}$$

where $[K]$, $\{u\}$, and $\{f\}$ are the global stiffness matrix, the nodal displacement and the equivalent force vectors for the FE representation, respectively. To be more specific, it is assumed that the total number of the degrees of freedom (DOFs) is M, so that the preceding stiffness matrix and vectors are of M dimensions. The foregoing equations reflect an equilibrium state for a whole structure. It is assembled from NE equilibrium equations that are established by considering each element and the essential boundary conditions.

Only an outline of the FE formulations for planar and flat plate structures is presented in the following sections. More details of FE theory and applications can be found in a number of excellent textbooks. [e.g., 8, 87, 90]

A.2 Planar Structural Formulation

A.2.1 FE formulation

It is known that an elemental stiffness matrix for a single element in an elastic structure can be expressed as

$$[K]_e = \int_{\Omega_e} [B]^T [C][B] d\Omega_e \tag{A.2}$$

where Ω_e is the physical domain of the e-th element, $[B]$ and $[C]$ are the strain-displacement and the stress-strain matrices. The elemental stiffness matrix for a two-dimensional isoparametric element can be derived easily. Let the element shape and displacement functions be expressed by

$$x(\xi,\eta)=\sum_{j=1}^{\tilde{N}} N_j(\xi,\eta)\,x_j$$
$$y(\xi,\eta)=\sum_{j=1}^{\tilde{N}} N_j(\xi,\eta)\,y_j \tag{A.3}$$

and

$$u(\xi,\eta)=\sum_{j=1}^{\tilde{N}} N_j(\xi,\eta)\,u_j$$
$$v(\xi,\eta)=\sum_{j=1}^{\tilde{N}} N_j(\xi,\eta)\,v_j \tag{A.4}$$

where the pairs (x_j, y_j) and (u_j, v_j) represent the coordinates and the displacements at local node j of the element. The integer $\tilde{N}$ denotes the number of nodal points in the element and $N_j(\xi,\eta)$ is the shape function associated with node j under the isoparametric coordinates (ξ,η).

It should be mentioned that two convenient coordinate systems have generally been utilized in illustrating a triangular isoparametric element, the area coordinates and the unit coordinates, as shown schematically in Figure A.1. However, only the unit triangular coordinate approach was used in the FE module because it was felt this approach is more analogous to quadrilateral isoparametric element description.

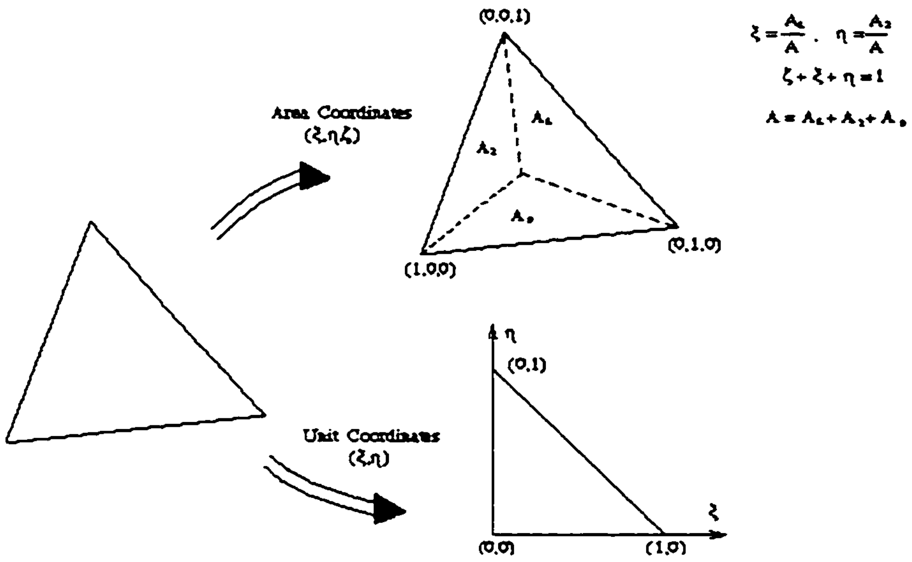

Figure A.1:·Two coordinates used to illustrate a triangular parametric element

For either a quadrilateral or a triangular isoparametric element, an entity of the stiffness matrix $[K]_e$ can now be expressed by

$$K_{ij}^{e} = h\int_{\eta_1}^{\eta_2}\int_{\xi_1}^{\xi_2} [B_i]^T[C][B_j]\left|[J]\right| \, d\xi \, d\eta \tag{A.5}$$

where h represents the element thickness that is here assumed to be uniform for easy presentation. The integration limits have values of

$$\xi_0 = 0, \xi_1 = 1-\eta$$
$$\eta_0 = 0, \eta_1 = +1$$

for a triangular element and

$$\xi_0 = -1, \xi_1 = +1$$
$$\eta_0 = -1, \eta_1 = +1$$

for a quadrilateral element. $[B_i]$ denotes the i-th block column of the strain-displacement matrix $[B]$ in the form

$$[B] = \lfloor [B_1], [B_2], \cdots, [B_{\tilde{N}}] \rfloor$$

$$[B_i] = \begin{bmatrix} N_{i,x} & 0 \\ 0 & N_{i,y} \\ N_{i,y} & N_{i,x} \end{bmatrix} \tag{A.6}$$

$$(1 \le i \le \tilde{N})$$

The strain-displacement relations are translated into

$$\{\xi\} = \lfloor \xi_x, \xi_{yy}, \gamma_{xy} \rfloor^T = [B]\{u\}^e \tag{A.7}$$

with the elemental displacement vector being specified by

$$\{u\}^e = \lfloor u_1^e, v_1^e, u_2^e, v_2^e, \cdots, u_N^e, v_N^e \rfloor^T \tag{A.8}$$

The matrix $[J]$ is the transformation Jacobian between two coordinates (x, y) and (ξ, η) defined by

$$[J] = \begin{bmatrix} \dfrac{\partial x}{\partial \xi} & \dfrac{\partial y}{\partial \xi} \\ \dfrac{\partial x}{\partial \eta} & \dfrac{\partial y}{\partial \eta} \end{bmatrix} \tag{A.9}$$

which can also be expressed explicitly in terms of nodal point coordinates (x_j, y_j) and shape functions as follows

$$[J] = \begin{bmatrix} N_{1,\xi} & N_{2,\xi} & \cdots & N_{\tilde{N},\xi} \\ N_{1,\eta} & N_{2,\eta} & \cdots & N_{\tilde{N},\eta} \end{bmatrix} \begin{bmatrix} x_1 & y_1 \\ x_2 & y_2 \\ \vdots & \vdots \\ x_{\tilde{N}} & y_{\tilde{N}} \end{bmatrix} \tag{A.10}$$

It is further noted that the following useful derivative relation holds for shape functions

$$[N_{i,x} \quad N_{i,y}]^T = [J]^{-1}[N_{i,\xi} \quad N_{i,\eta}]^T \qquad (1 \le i \le \tilde{N}) \tag{A.11}$$

and

$$\begin{bmatrix} N_{1,x} & N_{2,x} & \cdots & N_{\tilde{N},x} \\ N_{1,y} & N_{2,y} & \cdots & N_{\tilde{N},y} \end{bmatrix} = [J]^{-1} \begin{bmatrix} N_{1,\xi} & N_{2,\xi} & \cdots & N_{\tilde{N},\xi} \\ N_{1,\eta} & N_{2,\eta} & \cdots & N_{\tilde{N},\eta} \end{bmatrix} \tag{A.12}$$

Concentrated (point) and/or distributed (traction force) loads are incorporated into the linear system of equations through the shape functions. For example, in the distributed loading (or traction force) case, the components of the elemental force vector for the e-th element in the work equivalent form can be assembled from each of the element edges directly loaded by traction forces. For such an edge, the work equivalent force can be expressed by

$$f_{x,i} = h \int_{-1}^{+1} p_x N_i \left| [J_s] \right| d\xi,$$

$$f_{y,i} = h \int_{-1}^{+1} p_y N_i \left| [J_s] \right| d\xi, \tag{A.13}$$

$$(1 \le i \le \tilde{N}_e)$$

where p_x and p_y represent the distributed loading intensities in the x- and y-direction. The integer $\tilde{N}_e$ denotes the number of nodal points on the considered edge. $[J_s]$ denotes the Jacobian transformation matrix on the edge and its determinant is given by

$$|[J_s]| = \sqrt{\left(\frac{\partial x}{\partial \xi}\right)^2 + \left(\frac{\partial y}{\partial \xi}\right)^2} \tag{A.14}$$

with

$$\begin{aligned} x(\xi) &= \sum_{j=1}^{\tilde{N}_e} N_j(\xi) x_j \\ y(\xi) &= \sum_{j=1}^{\tilde{N}_e} N_j(\xi) y_j \end{aligned} \tag{A.15}$$

which give the isoparametric representation of an edge connected by $\tilde{N}_e$ nodes.

Figure A.2 may be used to aim to understand the notation. This configuration illustrates a three-node triangular boundary element loaded on one of the edges. Here, $\tilde{N}_e = 2$ and $\tilde{N} = 3$. The corresponding elemental displacement vector reduces to

$$\{u\}^e = \{u_1^e, u_2^e, u_3^e, v_1^e, v_2^e, v_3^e\}^T \tag{A.16}$$

and the force vector is expressed as

$$\{f\}^e = \{f_{x,1}^e, f_{y,1}^e, f_{x,2}^e, f_{y,2}^e, 0, 0\}^T \tag{A.17}$$

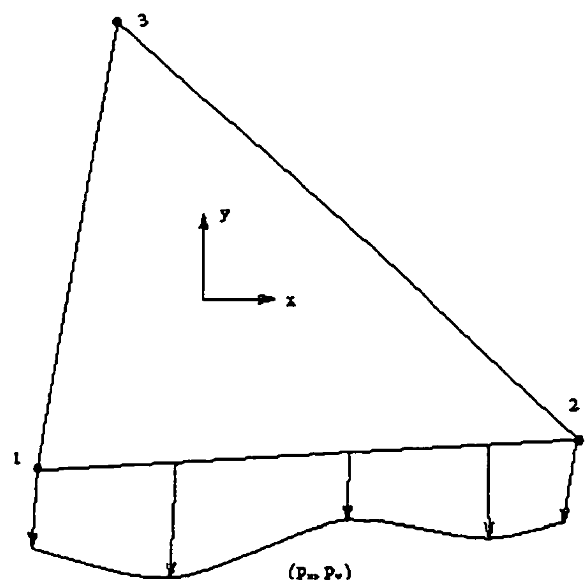

Figure A.2: Distributed load on a three-node triangular element

Only quadratic triangular and quadrilateral elements are employed in this study, as shown in Figure A.3(a)-(c). For planar structural applications, nine and four integration points (or Gaussian quadrature points) are used to numerical calculate the elemental stiffness matrices for a quadrilateral element and a triangular element, respectively. Correspondingly, the numbers of the stress recovery points (Barlow points, which turn out to be optimal stress recovery points) are set to be four and three depending on the type of element. A summary of these Barlow points is given in Table A.1. The developed finite element solver employs the dynamic storage allocation technique, which followed the approach taken by Akin [2]. The stiffness matrix is stored in the band form and Sloan's bandwidth optimization procedure is employed to reduce the bandwidth and to increase solver's efficiency.

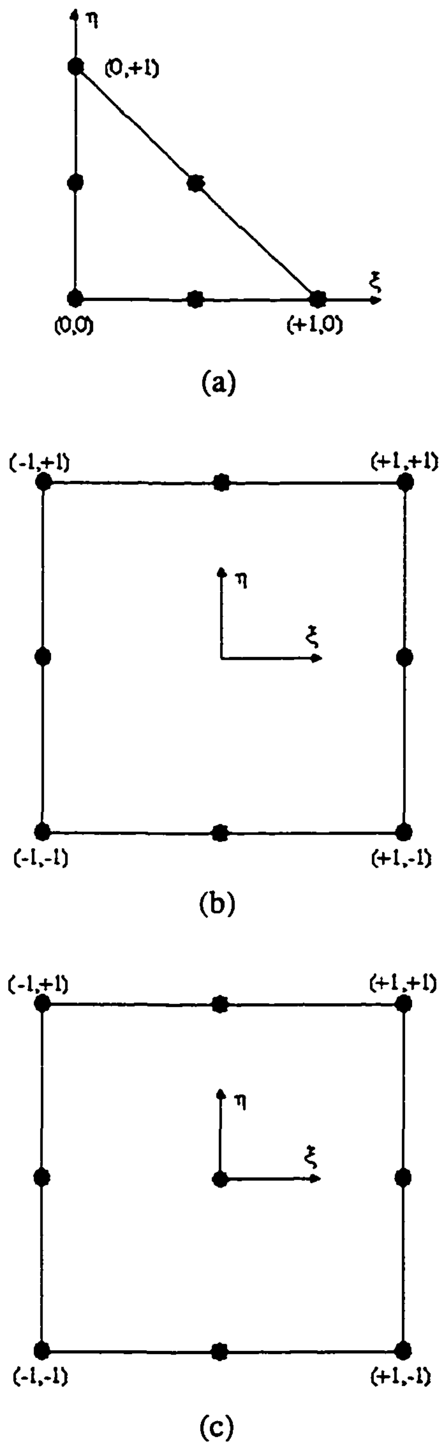

Figure A.3: A quadratic (a) triangular; (b) 8-node; (c) 9-node quadrilateral element

It should be pointed out that Table A.1 reveals one special aspect related to a quadratic triangular element: these are two different versions of three Barlow points. A more serious problem is that there is very limited information available about their comparative performance. Unless stated otherwise, the edge scheme will be used in the package for the stress recovery.

Element Shape	Optimal integration points $(\xi,\eta)_i$ and weights w_i in forming stiffness matrix	Optimal integration points $(\xi,\eta)_i$ and weights w_i in stress recovery
Quadrilateral	$(\xi,\eta)_1=\left(-\sqrt{0.6},-\sqrt{0.6}\right)\ w_1=\left(\frac{5}{9}\right)^2$ $(\xi,\eta)_2=\left(-\sqrt{0.6},0\right)\ w_2=\left(\frac{5}{9}\right)\left(\frac{8}{9}\right)$ $(\xi,\eta)_3=\left(-\sqrt{0.6},+\sqrt{0.6}\right)\ w_3=\left(\frac{5}{9}\right)^2$ $(\xi,\eta)_4=\left(0,-\sqrt{0.6}\right)\ w_4=\left(\frac{5}{9}\right)\left(\frac{8}{9}\right)$ $(\xi,\eta)_5=(0,0),\ w_5=\left(\frac{8}{9}\right)^2$ $(\xi,\eta)_6=\left(0,+\sqrt{0.6}\right)\ w_{61}=\left(\frac{5}{9}\right)\left(\frac{8}{9}\right)$ $(\xi,\eta)_7=\left(+\sqrt{0.6},-\sqrt{0.6}\right)\ w_7=\left(\frac{5}{9}\right)^2$ $(\xi,\eta)_8=\left(+\sqrt{0.6},0\right)\ w_8=\left(\frac{5}{9}\right)\left(\frac{8}{9}\right)$ $(\xi,\eta)_9=\left(+\sqrt{0.6},+\sqrt{0.6}\right)\ w_9=\left(\frac{5}{9}\right)^2$	$(\xi,\eta)_1=\left(-\frac{1}{\sqrt{3}},-\frac{1}{\sqrt{3}}\right),\ w_1=1$ $(\xi,\eta)_2=\left(-\frac{1}{\sqrt{3}},+\frac{1}{\sqrt{3}}\right),\ w_2=1$ $(\xi,\eta)_3=\left(+\frac{1}{\sqrt{3}},-\frac{1}{\sqrt{3}}\right),\ w_3=1$ $(\xi,\eta)_4=\left(+\frac{1}{\sqrt{3}},+\frac{1}{\sqrt{3}}\right),\ w_4=1$
Triangular	$(\xi,\eta)_1=\left(\frac{1}{3},\frac{1}{3}\right),\ w_1=-\frac{9}{32}$ $(\xi,\eta)_2=\left(\frac{3}{5},\frac{1}{5}\right),\ w_2=\frac{25}{96}$ $(\xi,\eta)_3=\left(\frac{1}{5},\frac{3}{5}\right),\ w_3=\frac{25}{96}$ $(\xi,\eta)_4=\left(\frac{1}{5},\frac{1}{5}\right),\ w_4=\frac{25}{96}$	Edge scheme: $(\xi,\eta)_1=\left(0,\frac{1}{2}\right),\ w_1=\frac{1}{6}$ $(\xi,\eta)_2=\left(\frac{1}{2},0\right),\ w_2=\frac{1}{6}$ $(\xi,\eta)_3=\left(\frac{1}{2},\frac{1}{2}\right),\ w_3=\frac{1}{6}$ Interior scheme: $(\xi,\eta)_1=\left(\frac{1}{6},\frac{2}{3}\right),\ w_1=\frac{1}{6}$ $(\xi,\eta)_2=\left(\frac{1}{6},\frac{1}{6}\right),\ w_2=\frac{1}{6}$ $(\xi,\eta)_3=\left(\frac{2}{3},\frac{1}{6}\right),\ w_3=\frac{1}{6}$

Table A.1: Optimal integration points and weights for quadratic elements

A.2.2 Validation Example

The model used to verify the FE module of the package is a classic one: a thin 80 units by 80 units square plate with a centered circular hole of 10 units diameter. The plate is under unit uniaxial tensile traction in the x-direction. Its quarter model, taking advantage of structural symmetry, is shown in Figure A.4

The theoretical stress solutions are available in classic elasticity books and their values along the x- and y-axes can be expressed by

$$\sigma_{xx} = \frac{1}{2}\left[2 - 5\left(\frac{r}{x}\right)^2 + 3\left(\frac{r}{x}\right)^4\right]$$
$$\sigma_{yy} = \frac{1}{2}\left[\left(\frac{r}{x}\right)^2 - 3\left(\frac{r}{x}\right)^4\right] \qquad \text{(A.18)}$$

along the x-axis and

$$\sigma_{xx} = \frac{1}{2}\left[2 - 5\left(\frac{r}{x}\right)^2 + 3\left(\frac{r}{x}\right)^4\right]$$
$$\sigma_{yy} = \frac{1}{2}\left[\left(\frac{r}{x}\right)^2 - 3\left(\frac{r}{x}\right)^4\right] \qquad \text{(A.19)}$$

along the y-axis, where $r = 5$ is the hole radius and both x and y take values from 5 to 40. The triangular mesh is depicted in Figure A.5. A comparison of theoretical and the FE solutions is shown in Figure A.6(a) and (b). As can be seen, the approximate stress results agree well with the theoretical solutions.

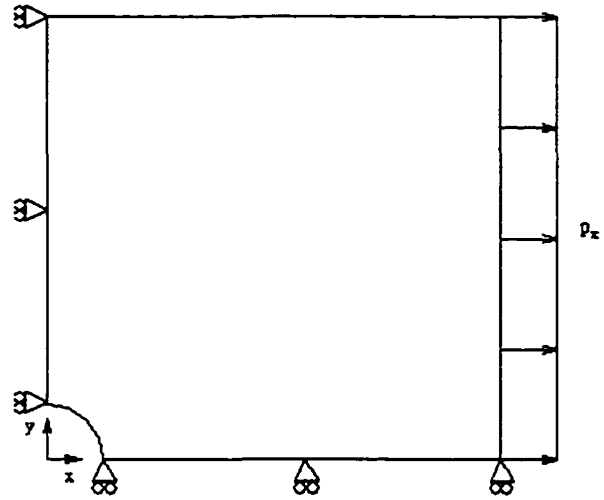

Figure A.4: Model of a plate with a circular hole

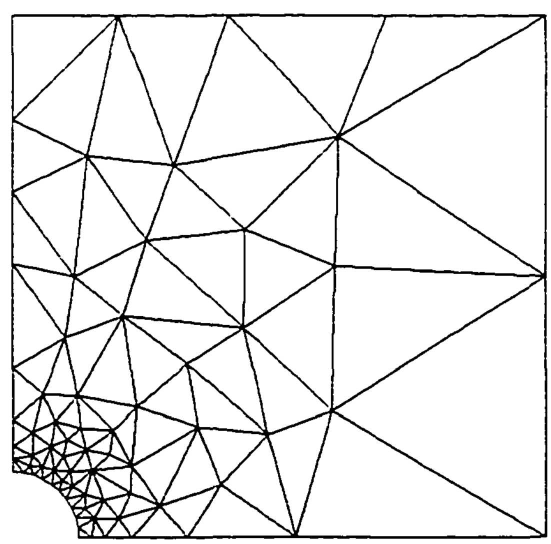

Figure A.5: Mesh of a plate with a circular hole

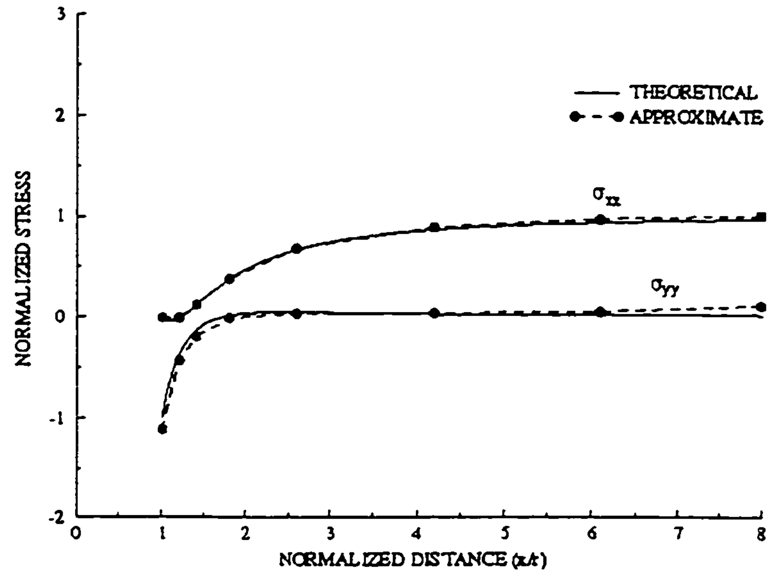

(a)

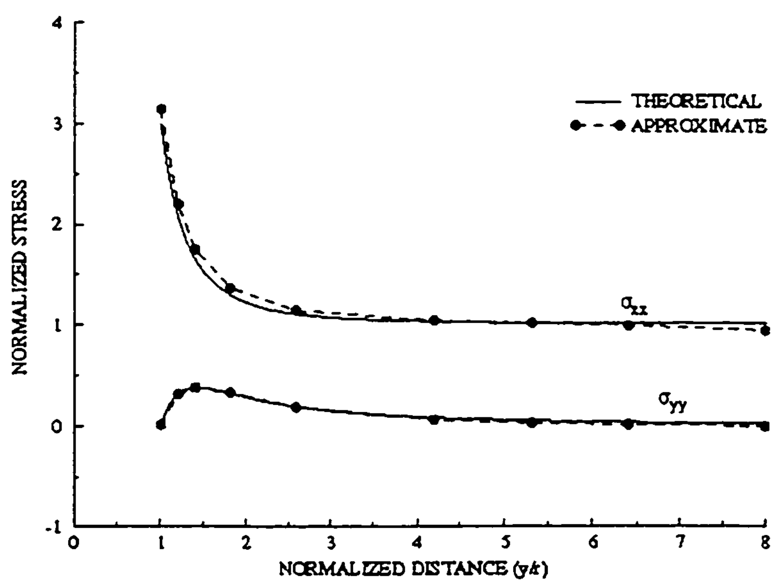

(b)

Figure A.6: Comparison of theoretical and approximate normal stresses (a) along x-axis; (b) along y-axis

A.3 Reissner-Mindlin Plate Theory and Its FE Development

A.3.1 Plate Theory and Energy Forms

According to the Reissner-Mindlin plate theory, without considering the mid-plane stretching, the displacement field of a plate structure, as shown schematically in Figure A.7, can be described by

$$\begin{aligned} u(x,y,z,t) &= z\theta_x(x,y,t) \\ v(x,y,z,t) &= z\theta_y(x,y,t) \\ w(x,y,z,t) &= w_0(x,y,t) \end{aligned} \tag{A.20}$$

where $\theta_x(x,y,t)$ and $\theta_y(x,y,t)$ represent rotations of the mid-plane normals along the x and the y axes, respectively, during the deformation, and $w_0(x,y,t)$ represents the displacement of the mid-plane in the z axis direction.

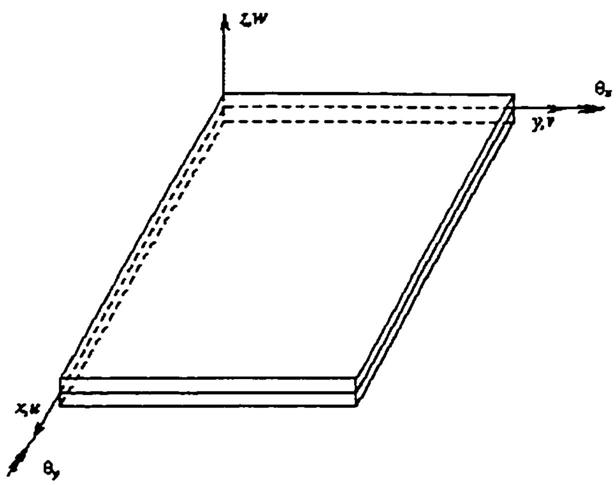

Figure A.7: Reissner-Mindlin plate notation

Various sources (e.g. [90]) can be consulted for details of this plate theory. For our current presentation, an expression of the total potential energy, U, is required. It can be shown that this quantity can be expressed as

$$U = \frac{1}{2}\int_A \left(\begin{Bmatrix} \theta_{x,x} \\ \theta_{y,y} \\ \theta_{x,y} + \theta_{y,x} \end{Bmatrix}^T [C_b] \begin{Bmatrix} \theta_{x,x} \\ \theta_{y,y} \\ \theta_{x,y} + \theta_{y,x} \end{Bmatrix} + \begin{Bmatrix} \theta_x + w_{0,x} \\ \theta_y + w_{0,y} \end{Bmatrix}^T [C_s] \begin{Bmatrix} \theta_x + w_{0,x} \\ \theta_y + w_{0,y} \end{Bmatrix} \right) dA -$$

$$\frac{1}{2}\int_A \left(\begin{Bmatrix} \theta_{x,x} \\ \theta_{x,y} \end{Bmatrix}^T \left[\frac{h^2}{12}\Sigma_0\right] \begin{Bmatrix} \theta_{x,x} \\ \theta_{x,y} \end{Bmatrix} + \begin{Bmatrix} \theta_{y,x} \\ \theta_{y,y} \end{Bmatrix}^T \left[\frac{h^2}{12}\Sigma_0\right] \begin{Bmatrix} \theta_{y,x} \\ \theta_{y,y} \end{Bmatrix} + \begin{Bmatrix} w_{0,x} \\ w_{0,y} \end{Bmatrix}^T [h\Sigma_0] \begin{Bmatrix} w_{0,x} \\ w_{0,y} \end{Bmatrix} \right) dA \tag{A.21}$$

A comma indicates partial differentiation with respect to the subscript following the comma; h is the plate thickness, and

$$[C_b] = D \begin{bmatrix} 1 & \nu & 0 \\ \nu & 1 & 0 \\ 0 & 0 & \frac{1-\nu}{2} \end{bmatrix}$$

$$[C_s] = \frac{\kappa E h}{2(1+\nu)} \begin{bmatrix} 1 & 0 \\ 0 & 1 \end{bmatrix} \tag{A.22}$$

where $D = Eh^2/[12(1-\nu^2)]$ denotes the flexural rigidity of the plate. The constant κ denotes the shear correction factor that is usually approximated for a rectangular cross section by 5/6 as proposed by Reissner [90]. The second term in Equation (A.21) containing the initial in-plane stress matrix

$$[\Sigma_0] = \lambda \begin{bmatrix} \sigma_x^0 & \sigma_{xy}^0 \\ \sigma_{xy}^0 & \sigma_y^0 \end{bmatrix} \tag{A.23}$$

represents the potential energy of these stresses acting on the nonlinear parts of the displacement-strain relations. The physical meaning of the scalar parameter λ will be discussed later.

A.3.2 Isoparametric Plate Element Formulation

The whole plate structure is now partitioned into finite elements. The potential energy in each element is then calculated and summed to yield the total potential energy. The minimum principle of the potential energy is used to formulate an eigenvalue problem. For an isoparametric element, recalling that $\tilde{N}$ denotes the number of nodal points associated with the element, then coordinates of the points in the element and the displacement field can be represented by

$$\begin{Bmatrix} w \\ \theta_x \\ \theta_y \end{Bmatrix} = \sum_{i=1}^{\tilde{N}} \begin{bmatrix} N_i(\xi,\eta) & 0 & 0 \\ 0 & N_i(\xi,\eta) & 0 \\ 0 & 0 & N_i(\xi,\eta) \end{bmatrix} \{q_i\} \tag{A.24}$$

where $\{q_i\} = \{w_i, \theta_{xi}, \theta_{yi}\}^T$ represents the corresponding displacement vector. With these transformations, the vectors in Equation (A.21) can be cast as

$$w_0 = \sum_{i=1}^{\tilde{N}} \{W_i\}^T \{q_i\} = \sum_{i=1}^{\tilde{N}} \begin{Bmatrix} N_i \\ 0 \\ 0 \end{Bmatrix}^T \{q_i\}$$

$$\begin{Bmatrix} \theta_x \\ \theta_y \end{Bmatrix} = \sum_{i=1}^{\tilde{N}} [\Theta_i]\{q_i\} = \sum_{i=1}^{\tilde{N}} \begin{bmatrix} 0 & N_i & 0 \\ 0 & 0 & N_i \end{bmatrix} \{q_i\} \tag{A.25}$$

$$\begin{Bmatrix} w_{0,x} \\ w_{0,y} \end{Bmatrix} = \sum_{i=1}^{\tilde{N}} [G_{wi}]\{q_i\} = \sum_{i=1}^{\tilde{N}} \begin{bmatrix} N_{i,x} & 0 & 0 \\ N_{i,y} & 0 & 0 \end{bmatrix} \{q_i\}$$

$$\begin{Bmatrix} \theta_{x,x} \\ \theta_{x,y} \end{Bmatrix} = \sum_{i=1}^{\tilde{N}} [G_{\beta_x i}]\{q_i\} = \sum_{i=1}^{\tilde{N}} \begin{bmatrix} 0 & N_{i,x} & 0 \\ 0 & N_{i,y} & 0 \end{bmatrix} \{q_i\} \tag{A.26}$$

$$\begin{Bmatrix} \theta_{y,x} \\ \theta_{y,y} \end{Bmatrix} = \sum_{i=1}^{\tilde{N}} [G_{\theta_y i}]\{q_i\} = \sum_{i=1}^{\tilde{N}} \begin{bmatrix} 0 & 0 & N_{i,x} \\ 0 & 0 & N_{i,y} \end{bmatrix} \{q_i\}$$

and

$$\begin{Bmatrix} \theta_{x,x} \\ \theta_{y,y} \\ \theta_{x,y} + \theta_{y,x} \end{Bmatrix} = \sum_{i=1}^{\tilde{N}} [B_{bi}]\{q_i\} = \sum_{i=1}^{\tilde{N}} \begin{bmatrix} 0 & N_{i,x} & 0 \\ 0 & 0 & N_{i,y} \\ 0 & N_{i,y} & N_{i,x} \end{bmatrix} \{q_i\}$$

$$\begin{Bmatrix} \theta_x + w_{0,x} \\ \theta_y + w_{0,y} \end{Bmatrix} = \sum_{i=1}^{\tilde{N}} [B_{si}]\{q_i\} = \sum_{i=1}^{\tilde{N}} \begin{bmatrix} N_{i,x} & N_i & 0 \\ N_{i,y} & 0 & N_i \end{bmatrix} \{q_i\} \tag{A.27}$$

The derivatives of shape functions with respect to x and y were worked out previously. Upon substituting Equations (A.25-27) into Equation (A.21), one can express the total potential energy in a single element as

$$U^e = \frac{1}{2} \sum_{i,j=1}^{\tilde{N}} \{q_i\}^T [K^e] \{q_j\} - \frac{1}{2} \sum_{i,j=1}^{\tilde{N}} \{q_i\}^T [K_G^e] \{q_j\} \tag{A.28}$$

where the entities in the matrices can be expressed as

$$K_{ij}^{e} = \int_{-1}^{1}\int_{-1}^{1} \left([B_{bi}]^T [C_b][B_{bi}] + [B_{si}]^T [C_s][B_{si}] \right) \|[J]\| \, d\xi \, d\eta$$

$$K_{Gij}^{e} = \int_{-1}^{1}\int_{-1}^{1} \begin{bmatrix} \frac{h^2}{12}\left([G_{\theta_x i}]^T [\Sigma_0][G_{\theta_x i}] + [G_{\theta_y i}]^T [\Sigma_0][G_{\theta_y i}] \right) + \\ h[G_{wi}]^T [\Sigma_0][G_{wi}] \end{bmatrix} \|[J]\| \, d\xi \, d\eta \qquad \text{(A.29)}$$

$$(1 \le i, j \le \tilde{N})$$

Summing up the total potential energy contributed from each element and applying the principle of minimum potential energy leads to the following eigenproblem

$$([K] - \lambda [K_G])\{q\} = \{0\} \qquad \text{(A.30)}$$

The matrices $[K]$ and $[K_G]$ are referred to as the global stiffness and the geometric (or initial-stress) matrices, respectively, and

$$\{q\} = \left\{ \{q_1\}^T, \{q_2\}^T, \cdots, \{q_{\mathrm{DOF}}\}^T \right\}^T \qquad \text{(A.31)}$$

where the subscript DOF denotes the number of degrees of freedom. Physically, Equation (A.30) implies that, in a linear buckling analysis, if the in-plane stresses induced by an in-plane loading condition are varied by a factor λ, the geometric stiffness should be changed proportionately. When nonpositivity occurs in the sum of the geometric stiffness and flexural stiffness, the in-plane load is referred to as the buckling load.

It is worth mentioning that in general the initial-stress terms arise from the given in-plane forces per unit length or width N_{0x}, N_{0y} and N_{0xy}. Consequently, the initial–stress matrix becomes

$$[\Sigma_0] = \frac{\lambda}{h}\begin{bmatrix} N_{ox} & N_{oxy} \\ N_{oxy} & N_{oy} \end{bmatrix} \tag{A.32}$$

Furthermore, it can be shown that

$$\left[K^e_{Gij}\right] = \int_{-1}^{1}\int_{-1}^{1} \begin{bmatrix} \Delta_{ij} & 0 & 0 \\ 0 & \dfrac{h^2}{12}\Delta_{ij} & 0 \\ 0 & 0 & \dfrac{h^2}{12}\Delta_{ij} \end{bmatrix} \left|[J]\right| \, d\xi \, d\eta \tag{A.33}$$

where

$$\Delta_{ij} = N_{ox}N_{i,x}N_{j,x} + N_{oxy}\left(N_{i,x}N_{j,y} + N_{i,y}N_{j,x}\right) + N_{oy}N_{i,y}N_{j,y} \tag{A.34}$$

The preceding equations show that under a pure axial compression load, the initial-stress matrix is positive definite. However, a pure shear condition generally yields a geometric matrix which is neither positive definite nor negative definite.

Due to the favorable results reported in the literature on nine-node Lagrangian type elements [90, 49], this type of element will be used exclusively in this work. It has been widely reported that trouble arises from the application of Reissner-Mindlin theory to thin plate situations as the ratio of plate thickness to span gets sufficiently small. Intuitively and also from a physical standpoint, as the ratio becomes sufficiently small, the contribution of shear deformation to the total strain energy should become negligible compared to the contribution of bending deformation. It can be observed that the bending strain is represented by a linear term, while the transverse shear strain varies parabolically. To alleviate this problem, various remedies have been proposed in the last two decades [90]. The selective integration approach was taken here such that the element bending and transverse shear terms in Equation (A.29) were integrated numerically using 3×3 Gauss quadratures (full integration) for the term

$$\int_{-1}^{1}\int_{-1}^{1} [B_{bi}]^T [C_b][B_{bj}]\,|[J]|\, d\xi\, d\eta \tag{A.35}$$

while a 2×2 scheme (reduced integration) was used for the term

$$\int_{-1}^{1}\int_{-1}^{1} [B_{si}]^T [C_s][B_{sj}]\,|[J]|\, d\xi\, d\eta \tag{A.36}$$

The full integration scheme is also applied to calculation of the geometric matrix. Note that it is necessary for the plane stress components to be available at the nine integration points in each element to form the geometric matrix. These components can be computed by a plane stress analysis.

B SURFACE-AREA BASED PARAMETRIZATION AND FINITE-DIFFERENCE APPROXIMATION

B.1 Surface-Area Based Parametrization

More details about this method can be found in the work by Theodoracatos and Bobba [69]. Here, we present the formulae for reference. The normalized u-direction surface-area based parametrization can be represented by

$$
\begin{aligned}
u_1 &= 0 \\
u_i &= \frac{1}{A}\sum_{j=2}^{N_v}\left|\vec{A}_{ij1} - \vec{A}_{ij2}\right| \\
&(2 \le i \le N_u)
\end{aligned}
\tag{B.1}
$$

Here

$$
\begin{aligned}
\vec{A}_{ij1} &= \frac{1}{2}\left(\vec{r}_{i,j} - \vec{r}_{i,j-1}\right)\times\left(\vec{r}_{i,j} - \vec{r}_{i-1,j}\right) \\
\vec{A}_{ij2} &= \frac{1}{2}\left(\vec{r}_{i-1,j-1} - \vec{r}_{i,j-1}\right)\times\left(\vec{r}_{i-1,j-1} - \vec{r}_{i-1,j}\right) \\
\vec{r}_{i,j} &= \left(P_x(u_i, v_j),\ P_y(u_i, v_j),\ P_z(u_i, v_j)\right)^T
\end{aligned}
\tag{B.2}
$$

represent the areas of two triangles resulting from the diagonal division of a quadrilateral patch and points on the surface in vector form. The area A is defined by

$$
A = \sum_{i=2}^{N_u}\sum_{j=2}^{N_v}\left|\vec{A}_{ij1} - \vec{A}_{ij2}\right| \tag{B.3}
$$

which can be interpreted as an approximation to the surface area. Note that the parameters u_i in Equation (B.1) could alternatively be defined as

$$u_i = \frac{1}{A}\sum_{j=2}^{N_v}\left(\left|\bar{A}_{ij1}\right| - \left|\bar{A}_{ij2}\right|\right)$$

$$(2 \le i \le N_u) \tag{B.4}$$

However, it is felt that the former is preferred because it yields a smaller increment when a noncoplanar patch is encountered. Consequently, Equation (B.1) is used exclusively in this study.

Similarly, the normalized v-direction surface-area based parametrization can be represented by

$$\begin{aligned} v_1 &= 0 \\ v_i &= \frac{1}{B}\sum_{j=2}^{N_u}\left|\bar{B}_{ij1} - \bar{B}_{ij2}\right| \\ &(2 \le i \le N_v) \end{aligned} \tag{B.5}$$

with

$$\begin{aligned} \bar{B}_{ij1} &= \frac{1}{2}\left(\bar{r}_{i-1,j-1} - \bar{r}_{i-1,j}\right)\times\left(\bar{r}_{i,j} - \bar{r}_{i-1,j}\right) \\ \bar{B}_{ij2} &= \frac{1}{2}\left(\bar{r}_{i-1,j-1} - \bar{r}_{i,j-1}\right)\times\left(\bar{r}_{i,j} - \bar{r}_{i,j-1}\right) \\ B &= \sum_{j=2}^{N_v}\sum_{i=2}^{N_u}\left|\bar{B}_{ij1} - \bar{B}_{ij2}\right| \end{aligned} \tag{B.6}$$

B.2 Gaussian and Mean Curvatures and Finite-Difference Approximation

The topic of the Gaussian and mean curvatures and their usefulness in quantitatively characterizing a surface can be found in many references [e.g., 63]. Here, only the analytical expression and the finite-difference approximation to the curvature associated with a surface in parametric form are given.

Let a surface be characterized by

$$\begin{aligned} x &= P_x(u,v) \\ y &= P_y(u,v) \\ z &= P_z(u,v) \end{aligned} \tag{B.7}$$

The Gaussian and mean curvatures at an arbitrary point of the surface can then be computed by

$$\begin{aligned} K &= \frac{LN - M^2}{EG - F^2} \\ H &= \frac{1}{2}\frac{EN - 2FM + GL}{EG - F^2} \end{aligned} \tag{B.8}$$

respectively, where

$$\begin{aligned} E &= \vec{r}_{,u} \bullet \vec{r}_{,u} \\ F &= \vec{r}_{,u} \bullet \vec{r}_{,v} \\ G &= \vec{r}_{,v} \bullet \vec{r}_{,v} \end{aligned} \tag{B.9}$$

$$\begin{aligned} L &= \vec{n} \bullet \vec{r}_{,uu} \\ M &= \vec{n} \bullet \vec{r}_{,uv} \\ N &= \vec{n} \bullet \vec{r}_{,vv} \end{aligned} \tag{B.10}$$

with

$$\bar{r}_{,u} = \frac{\partial \bar{r}}{\partial u}, \quad \bar{r}_{,uu} = \frac{\partial^2 \bar{r}}{\partial u^2}, \quad \bar{r}_{,uv} = \frac{\partial^2 \bar{r}}{\partial u \partial v}; \quad \text{etc}$$

$$\bar{n} = \frac{\bar{r}_{,u} \times \bar{r}_{,v}}{\left|\bar{r}_{,u} \times \bar{r}_{,v}\right|} \tag{B.11}$$

To illustrate the finite-difference approximation, we illustrate the procedure for a scalar function $P(u,v)$. The associated finite-difference stencils for the first-order derivatives are shown in Figure B.1. The first-order partial derivative $\frac{\partial P}{\partial u}$ at the grid point (u_i, v_j) can be approximated by

$$\frac{1}{\Delta_{i+1}^u {\Delta_i^u}^2 + \Delta_i^u {\Delta_{i+1}^u}^2}\left[{\Delta_i^u}^2\left(P_{i+1,j} - P_{i,j}\right) - {\Delta_{i+1}^u}^2\left(P_{i-1,j} - P_{i,j}\right)\right] \tag{B.12}$$

if the grid point is not at the u-direction boundary, where $\Delta_i^u = u_i - u_{i-1}$. Note that the set of u_i may be enriched for display purpose by adding a number of interior values in each interval formed by the u-direction parameters. It will be assumed that the number of the enriched u-direction values is m. This is also applicable to the v-direction derivatives. For the grid points at the left u-direction boundary, i.e., (u_1, v_j), the following approximation can be used

$$\frac{1}{\Delta_3^u {\Delta_2^u}^2 + \Delta_2^u {\Delta_3^u}^2}\left[\left({\Delta_2^u}^2 + {\Delta_3^u}^2\right)\left(P_{2,j} - P_{1,j}\right) - {\Delta_2^u}^2\left(P_{3,j} - P_{1,j}\right)\right] \tag{B.13}$$

while at the right u-direction boundary (u_m, v_j), the derivatives with respect to u can be approximated by

$$\frac{1}{\Delta_m^u {\Delta_{m-1}^u}^2 + \Delta_{m-1}^u {\Delta_m^u}^2}\left[{\Delta_m^u}^2 \left(P_{m-2,j} - P_{m,j}\right) - \left({\Delta_m^u}^2 + {\Delta_{m-1}^u}^2 \right)\left(P_{m-1,j} - P_{m,j}\right)\right] \quad \text{(B.14)}$$

Similar expressions can be derived to calculate other derivatives. It should be pointed out that the preceding finite-difference approximations are of second-order accuracy.

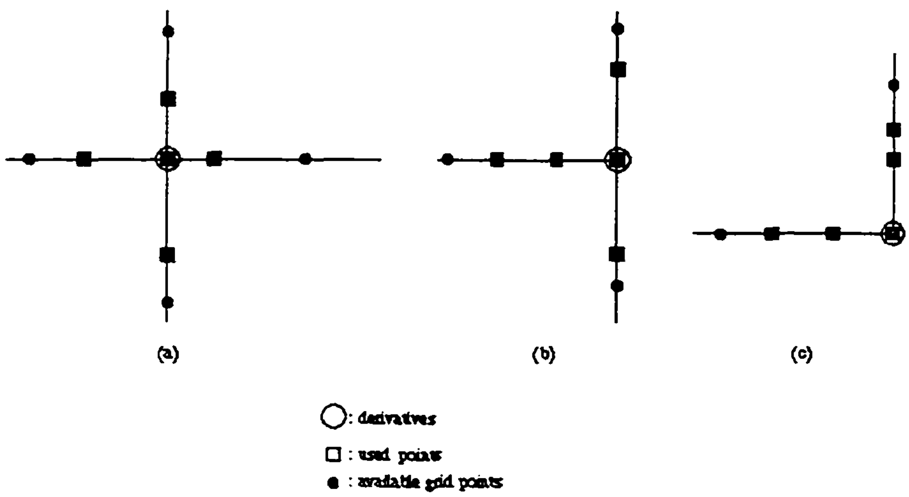

Figure B.1 Finite-difference stencils: (a) interior points; (b) boundary points; (c) corner point.

IMAGE EVALUATION TEST TARGET (QA-3)

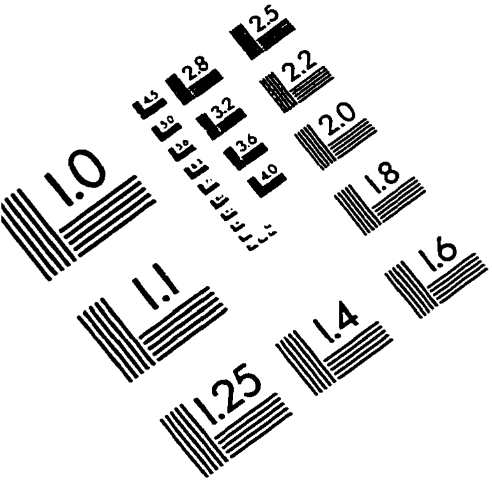

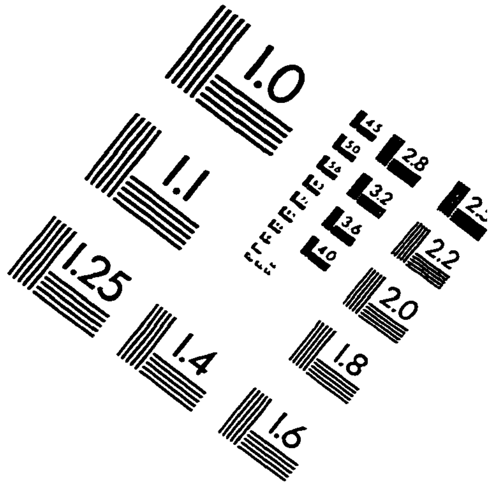

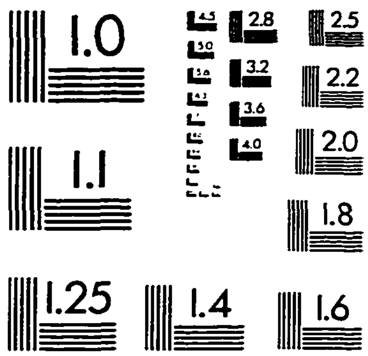

150mm

6″

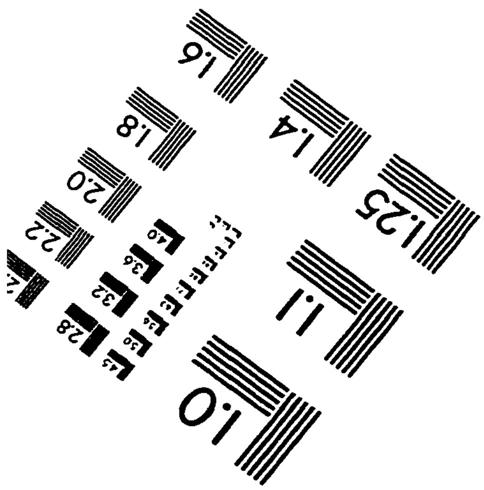

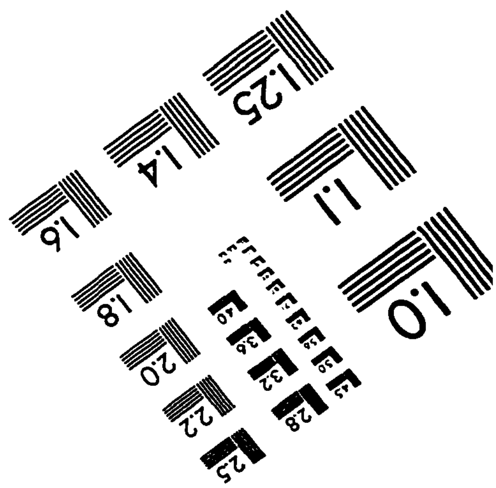

APPLIED IMAGE, Inc
1653 East Main Street
Rochester, NY 14609 USA
Phone: 716/482-0300
Fax: 716/288-5989